university of groningen / faculty of science and engineering / kapteyn astronomical institute

ASTRONOMY MASTER'S THESIS

A semi-analytic model for the evolution of star forming disc galaxies

Author:
Anna. F. Esselink

Supervisors:
Prof. dr. Filippo Fraternali
dr. Francesca Rizzo

August 2025

Abstract

Most star-forming galaxies in the Universe host a rotationally supported disc, which is the main site of gas accretion and star formation. The evolution of these discs is not well understood, as it depends on several connected processes and varies strongly with galaxy mass and redshift. Simple spatially resolved models are useful to interpret observed scaling relations and to compare with the growing amount of resolved data across cosmic time.

We present a radially resolved semi-analytic model for the evolution of star-forming disc galaxies. The model self-consistently includes gas accretion, angular momentum conservation, radial flows, star formation, and an evolving dark matter halo. The free parameters of the model are constrained through MCMC fitting to local scaling relations: the baryonic Tully-Fisher relation, the relation between the specific angular momentum, baryonic mass and gas fraction, and the stellar size-mass relation.

The model successfully reproduces the local scaling relations. The resulting evolution shows inside-out growth, extended gas discs relative to stars, and star-formation histories peaking near $z \sim 2$. Comparison with high-redshift observations reveals mixed agreement. The model underpredicts the evolution of the Tully-Fisher relation in massive systems, likely due to underestimated early halo growth, while it more closely matches the evolution of the stellar and baryonic specific angular momentum - mass relations. Stellar sizes evolve only modestly in comparison to empirical evolution of the stellar size-mass relation. The star formation main sequence is reproduced qualitatively with elevated high-z SFRs. The model reproduces stellar-to-halo mass relation at $z = 0$, but shows systematically high stellar-to-halo ratios at high-z compared to the observed evolution. These tensions highlight the need for physically motivated extensions, such as feedback-driven outflows, delayed stellar recycling, and faster early halo growth. Overall, our model captures the first-order evolution of disc galaxy properties across cosmic time and provides constraints on parameters such as accretion timescales and angular-momentum growth.

Contents

1 Introduction **3**
1.1 Ingredients for disc evolution . . . 3
1.2 Kinematic scaling relations and their evolution as model benchmarks . . . 5
1.3 Existing evolution models and their limitations . . . 11
1.4 Overview of the thesis . . . 13

2 Evolution Model **14**
2.1 Dark matter halo . . . 15
2.2 Gas accretion . . . 17
2.3 Radial flows . . . 19
2.4 Star formation law . . . 20
2.5 Self-consistent rotation velocity . . . 21
2.6 Initializing the model & numerical details . . . 22
2.7 Constraining model parameters . . . 26

3 Data **28**
3.1 Observational data for higher redshifts . . . 28
3.2 Physical parameters for the high-z samples . . . 29
3.3 High-z galaxies compared to local scaling relations . . . 33

4 Results **35**
4.1 Constraints on the free parameters of the evolution model . . . 35
4.2 Behaviour of the disc properties of modelled galaxies . . . 37
4.3 Evolution of scaling relations . . . 40
4.4 Impact of different n and j mismatch on best-fit parameters . . . 45
4.5 Evolution of scaling relations for no DM evolution . . . 45

5 Discussion **48**
5.1 Impact of assumptions in the evolution model . . . 48
5.2 Evolution of surface densities . . . 50
5.3 Comparison evolution model & literature . . . 51
5.4 Comparison to model with no halo evolution . . . 54
5.5 Future Work . . . 54

6 Conclusion **56**

7 Acknowledgements **58**

A Constants **65**

B Code **65**

C MCMC - Corner Plot Results **66**
C.1 Corner plots results ($n = 0.3$) . . . 66
C.2 Corner plots for different n and angular momentum mismatch . . . 69

1 Introduction

Galaxies are complex systems whose formation and evolution are governed by a combination of cosmological, dynamical and baryonic processes. Among them, star-forming galaxies (SFGs) play an important role in our understanding of galaxy evolution, as they show active star formation and structure growth across cosmic time (Kennicutt, 1998; Madau & Dickinson, 2014). A significant fraction of SFGs are disc galaxies, which are rotationally supported systems with ordered stellar motions and flattened, extended structures. Their stellar and gas components are organized into discs whose size, mass, and angular momentum reflect both the properties of the host dark matter halo and the history of gas accretion, star formation and feedback processes (Fall & Efstathiou, 1980; Mo et al., 1998; Posti et al., 2019).

The observable imprint of the different physical processes that regulate the evolution are reflected in the scaling relations of disc galaxies. Relations such as the stellar and baryonic Tully-Fisher relations (Tully & Fisher, 1977; Lelli et al., 2016b), the Fall relation between specific angular momentum and mass (Fall, 1983; Posti et al., 2018), the size-mass and star formation main sequence relations (van der Wel et al., 2014) provide crucial constraints for models of disc evolution. These scaling relations encode information about the efficiency of star formation, angular momentum retention, and the baryonic-to-dark-matter connection, offering an empirical framework to constrain galaxy formation models across cosmic time.

In this thesis, we build a radially resolved semi-analytic model for star-forming disc galaxies. The model is constrained using local scaling relations and tested against high-redshift observations to study the evolution of disc properties and scaling relations. With this method we aim to improve our understanding of the processes that govern the evolution of disc galaxies across cosmic time.

1.1 Ingredients for disc evolution

The evolution of galactic discs is driven by a set of physical processes that regulate how baryons are accreted, redistributed, converted into stars, expelled, and recycled. This section examines the influence of the dark matter (DM) halo, the mechanisms governing gas accretion, star formation, and feedback, the acquisition and redistribution of angular momentum, and the impact of mergers.

Galaxies form and evolve within dark matter haloes, which provide the dominant gravitational potential in which baryons reside. The halo mass and its growth therefore are an important factor in determining the scale and dynamics of galaxies. In ΛCDM cosmology, DM haloes assemble hierarchically from small to large scales (van den Bosch et al., 2014). The rotation of the baryonic galactic discs that are formed within the DM potential, is largely governed by the halo mass, producing rotation curves that remain flat beyond the optical disk.

1.1.1 Gas accretion

For low-mass haloes, cold filamentary gas is thought to be able to flow directly from the cosmic web into the circumgalactic medium (CGM) and onto the disc, without being shock-heated (Dekel & Birnboim, 2006), also known as cold-mode accretion. In higher mass haloes, the surrounding gas is commonly shock heated to temperatures close to the virial temperature, requiring processes such as radiative cooling to accrete onto the disc, also known as hot-mode accretion (Tumlinson et al., 2017). The halo virial mass threshold between cold and hot-mode accretion is around $M_{\rm th} \sim 10^{11.5-12}$ $\rm M_\odot$, with little evolution with redshift (Dekel & Birnboim, 2006; Kereš et al., 2005). Generally, in the early-stage of galaxy evolution, gas is expected to accrete in cold-mode accretion, due to the lower mass of the haloes at these times. Hot mode accretion becomes more important at lower redshifts when the haloes have grown more massive. The time at which the transition from cold- to hot mode accretion takes place varies based on halo mass. For massive haloes ($\gtrsim 10^{12}$ $\rm M_\odot$), this happens around $z \sim 2-3$. In lower mass haloes ($< 10^{12}$ $\rm M_\odot$) cold-mode

accretion can remain dominant up to $z = 0$ (Dekel et al., 2009; van de Voort et al., 2011). However, the full process of gas accretion onto the disc is very complex and remains not fully understood. Many mechanisms, such as gravity, heating and cooling, and feedback, impact accretion.

1.1.2 Star formation and depletion time

Within a galaxy disc, star formation occurs by gravitational collapse and fragmentation. For this to occur cold dense gas is required, e.g. molecular clouds. Inside these clouds, radiative cooling is more efficient then in the diffuse ISM. The low temperatures lead to low pressure, which increases the likelihood of a gravitational collapse inside molecular clouds (McKee & Ostriker, 2007). As stars form, their mass is locked up with a fraction of their mass being returned to the interstellar medium (ISM) through supernovae and stellar winds. The amount of gas that is returned to the ISM is mostly dependent on the initial mass function (IMF) and the star formation rate (SFR) at the time the stellar population was born. The IMF describes the mass distribution of stars of a stellar population at its birth. The first formalism for the IMF was a single power law $\phi(M) \propto M^{-2.35}$ by Salpeter (1955). The main difference with other IMFs is the behaviour at the low-mass end: the Kroupa IMF uses a broken power law, with flatter slopes at low masses (Kroupa, 2002), the Chabrier IMF adapts a log-normal form at low masses (Chabrier, 2003).

The timescale at which star formation can take place depends on the gas reservoir. An estimate of this can be made based on the SFR and gas supply at a given time using the depletion time $\tau_{\rm dep}$ $\tau_{\rm dep} \sim M_{\rm gas}/{\rm SFR}$. For galaxies with a Milky Way (MW) like mass, $\tau_{\rm dep} \sim 2 - 4$ Gyr (Whitaker et al., 2012; Tumlinson et al., 2017). However, the timescale on which the MW has been forming stars is much longer, indicating that accretion of fresh gas is required to sustain star formation on longer timescales (Schönrich & Binney, 2009; Fraternali & Tomassetti, 2012).

Neutral atomic hydrogen (HI) dominates the outer regions of galaxy discs, forming a diffuse and extended reservoir of gas that can serve as the primary fuel for future star formation once it condenses into molecular clouds. Low-mass galaxies have a high gas fraction, where the gaseous disc (HI gas) is much more extended than the stellar disc, as most of the star formation occurs in the inner disc. Consequently, their depletion time is already similar to the Hubble time, requiring little gas accretion, as long as inward radial flows can feed the central regions of the disc (Cimatti et al., 2020).

1.1.3 Feedback

Stellar evolution processes and active galactic nuclei (AGN) are the main sources of feedback in galaxies, and can strongly affect the star formation and general baryon cycle. Massive stars can inject energy in the ISM via UV radiation, and expel large amounts of gias via stellar winds and supernova explosions, while AGN can drive powerful jets and outflows. This feedback can drive turbulence in the ISM and cause large-scale outflows that carry gas out of the disc. Outflows are thought to regulate the star formation by heating or expelling the gas.

Gas ejected by stellar or AGN feedback can form large-scale galactic fountains, in which the expelled material cools and falls back toward the disc on timescales of a few hundred Myr (Fraternali et al., 2013; Nelson et al., 2015). On larger scales, wind recycling can occur, where outflows driven by stellar or AGN feedback escape into the CGM or IGM and later reaccrete over timescales of Gyrs (Oppenheimer et al., 2010). Additionally, gas heated by feedback may remain bound to the halo and cool gradually within the CGM, later accreting onto the disc through processes such as radiative or mixing-induced cooling (Voit et al., 2017; Hafen et al., 2022). In low mass galaxies, stellar feedback can remove a significant fraction of their gas and reduce their star formation overall (Muratov et al., 2015; Christensen et al., 2016).

1.1.4 Angular momentum

The angular momentum of matter is another critical factor of a galaxy disc's structure. In the early Universe, DM haloes acquire angular momentum through tidal torques from neighbouring den-

sity fluctuations (Peebles, 1969). This angular momentum is shared with the gas within the halo and is partially transferred to the disc when the gas cools and accretes onto the disc. The specific angular momentum of the accreting gas influences the size and rotation of the disc. Tidal-torque theory predicts that material accreted at later times generally carries higher specific angular momentum because torques accumulate as structure grows. Gas that remains hot in the halo cools slowly and thus experiences additional torquing and mixing before it settles into the disc. In general high angular momentum gas tends to settle at large radii. Early cold, rapid inflows deliver lower-angular momentum material more directly, letting gas settle in more central regions, with the possibility of triggering starbursts or contributing to bulge growth. The net effect is an increase of the accreted angular momentum with time, which naturally drives inside-out growth and the emergence of extended, rotationally supported discs (Stewart et al., 2013; Danovich et al., 2015). The angular momentum distribution of infalling gas can therefore regulate not only the disc size but also its rotation curve and stability, with important consequences for the star formation efficiency and morphological evolution of the galaxy (Fox & Davé, 2017).

1.1.5 Mergers

Merger events can fundamentally alter galaxies, but the significance of their impact depends strongly on the mass ratio and gas content of the progenitors, and the redshift of the event. In major mergers (mass ratios $\lesssim$3:1), the colliding systems can lose angular momentum, triggering starbursts and transform the morphology from a disc into a spheroid-dominated system. They also tend to disrupt ordered rotation, increase stellar velocity dispersion, and build up prominent spheroidal components (Lin et al., 2008). In the case where the progenitors are gas-rich (wet merger), the angular momentum loss in the gas can be less significant and subsequently re-form a rotating disc after the merger. In the local Universe, most SFGs galaxies are dominated by rotationally supported stellar components, with only modest contributions from central bulges. Their stars move predominantly in ordered circular orbits rather than in random motions, reflecting the kinematics of a dynamically cold disc. Such structural and dynamical properties suggest that the majority of present-day discs have not experienced recent major mergers (Somerville & Davé, 2015).

Minor mergers (typical mass ratios $\sim$10:1 or larger) cause less disturbance to the disc but are able to dynamically heat the stellar component or contribute to the formation of thick discs (Martin et al., 2018). Observational and theoretical estimates of both the cold gas content in present-day satellite galaxies and their merger timescales indicate that these systems do not supply enough gas to sustain the current star formation rates of large spiral galaxies (Di Teodoro & Fraternali, 2014). Consequently, minor mergers are unlikely to represent the dominant mode of gas accretion for the spiral galaxy population as a whole, particularly at low redshift (Fraternali & Tomassetti, 2012).

1.2 Kinematic scaling relations and their evolution as model benchmarks

Local star forming galaxies show strong correlations between several physical properties. These scaling relations can give useful insights into the formation of galaxies and can be used to test galaxy formation and evolution models. The kinematic scaling relations discussed in this section are well established in the local universe; however, their evolution is highly debated. A selection of local scaling relations will be used to constrain the parameter of our evolution model while others are used to check the outcome of the model and its accuracy at higher redshifts.

1.2.1 Tully-Fisher Relation

The Tully-Fisher relation (TFR) was originally presented as a linear correlation between the logarithm of the velocity widths of HI profiles and the absolute magnitudes of SFGs, with the purpose of using it as a distance indicator (Tully & Fisher, 1977). However these parameters can be

connected to other aspects of a galaxy. The velocity width is directly related to the rotation velocity of the disc. Additionally, the absolute magnitude can be expressed in terms of luminosity, which in turn can be related to the stellar mass. One common method is to assume a constant stellar mass-to-light ratio $\Upsilon_\star$ in the near-infrared 3.6 μm band, with the ratio commonly set to $\Upsilon_\star^{[3.6]} \approx 0.5\ \mathrm{M}_\odot/\mathrm{L}_\odot$.

Subsequently, the TFR is often presented as the relation between the stellar mass $M_\star$ and the rotation velocity. The flat part of the rotation curve is often used as a proxy for the rotation and reduces the intrinsic scatter in the relation (Verheijen, 2001). The circular velocity is also a tracer of the galaxy's gravitational potential and can therefore be linked to the combined mass distribution of the disc and dark matter halo.

Spatially resolved HI observations from radio interferometers can be used to establish the kinematics of galaxies from their rotation curves. HI is also an ideal tracer of $V_{\rm flat}$, because the atomic gas component is more extended than other gas components or the stellar component. At outer radii, the rotation curve is expected to be dominated by the DM halo, making $V_{\rm flat}$ closely related to the virial velocity. The linear relation between the stellar mass of the disc $M_\star$ and $V_{\rm flat}$is written as:

$$\log\left(\frac{M_\star}{M_\odot}\right) = s\log\left(\frac{V_{\rm flat}}{\mathrm{km\,s^{-1}}}\right) + \log(A), \tag{1}$$

where s is the slope and $\log(A)$ is the normalization. Their values range from $s \sim 4.5 - 5.1$, and $\log(A) \sim -0.9 - -0.2$, with an intrinsic scatter of $\sigma \approx 0.15 - 0.21$ dex (McGaugh & Schombert, 2015). Figure 1a shows the TFR with data from Lelli et al. (2016a), and Di Teodoro et al. (2021) for the massive spirals, colour coded with the gas fraction $f_{\rm gas} = M_{\rm gas}/M_{\rm bar}$. It can be observed that the baryonic mass of dwarf galaxies is dominated by gas, while massive galaxies are gas poor.

1.2.2 Baryonic Tully-Fisher Relation

The Baryonic Tully-Fisher Relation (BTFR) uses the total baryonic mass $M_{\rm bar}$, instead of the stellar mass, like the standard TFR. To obtain the baryonic mass, an estimate of the gas mass is required. In local SFGs, the gas component is dominated by atomic gas (Catinella et al., 2018). Therefore, its mass can be estimated using HI observations ($M_{\rm bar} = M_\star + M_{\rm HI}$).

The BTFR can be similarly written as the TFR (eq. (1)):

$$\log\left(\frac{M_\star}{M_\odot}\right) = s\log\left(\frac{V_{\rm flat}}{\mathrm{km\,s^{-1}}}\right) + \log(A). \tag{2}$$

Generally, more massive galaxies are dominated by their stellar component in mass, which implies that their position changes minimally compared to the TFR. Dwarf galaxies, however, are gas dominated, with their baryonic mass up to 10 times greater than their stellar mass (Cimatti et al., 2020). As a consequence, the BTFR is less steep than the TFR, with $s \sim 3.7 - 4.2$, and $\log(A) \sim 1.3 - 2.3$, for $\Upsilon_\star \approx 0.5\ \mathrm{M}_\odot/\mathrm{L}_\odot$. A change in $\Upsilon_\star$ affects both the slope and normalisation. The BTFR is a tighter and more fundamental relation than the TFR with an intrinsic scatter of only ~ 0.1 dex (Lelli et al., 2016b). Similarly to the TFR, the BTFR is plotted in fig. 1b.

1.2.3 Specific angular momentum vs. mass relation

A tight relation between the specific angular momentum and the mass of the stellar disc of SFGs was first discovered by Fall (1983), and is therefore commonly referred to as the Fall relation. The specific angular momentum j, is the angular momentum per unit mass. It is determined by the distribution of mass within the disc and its rotation velocity, which is defined, within a radius R, as

$$j(t, <R) \equiv \frac{2\pi \int_0^R \Sigma(t,R') v_{\rm rot}(t,R') R'^2 dR'}{2\pi \int_0^R \Sigma(t,R') R' dR'}, \tag{3}$$

where $\Sigma(R)$ is the surface density and $v_{\rm rot}$ the rotation velocity. The denominator defines the total mass of the component that is being considered. Since the discovery of the Fall relation, a tight

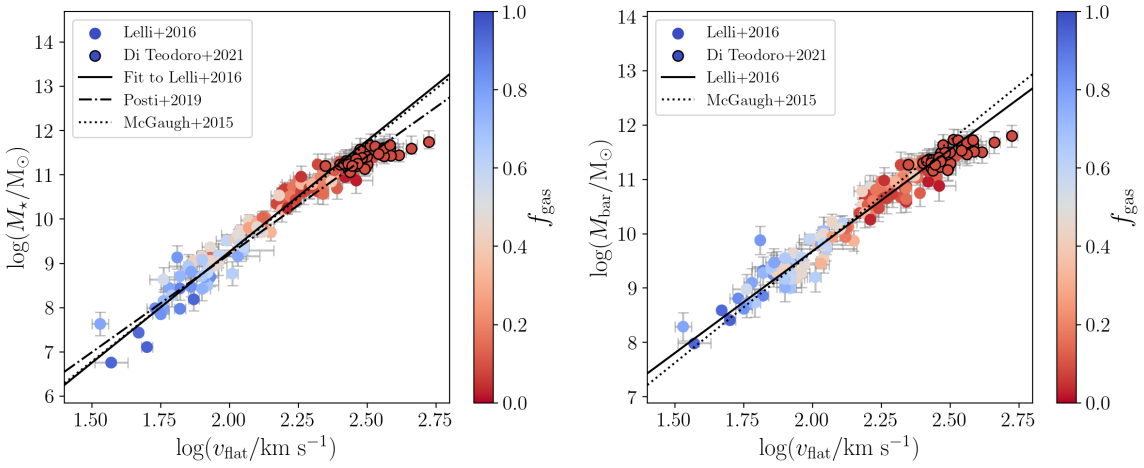

(a) Stellar Tully-Fisher Relation

(b) Baryonic Tully-Fisher Relation

Figure 1: The TFR and BTFR plotted with data from Lelli et al. (2016a) and Di Teodoro et al. (2021). The galaxy data points are coloured according to their gas fraction f_{gas}. The black lines indicate different (B)TFR relations from Lelli et al. (2016b), Posti et al. (2019) and McGaugh & Schombert (2015).

relation has been found not only for the stellar component but also for the gas and baryonic mass components of SFGs. The relation is given by:

$$\log\left(\frac{j}{10^3\ \mathrm{kpc\,km\,s^{-1}}}\right) = D + \zeta \log\left(\frac{M}{10^{11}\ \mathrm{M}_\odot}\right) \tag{4}$$

where D is the normalisation, and ζ the slope of this linear relation. For the relation between the stellar specific angular momentum $j_\star$ and $M_\star$ of spiral galaxies, $D = 3.34 \pm 0.03$ and $\zeta = 0.55 \pm 0.02$, with an orthogonal intrinsic scatter of $\sigma_\perp = 0.17 \pm 0.01$ (Posti et al., 2018). The $j - M$ relation for the stellar, gas, and baryonic component separately, has been established by Mancera Piña et al. (2021a). In this case, the gas is assumed to primarily consist of neutral atomic hydrogen (HI). Geesink et al. (2025) found that a similar also relation is present for the molecular gas H_2 at $z = 0$. These relations and their intrinsic scatter are shown in fig. 2. The characterisation of the $j_{H_2} - M_{H_2}$ shows that is more shallow than the relation of the atomic gas, and it more closely resembles the stellar $j_\star - M_\star$ relation.

The observed relation between specific angular momentum and baryonic mass can be directly connected to the properties of dark matter haloes. Cosmological N-body simulations show that haloes follow a similar scaling, with $j_h \propto M_h^{2/3}$ (Bullock et al., 2001a). This parallel suggests that galaxies inherit much of their angular momentum from their host haloes, establishing a link between baryonic discs and the dark matter structures in which they form and evolve. In the formation of a galactic disk, the baryons and DM are in the same gravitational potential, consequently they will have a similar initial specific angular momentum j.

$$j_b = \frac{J_{\mathrm{bar}}}{M_{\mathrm{bar}}} \approx j_{\mathrm{DM}} = \frac{J_{\mathrm{DM}}}{M_{\mathrm{vir}}}, \tag{5}$$

where J_{bar} and J_{DM} are the total angular momentum of the baryons and DM respectively, and it can generally be assumed that the DM composes most of the virial mass ($M_{\mathrm{DM}} \approx M_{\mathrm{vir}}$). As matter is accreted through mergers and smooth inflows, the conservation of angular momentum implies that eq. (5) should broadly hold. In practice, baryons can lose part of their angular momentum to the dark matter halo or to outflows during cooling and feedback processes, such that discs typically retain a fraction of the halo's specific angular momentum (Fall & Efstathiou, 1980; Mo et al., 1998).

1.2.4 j - M - $f_{\rm gas}$ relation

Mancera Piña et al. (2021b) expanded on the j - M relations, with the discovery of tight correlations in the $j - M - f_{\rm gas}$ space for the stellar, gas and baryonic component of disc galaxies. The relation between the parameters is given by

$$\log\left(\frac{j_i}{\rm kpc\,km\,s^{-1}}\right) = \alpha_i \log\left(\frac{M_i}{M_\odot}\right) + \beta_i \log(f_{\rm gas}) + \gamma_i \tag{6}$$

The best fit coefficients found by Mancera Piña et al. (2021b) are listed in table 1. The lowest uncertainty and scatter are found for the baryonic component. The data of the galaxies in the $j - M - f_{\rm gas}$ plane for the three different mass components is shown in fig. 2. In general, it can be observed that at fixed mass, for the stellar and baryonic component, $f_{\rm gas}$ increases with increasing j. For the gas component, the reverse is seen, as $f_{\rm gas}$ decreases with increasing j.

	α	β	γ	$\sigma_\perp$
Stars	0.67 ± 0.03	0.51 ± 0.08	-3.62 ± 0.23	0.10 ± 0.01
Gas	0.78 ± 0.03	-0.49 ± 0.04	-4.64 ± 0.25	0.08 ± 0.01
Baryons	0.73 ± 0.02	0.46 ± 0.05	-4.25 ± 0.19	0.08 ± 0.01

Table 1: Best fit coefficients for the $j - M - f_{\rm gas}$ plane (eq. (6)) (Mancera Piña et al., 2021b)

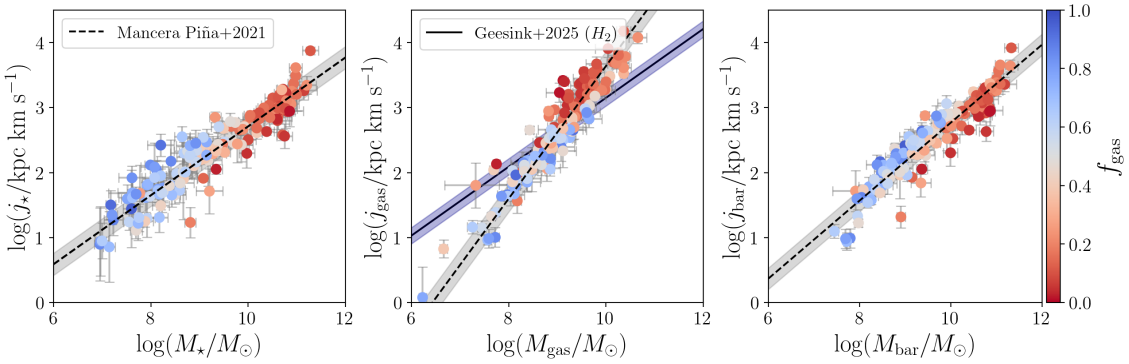

Figure 2: The $j - M$ relation (from left to right) for the stellar, gas, and baryonic component of the galaxies. Adapted from Mancera Piña et al. (2021b). The data points are coloured according to their gas fraction $f_{\rm gas}$. The dashed line is the best fit $j - M$ relation from Mancera Piña et al. (2021a), with the intrinsic scatter in grey. The $j_{H_2} - M_{H_2}$ relation is similarly shown in blue (Geesink et al., 2025).

1.2.5 Size-Mass relation

The disc size of SFGs is directly related to its mass, as described by the size-mass relation:

$$\log\left(\frac{R_{\rm eff}}{1\,\rm kpc}\right) = \log(A) + \alpha \log\left(\frac{M_\star}{5 \times 10^{10} M_\odot}\right), \tag{7}$$

where $R_{\rm eff}$ is the effective radius. However, this relation has a relatively high scatter. At $z = 0$, the slope is found to be $\alpha \approx 0.22$ (van der Wel et al., 2014). Different parametrizations of the size-mass relation and their scatter are presented in fig. 3. The relations of Shen et al. (2003) and van der Wel et al. (2014) are based on samples containing SFGs with observation form SDSS and HST respectively, while the relation from Posti et al. (2019) is based on a smaller sample of only disc galaxies with regular kinematics.

The evolution of this relation can reveal a lot about the growth of galaxies and the related physical parameters. Using observations with JWST, the relation between the effective radius and redshift at fixed mass has been explored up to $z = 10$. For a fixed stellar mass of $5 \times 10^{10}\ M_{\odot}$, the evolution of the effective radius for SFGs is $R_{\rm eff} \propto (1+z)^{-1.21\pm0.05}$ (Yang et al., 2025). The growth of the effective radius over time in an indication of the inside-out growth of galactic discs.

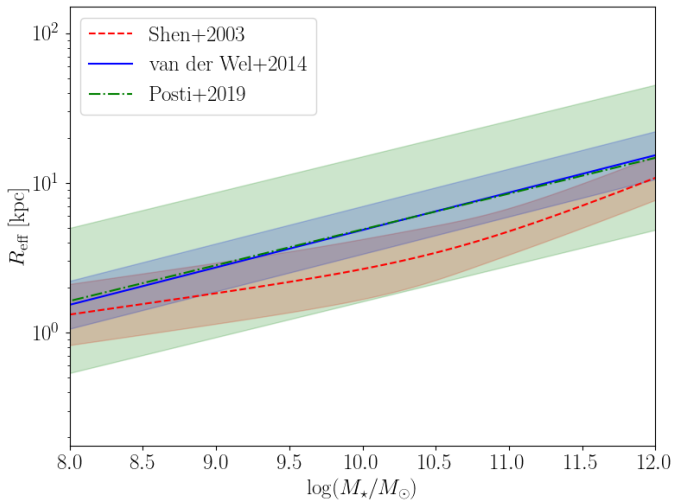

Figure 3: The stellar size-mass relations from Shen et al. (2003) (red), van der Wel et al. (2014) (blue) and Posti et al. (2019) (green). The band around the relation represents the intrinsic scatter.

1.2.6 Star formation main sequence

For SFGs a correlation is found between their global SFR and stellar mass $M_\star$, known as the star formation main sequence (SFMS). The relation is commonly described by a power law:

$$\log(\mathrm{SFR}) = \alpha(\log M_\star - 10.5) + \beta \tag{8}$$

with a slope of $\alpha \approx 0.7$, and normalization of $\beta \approx 0.38$ at $z = 0$ (Whitaker et al., 2012). Starburst galaxies have a higher SFR and lie around $\gtrsim 0.5$ dex above the SFMS at equal $M_\star$, while quenched galaxies lie below the relation. However, the majority of SFGs are found on the SFMS, indicating that their stellar mass is build up in a steady mode rather than in short-lived bursts.

The evolution of the SFMS can be describe by the empirical relation from Popesso et al. (2023):

$$\log \mathrm{SFR}(t, \log M_\star) = (-0.034t + 4.722)\log M_\star - 0.1925 \log^2 M_\star + (-26.16 + 0.2t) \tag{9}$$

where t is the cosmic time and $M_\star$ the stellar mass. Figure 4 shows the relation at different redshifts. This parametrization flattens the slope of the SFMS at high masses. The evolution indicates that a given stellar mass, the SFR is larger at higher redshifts.

1.2.7 Stellar-to-halo mass relation

An important parameter in the evolution of galaxies is the stellar-to-halo mass ratio:

$$f_{\mathrm{m},\star} \equiv \frac{M_\star}{M_{\rm vir}} < f_{\rm b}, \tag{10}$$

where $f_{\rm b}$ is the cosmic baryon fraction, the fraction of baryonic mass in relation to the mass of all matter (including DM). This condition always applies and commonly $f_{\mathrm{m},\star} \ll f_{\rm b}$. This is tied to the missing baryon problem, which is the general observation of the lack of baryonic mass in cosmic structures (McGaugh et al., 2010).

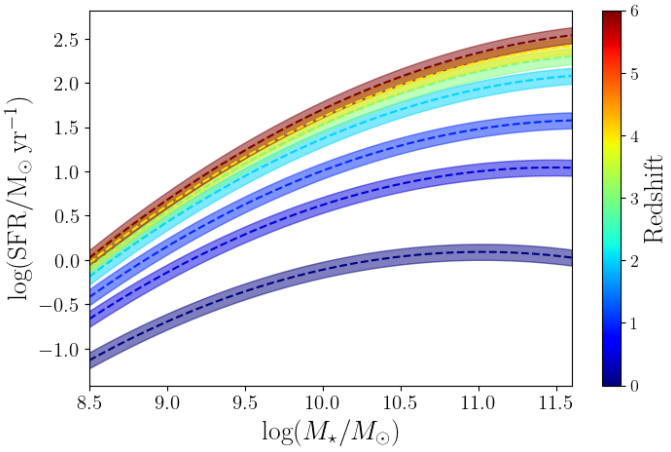

Figure 4: The star formation main sequence from Popesso et al. (2023), at different redshifts as indicated by colour. The band around the relations indicates the scatter around the best fit.

The stellar-to-halo mass ratio is expected to change with virial mass and redshift. This becomes more evident when looking at the stellar-to-halo mass relation (SHMR) of galaxies, which describes $f_{\mathrm{m},\star}$ as a function of M_{vir}. The SHMR can be established using the stellar mass function (SMF), and the halo mass function (HMF) from cosmological N-body simulations, using the method of halo abundance matching (Behroozi et al., 2013). The matching in this method assumes that more massive haloes host more massive galaxies, allowing for one-to-one mapping. With this procedure a stellar mass $M_\star$ can be connected to a specific halo mass M_{vir} by taking the value for which the number density of the HMF at M_{vir} is equal to that of the SMF at $M_\star$ (Cimatti et al., 2020).

The relation itself can be modelled by a double power-law (Moster et al., 2013):

$$\frac{M_\star}{M_{\mathrm{halo}}} = \epsilon \left[\left(\frac{M_{\mathrm{halo}}}{M_1} \right)^{-\alpha} + \left(\frac{M_{\mathrm{halo}}}{M_1} \right)^{\beta} \right]^{-1}, \tag{11}$$

where ϵ is called peak efficiency ($\epsilon \approx 0.035$), M_1 is the characteristic halo mass ($M_1 \approx 10^{12}$ M$_\odot$), and $\alpha \approx -0.5$ and $\beta \approx 3.0$ are the slopes at low and high masses respectively. The nonlinearity of the SHMR can be connected to the star formation efficiency since it has a direct correlation with $f_{\mathrm{m},\star}$. At low halo masses, the star formation is less efficient due to relatively strong impact of supernova feedback (Christensen et al., 2016). At high halo masses, the star formation efficiency is limited by AGN feedback and virial shock heating (Dekel & Birnboim, 2006). Therefore, the highest star formation and $f_{\mathrm{m},\star}$ are found at intermediate masses ($M_{\mathrm{halo}} \sim 10^{12} M_\odot$, Milky Way like), as can be observed in fig. 5, left.

Figure 5 shows that from $z = 4$, the SHMR appears to evolve relatively little, especially for $M_{\mathrm{halo}} < 10^{12}\ M_\odot$. For massive galaxies, star formation is commonly quenched, and hence their main source of growth is mergers. The most significant change is seen to take place at $z > 4$ (Behroozi et al., 2013; Behroozi et al., 2019). At higher redshifts, the peak in the stellar-to-halo mass ratio appears at lower masses, implying more efficient star formation at lower halo masses at early times.

1.2.8 Concentration-mass relation

The concentration of DM haloes scales with virial mass and redshift. This concentration-mass relation for redshifts $0 < z < 5$ has been established by Dutton & Macciò (2014), using cosmological N-body simulations.

$$\log(c_{\mathrm{vir}}) = a + b \log \left(\frac{M_{\mathrm{vir}}}{10^{12} h^{-1} \mathrm{M}_\odot} \right), \tag{12}$$

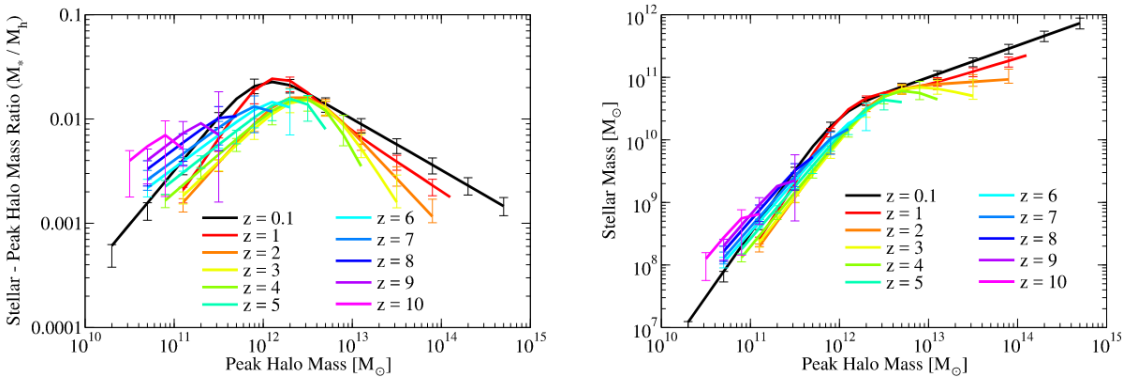

Figure 5: *left:* The stellar-to-halo mass ratio ($f_{\mathrm{m},\star}$) as a function of peak halo mass M_{peak} for redshifts 0.1-10. *right:* The stellar-to-halo mass relation for redshifts 0.1-10. Figures taken from Behroozi et al. (2019)

Where h is the reduced Hubble constant. The evolution of the zero-point a and slope b are given by (for Planck cosmology (Planck Collaboration et al., 2020))

$$a = 0.537 + (1.025 - 0.537)\exp\left(-0.718z^{1.08}\right) \tag{13}$$

$$b = -0.091 + 0.024z \tag{14}$$

From eqs. (12) to (14) we see that, in general, the concentration decreases with increasing halo mass. The slope of the relation flattens with redshift. At redshifts $z \sim 4 - 5$, the concentration is nearly constant, at $\log(c_{\mathrm{vir}}) \approx 0.5$, for changing mass.

1.3 Existing evolution models and their limitations

To study the formation of galaxies, popular methods are hydrodynamical simulations and semi-analytic models (SAM), which each come with their own advantages and disadvantages. With SAMs, a special category is represented by radially resolved disc models. which offer a middle ground between the high computational cost and complexity of hydrodynamical simulations and the oversimplifications in unresolved galaxies, typical of the more standard SAMs. Resolved disc models can track spatially dependent processes like inside-out growth, radial flows and angular momentum transport. This approach is critical for understanding the observed gradients in metallicity, stellar populations, and gas content and it allows for direct comparison with spatially resolved observations without the numerical noise, resolution limits and subgrid uncertainties that come with hydrodynamical simulations. Here we highlight several radially resolved disc models.

Among the most sophisticated implementations of radially resolved semi-analytic approaches are the chemical evolution models of the Milky Way, which provide a detailed framework to study the build-up of stellar populations and abundance gradients in our Galaxy. These models couple prescriptions for gas accretion, star formation, and radial flows with the enrichment from stellar evolution and supernovae, enabling them to reproduce the observed chemical abundance patterns across the galactic disc. The classical two-infall model of Chiappini et al. (2001) was among the first to explain the bimodality in the $[\alpha/\mathrm{Fe}] - [\mathrm{Fe/H}]$ plane through distinct episodes of gas accretion, successfully accounting for the properties of both the thick and thin discs. Later, Schönrich & Binney (2009) extended this framework by including radial migration of stars, showing that the mixing of stellar populations is essential to reproduce the observed abundance distributions and metallicity gradients. Building on this, Bilitewski & Schönrich (2012) further refined the modelling of gas flows and stellar migration, providing an even more detailed picture of the

interplay between chemical enrichment and dynamical processes. Extending these models to a general framework for resolved galaxy evolution models comes with several challenges, including much less observational constraints and an increase in the diversity of galaxy properties and evolution paths.

Fraternali & Tomassetti (2012) presented a radially resolved inversion method based on a set of simplifying assumptions. The disc is divided into independent annuli, each following a prescribed star formation history (SFH). Using the observed Kennicutt-Schmidt relation, the star formation rate density $\Sigma_{\rm SFR}$ is linked to the gas surface density ($\Sigma_{\rm gas}$) with a power law $\Sigma_{\rm SFR} \propto \Sigma_{\rm gas}^{n}$. Assuming this relation holds in each annuli, then sustaining a given SFH requires a corresponding accretion history. Their resulting radially resolved accretion rates imply significant late-time gas accretion, migrating outward with time (inside-out growth). The model is reliant on a simple parametrisation of an assumed SFH. The angular momentum distribution or radial flows were not explicitly considered, while the galactic potential is assumed constant in time.

Pezzulli & Fraternali (2016) moved away from the so-called independent-annuli approach, by allowing gas exchange between annuli. The conservation of angular momentum following gas accretion requires mass flows between annuli (Mayor & Vigroux, 1981). Following this requirement, they provide analytic functions for the accretion profiles, radial flows and abundance gradients as a function of the angular momentum of the accreting gas. The effective accretion is decomposed into direct accretion from the intergalactic medium (IGM), and the internal contribution from radial flows (Pitts & Tayler, 1989). To constrain the contributions from either, assumptions on the shape of the surface density are required, in addition to observational constraints from abundance gradients. Additionally, a fixed galactic potential was used. From this analysis, they show that even a small mismatch between the angular momentum of the accreting gas and that of the disc leads to coherent radial flows. These flows are able to reproduce the observed negative metallicity gradient in the Milky Way disc, which cannot be explained in a framework of strictly independent annuli. The results therefore highlight the importance of angular momentum conservation and radial gas transport in shaping the chemical structure of galactic discs.

In the model by Popping et al. (2014), radially resolved discs are placed in a cosmological semi-analytic framework. The cold gas is partitioned into HI and H_2 using pressure- or metallicity-based recipes. Consequently star formation can be tied directly to the molecular component, letting the model track the radial SFR and metallicity profiles, as well as global HI/H_2 scaling relations across time. The model successfully reproduces the observed HI and H_2 mass functions and their evolution, and it captures the global scaling relations between gas fractions, stellar mass, and SFR. The model is reliant on equilibrium partitioning recipes, axisymmetric independent annuli, and parametrized feedback, outflows and re-accretion that are not dynamically coupled to the halo, i.e. they rely on independent prescription instead of arising self-consistently from interaction between the galaxy and its host halo.

In this thesis we build on the work by Costa (2024). In their work, a resolved disc evolves following a set accretion rate history with a prescribed radial accretion profile (described further in section 2.2). The accretion radius is constrained by a prescribed evolution of the specific angular momentum of the accreting gas, for which a range of different accretion timescales were explored. They further explore the impact of different star formation laws. In their work they aimed to reproduce the $j_{\rm bar} - M_{\rm bar} - f_{\rm gas}$ relation, they succeed and conclude inside-out growth is a crucial component in reproducing this relation. In their model no DM halo is considered and the rotation velocity is set to remain constant over time following the TFR, i.e. a fixed potential is assumed. They also use the independent annuli approach. In this work we aim to remove these assumption and constrain the free parameters of the model using local scaling relations.

1.4 Overview of the thesis

In this thesis we build a semi-analytic model for the evolution of star forming disc galaxies and use it to study the evolution of various scaling relations. In Chapter 2 the different components of the model are described, including the DM halo evolution, gas accretion, star formation, disc rotation and radial flows. The numerical details of the model and the method used to constrain the free parameters of the model are also discussed. The high redshift data sample that we compiled, including the computation of the gas mass and angular momentum, are presented in Chapter 3, and then compared to local scaling relations. The results of the model are shown in Chapter 4, where the outcome of the parameter fitting and the resulting prediction for the evolution of disc properties and scaling relations are presented. In Chapter 5 we discuss what impact the assumptions in our model have on our results, and how the predicted evolution of the scaling relations compares to our high redshift data sample and to their evolution presented in the literature. Lastly, we summarize our main findings and conclusions in Chapter 6.

2 Evolution Model

The evolution of disc galaxies is governed by several interconnected processes, including gas accretion, star formation, stellar feedback, and radial flows, as described in section 1.1. In simple terms, when the gas from the CGM cools, it settles at the centre of dark-matter haloes and can be accreted onto galaxies. This gas can fuel star formation in the galactic discs.

To capture the interplay between these processes and their impact on the properties and kinematics of SFGs, we have constructed a semi-analytic radially resolved evolution model. The evolution is tracked in terms of the gas and stellar surface densities and their rotation velocity over time. The model includes dark matter halo growth, gas accretion, angular momentum growth and radial flows within the disc. This model builds on the formalism of Costa (2024), using their treatment of gas accretion and inside-out growth, while introducing a time-evolving dark matter halo, modified star formation law, self-consistent rotation curves and radial flows .

In our galaxy evolution model, the DM halo evolves independently of the disc. The growth of the halo and its properties is described in section 2.1. The evolution of stars and gas in disc galaxies can be described in terms of their surface densities $\Sigma_{\rm gas}$ and $\Sigma_\star$ as (Cimatti et al., 2020):

$$\frac{\partial \Sigma_{\rm gas}}{\partial t} = \dot{\Sigma}_{\rm eff} - \dot{\Sigma}_{\rm out} + \dot{\Sigma}_{\rm ret} - \Sigma_{\rm SFR}, \tag{15}$$

$$\frac{\partial \Sigma_{\star}}{\partial t} = \dot{\Sigma}_{\star,\rm rf} - \dot{\Sigma}_{\rm ret} + \Sigma_{\rm SFR}, \tag{16}$$

where $\dot{\Sigma}_{\rm eff}$ is the effective accretion rate, $\dot{\Sigma}_{\rm out}$ is the outflow rate, $\dot{\Sigma}_{\rm ret}$ is the gas return rate from stellar evolution, $\Sigma_{\rm SFR}$ is the star formation rate (SFR), and $\dot{\Sigma}_{\star,\rm rf}$ is the rate at which the surface densities change due to radial flows. In general, the rate of change in the surface densities will be given in $\mathrm{M_\odot\,pc^{-2}\,Gyr^{-1}}$. In the model the galactic disc is split up into concentric and coplanar annuli, along which these surface densities are defined. In this model, the gas component represents the sum of the atomic HI and molecular H_2 gas.

A key ingredient is gas accretion $\dot{\Sigma}_{\rm acc}$ from the CGM, which is related to the accretion rate history. As discussed in section 2.2, to ensure an inside-out formation of the disc, the angular momentum of the accreted gas is set to increase over time. The effective accretion rate $\dot{\Sigma}_{\rm eff}$ in eq. (15) consists of two contributions, an annulus can gain gas from outside the disc ($\dot{\Sigma}_{\rm acc}$) or from adjacent annuli. The latter are radial flows, induced by the conservation of angular momentum. Stars also move through disc, however their radial flows ($\dot{\Sigma}_{\star,\rm rf}$, eq. 16) are not directly impacted by the gas accretion. The radial flows and their impact on the disc is described in section 2.3.

The outflow rate $\dot{\Sigma}_{\rm out}$ in eq. (15) describes the loss of gas to the external environment of the galaxies. The main sources of outflows are AGN and stellar feedback. For massive galaxies, the speed of the outflowing gas does not exceed the escape velocity, and hence an assumption of no outflows can be safely made when modelling a galaxy at a larger scale over long cosmic times. In our evolution model, outflows are omitted for all galaxy masses. This is a limitation that we will further discuss in section 5.1.

The return rate $\dot{\Sigma}_{\rm ret}$ is the rate at which gas is returned to the ISM by stars, through supernova explosions and mass losses, hence this term is added to the gas surface density (eq. 15), and subtracted from the stellar surface density (eq. 16). The return rate is dependent on the SFR, and the initial mass function (IMF). $\Sigma_{\rm SFR}$ is directly related to the amount of cold gas available in the disc. The final ingredient is the star formation law, which relates the gas surface density to the SFR. The computation of the SFR and the corresponding return rate are further discussed in section 2.4.

To gain insight into the kinematics of the galaxies, we require to know their rotation velocity. Section 2.5 describes how the rotation curve can be constructed from the properties of the dark matter halo and the surface densities of the stellar and gas components. Lastly, section 2.6 describes the numerical details of the model and section 2.7 describes the method with which the free parameters of the model will be constrained.

2.1 Dark matter halo

The gravitational potential of the DM halo in which a galaxy resides has a crucial impact on the kinematics of the galactic disc. Therefore to accurately model the kinematic evolution, the growth of the DM halo needs to be accounted for. In this evolution model, the DM evolves independently of the baryonic disc, where its growth rate is defined solely by the halo mass at a given redshift, adding no free parameters to the model.

2.1.1 Evolution of the dark matter halo

In ΛCDM cosmology, haloes grow through hierarchical merging, implying a bottom-up structure formation in which smaller systems form first, then later merge and grow into larger systems. If DM accretion and mass loss are ignored, the evolution of DM haloes can be described by a merger tree, which shows the merging of progenitor haloes over cosmic time to form larger haloes (van den Bosch et al., 2014).

The basis on which the majority of analytic models of halo are build, is the extended Press-Schechter formalism (EPS) (Bond et al., 1991). The original Press-Schechter formalism (Press & Schechter, 1974) is used to analytically describe the HMF by connecting the initial density perturbation in the Universe to the number of collapsed DM haloes. The EPS extends upon the original formalism by allowing one to follow the formation and evolution of a halo across cosmic time, in contrast to knowing solely their abundances at a specific time. The EPS can model the hierarchical formation of haloes by building merger trees, also accounting for subhaloes and the properties of progenitors (Mo et al., 2010).

For an approximation of the average dark matter accretion rate $\dot{M}_{h,12}$ we adopt the extended Press-Schechter formalism of Krumholz et al. (2018):

$$\dot{M}_{h,12}(z) \approx -\alpha M_{h,12},(z)^{1+\beta}\dot{\omega}(z) \tag{17}$$

where the masses are normalized to 10^{12} $M_\odot$, α and β are dimensionless parameters and ω is the self-similar time variable of the EPS formalism, of which the fitted time derivative is given by

$$\dot{\omega} \approx -0.0476[1+z+0.093(1+z)^{-1.22}]^{2.5}\ \mathrm{Gyr}^{-1}. \tag{18}$$

This parametrization includes the accelerated growth of the haloes at high redshift, and their more stable period at later cosmic times. Following ΛCDM cosmology, the fitted parameters are given by $\alpha = 0.628$, $\beta = 0.14$ (Krumholz et al., 2018). The resulting DM halo evolution and accretion rate are shown in fig. 6.

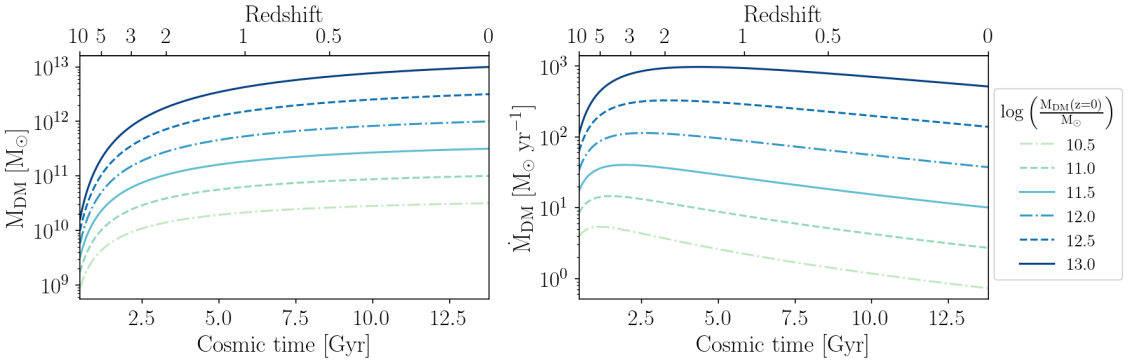

Figure 6: Evolution of the total DM halo mass *(left)*, and the DM accretion rate *(right)*, for a range of different halo masses as indicated by the colours.

In our evolution model, the dark matter halo evolves independently of the galaxy disc. Starting from the same cosmic time, haloes with different seed masses will evolve according to the

accretion rate, as a function of redshift and halo mass. To obtain the halo mass at a given cosmic time or redshift, we numerically integrate eq. (17). For a given starting time or redshift of the evolution model, we require to know the halo seed mass to obtain a specified halo mass at $z = 0$. The required halo seed mass is found by applying the bisection method, a numerical root finding algorithm, allowing us to create consistent halo evolution histories for galaxies of different masses.

2.1.2 Halo properties

Once a halo has undergone gravitational collapse and reached a dynamical equilibrium, the virial theorem can be applied to derive its properties. The virial radius is defined as the radius within which the average density is at a certain overdensity Δ_c above the critical density of the universe $\rho_{\rm crit}$ at that redshift, i.e. $\bar{\rho}(< r_{\rm vir}) = \Delta_c(z)\rho_{\rm crit}(z)$. Assuming a spherical system, where $r_{\rm vir}$ is defined as the distance from the peak of the halo density distribution, the virial mass is given by

$$M_{\rm vir} = \frac{4\pi}{3}\Delta_c(z)\rho_{\rm crit}(z)r_{\rm vir}^3, \tag{19}$$

where the critical density at a redshift z is defined by

$$\rho_{\rm crit}(z) = \frac{3H^2(z)}{8\pi G}, \tag{20}$$

where $H(z)$ is the Hubble parameter, and G is the gravitational constant. Equations (19) and (20) can then be used to derive the following expression of the virial radius (Cimatti et al., 2020).

$$r_{\rm vir} = \left[\frac{2GM_{\rm vir}}{\Delta_c(z)H^2(z)}\right]^{1/3}. \tag{21}$$

Similarly, the circular velocity at the virial radius, for a given virial mass can be inferred. For a spherical density distribution, the circular speed is simply given by

$$v_c(r) = \sqrt{r\frac{{\rm d}\Phi(r)}{{\rm d}r}} = \sqrt{\frac{GM(r)}{r}}, \tag{22}$$

where $\Phi(r)$ is the gravitational potential and $M(r)$ is the enclosed mass at radius r. The virial velocity, i.e. the circular speed at $r_{\rm vir}$, is then defined similarly using eqs. (21) and (22) as

$$v_{\rm vir} = \sqrt{\frac{GM_{\rm vir}}{r_{\rm vir}}} = [GM_{\rm vir}H(z)]^{1/3}\left[\frac{\Delta_c(z)}{2}\right]^{1/6}. \tag{23}$$

The density profile of dark matter haloes is generally well described by the Navarro-Frenk-White (NFW) profile (Navarro et al., 1996)

$$\rho(r) = \frac{4\rho_s}{(r/r_s)(1+r/r_s)^2}, \tag{24}$$

where ρ_s is the characteristic density, and r_s is the scale radius. The NWF profile transitions from a shallow slope $\rho \propto r^{-1}$ at small radii ($r \ll r_s$) to a steeper slope $\rho \propto r^{-3}$ at large radii ($r \gg r_s$). For a halo with a NFW profile the circular velocity is given by

$$v_c^2(r) = v_{\rm vir}^2\left[\frac{1}{x}\frac{\ln(1+cx) - \frac{cx}{1+cx}}{\ln(1+cx) - \frac{c}{1+c}}\right], \tag{25}$$

where $x = r/r_{\rm vir}$, and c the concentration parameter (Mo et al., 2010). The concentration parameter c, quantifies how centrally concentrated the mass distribution is, which changes as a function of halo mass and redshift (see section 1.2.8).

To compute the virial radius $r_{\rm vir}$ and velocity $v_{\rm vir}$, the evolution of the Hubble parameter $H(z)$ and the overdensity Δ_c need to be defined. For a flat ΛCDM universe, the evolution of the Hubble parameter $H(z)$ is given by (Mo et al., 2010)

$$H^2(z) = H_0^2 \left[\Omega_{r,0}(1+z)^4 + \Omega_{m,0}(1+z)^3 + \Omega_{\Lambda,0}\right], \tag{26}$$

where $\Omega_{r,0}$, $\Omega_{m,0}$ and $\Omega_{\Lambda,0}$ are the present-day density parameters for radiation, matter and vacuum energy, respectively. In this thesis, their values are taken from the Planck 2018 results (Planck Collaboration et al., 2020) (Used values of constants in the model are given appendix A). For the evolution of the overdensity Δ_c, we use the approximation give by Bryan & Norman (1998):

$$\Delta_c \approx 18\pi^2 + 82y - 39y^2, \tag{27}$$

where $y = \Omega_m(z) - 1$. The evolution of the matter density parameter $\Omega_m(z)$ is given by

$$\Omega_m(z) = \frac{\Omega_{m,0}(1+z)^3}{\Omega_{m,0}(1+z)^3 + \Omega_{r,0}(1+z)^4 + \Omega_{\Delta,0}}. \tag{28}$$

Following eq. (27), the overdensity decreases over time, from $\Delta_c \approx 178$ at $\gtrsim 5$, to $\Delta_c \approx 101$ at $z = 0$.

2.2 Gas accretion

The amount of time a galaxy can continue to form stars given their current SFR and gas supply is given by the depletion time ($\tau_{\rm dep} \sim M_{\rm gas}/{\rm SFR}$). Without accretion from the CGM, the galactic discs are expected to quench within a few Gyr. SFGs are actively forming stars to the present day. This is indirect evidence that they must have a continuous inflow of gas to replenish their gas reservoir and sustain active star formation (Fraternali & Tomassetti, 2012).

In addition to continuous accretion, mergers can also have a large impact on the evolution of galaxies. While major mergers can disrupt a disc and form an early-type galaxy (ETG) (Lin et al., 2008), the gas expelled in such events may eventually cool and be re-accreted, potentially leading to the regrowth of a spiral disc. However, the existence of a star formation main sequence, i.e. a tight correlation between stellar mass and SFR, indicates a smooth evolution process for SFGs (Speagle et al., 2014). Also, simulations show that for SFGs with stellar masses below $\sim 10^{11} M_\odot$, the majority of their stellar mass is formed in-situ (Dekel et al., 2009; Rodriguez-Gomez et al., 2016; Qu et al., 2017). Hence, SFGs are more likely to gradually build their stellar mass through the accretion of cold gas rather than through major mergers (Dekel et al., 2009). Therefore, in our model, we assume that discs grow gradually through smooth gas accretion from the CGM.

2.2.1 Gas accretion history in the model

In our model, we take an exponential form for the gas accretion history, given by (Costa, 2024)

$$\dot{M}_{\rm acc}(t) = Ce^{-\omega_{\rm acc} t}, \tag{29}$$

where C is a normalisation constant in $\mathrm{M}_\odot\ \mathrm{Gyr}^{-1}$, t is the time in Gyr, with $t = 0$ defined as the time at which the evolution model starts, $\omega_{\rm acc}$ is the accretion frequency in Gyr^{-1}, defined as the inverse of the accretion timescale ($\omega_{\rm acc} = 1/\tau_{\rm acc}$). For positive values of $\omega_{\rm acc}$, the amount of matter accreted decreases exponentially over time, for negative values of $\omega_{\rm acc}$ the opposite is true. A high value of $\omega_{\rm acc}$ would imply that most gas is accreted at early times, while a low value implies a more constant accretion rate across time. We also anticipate that a higher value would typically lead to a smaller disc, as most gas is accreted in the inner regions due to the specified inside-out growth of the disc (see section 2.2.2).

The surface brightness profiles of the stellar discs of SFGs, particularly in late-type spirals and low-mass systems, can typically be well approximated by an exponential profile (Freeman, 1970). In these galaxies, the disc dominates the light distribution, especially at intermediate and large

radii. However, in galaxies with a prominent bulge component, the profile will steeply increase in the central regions, exceeding the exponential disc. For this reason, and to simplify the problem, we assume that the gas accreted at each time is distributed exponentially in the radial direction. The surface density $\dot{\Sigma}_{\rm acc}$ is given by (Costa, 2024)

$$\dot{\Sigma}_{\rm acc}(t, R) = \frac{\dot{M}_{\rm acc}(t)}{2\pi R^2_{\rm acc}(t)} e^{-\frac{R}{R_{\rm acc}(t)}} \tag{30}$$

$$= \frac{C}{2\pi R^2_{\rm acc}} e^{-\omega_{\rm acc} t} e^{-\frac{R}{R_{\rm acc}(t)}} \tag{31}$$

where $R_{\rm acc}$ is the radial scale length of the exponential at a given time. In the evolution model, there is no initial mass ($M_{\rm bar}(t = 0) = 0$), and outflows are neglected. Therefore, the total baryonic mass that has been accreted, is given by the time integration over the accretion rate (eq. (29)).

$$M_{\rm acc}(t) = \int_0^t C e^{-\omega_{\rm acc} t'} dt' \tag{32}$$

The normalisation constant C, is then given by $C = \frac{\omega_{\rm acc} M_{\rm acc}(t_0)}{1 - e^{-\omega_{\rm acc} t_0}}$, with t_0 corresponding to the time at $z = 0$. As outflows are omitted in this evolution model, $M_{\rm acc}(t)$ is the total baryonic mass at time t, if the maximum radius is assumed to be infinite. Both $\omega_{\rm acc}$ and $M_{\rm acc}(t_0)$ are free parameters of the evolution model that will be varied and constrained.

2.2.2 Inside out growth

Galaxy discs grow inside-out, i.e. they grow in size over time (Nelson et al., 2016). Analysis of stellar populations show that the populations in the outer regions are younger than those in the inner regions, indicating that these inner regions formed earlier (González Delgado et al., 2015). Additionally, evolution of the density and star formation rate density profiles indicate that discs grow in size over time and that gas is accreted at increasingly larger radii over time (Patel et al., 2013; Pezzulli et al., 2015).

The inside-out growth of galactic discs can theoretically be related to the growth of angular momentum. An increase in the specific angular momentum implies that there is a build-up of mass at larger radii, likely coupled with an increase in the rotation velocity. Consequently, to achieve inside-out growth, it is required that the specific angular momentum of the accreting gas is greater than that of the disc at any time (Pezzulli et al., 2017). Additionally, the angular momentum of the accreted material is linked to that of dark matter haloes, which grow in size and spin over time (Bullock et al., 2001a).

To induce inside-out growth in the evolution model, we let the specific angular momentum of the accretion gas $j_{\rm acc}$ grow over time according to

$$j_{\rm acc}(t) = j_{\rm min} + (j_{\rm max} - j_{\rm min}) \left(\frac{t}{t_0} \right)^n \tag{33}$$

where n is a free parameter controlling the time evolution of $j_{\rm acc}$ (Costa, 2024). For $n = 1$, $j_{\rm acc}$ increases linearly over time from $j_{\rm min}$ at $t = 0$ to $j_{\rm max}$ at $t = t_0$. For $n < 1$, $j_{\rm acc}$ grows quickly at early times, inversely for $n > 1$, $j_{\rm acc}$ remains relatively small to then quickly increase at late times. The impact of different values for n on the galaxy evolution will be further investigated in this thesis. $j_{\rm max}$ is used as an input parameter of the model, while $j_{\rm min}$ is set to be a fixed fraction of $j_{\rm max}$. For an exponentially decreasing accretion rate, the initial angular momentum will have a significant impact on the size of the disc. In our model $j_{\rm min} = j_{\rm max}/10$ will be used, after experimentation showed that for significantly smaller values of $j_{\rm min}$ the early discs are compressed too much, while for higher values the growth of j and $R_{\rm eff}$ was found to be too shallow (further discussed in section 5.1.3).

The specific angular momentum of the accreting gas is used to infer the radial scale length $R_{\rm acc}$. The specific angular momentum of any disc component is determined by its surface density profile and rotation velocity at a given time:

$$j(t, R < R_{\rm max}) \equiv \frac{2\pi \int_0^{R_{\rm max}} \Sigma(t, R') v_{\rm rot}(t, R') R'^2 dR'}{2\pi \int_0^{R_{\rm max}} \Sigma(t, R') R' dR'}, \tag{34}$$

where $R_{\rm max}$ is the maximum radius of the disc. For the accreted gas, the surface density is given by eq. (31). The Newton-Raphson method is applied to numerically find $R_{\rm acc}$ for a given value of $j_{\rm acc}$. The rotation velocity depends on the structure and angular momentum of the CGM, which are not explicitly modelled in this evolution model. The CGM can influence the angular momentum of accreting gas through mixing, torques, or misalignment with the disc. For simplicity, we assume the infalling gas co-rotates with the disc. We will separately investigate the impact of a local angular momentum deficit, or equivalently a rotation velocity deficit of the infalling gas with respect to the disc (see section 2.3).

2.3 Radial flows

Radial flows impact the structural and dynamical evolution of galactic discs. The redistribution of gas can affect the SFR in different regions and the distribution of angular momentum, among others. To reproduce observed metallicity gradients in chemical evolution models, radial flows appear to be required (Schönrich & Binney, 2009). Subsequently, metallicity gradients can also be used to constrain radial flows in galaxies (Pezzulli & Fraternali, 2016). One of the possible mechanisms that can drive radial flows is the local conservation of angular momentum during gas accretion. When gas is accreted from the hot CGM, which is pressure-supported due to its high temperature ($T \sim 10^6$ K), it typically possesses lower specific angular momentum than the disc at the same radius. As this low angular momentum gas settles onto the disc, it induces an inward radial flow to conserve total angular momentum. The analytic formalism describing this effect has been introduced by Mayor & Vigroux (1981) and extended on by Pitts & Tayler (1989).

The radial flows model of Pitts & Tayler (1989) assumes that an instantaneous centrifugal equilibrium is reached in the disc when gas is accreted. This assumption is only valid when the rotation velocity dominates over the radial velocity. Due to high expected gas accretion rate and fast halo growth at early times, and the high angular momentum and fast increase in density in the outer regions in an inside-out growing disc, this prescription for radial flows breaks down in the very early stages of the evolution model or in the outer regions of the galaxy. Under the conservation of angular momentum, the radial velocity of the gas $u_{\rm R,gas}$ is given by

$$u_{\rm R,gas}(t, R) = \frac{\partial R}{\partial t} = \frac{-[\dot{\Sigma}_{\rm acc}(t, R)\,(j_{\rm disc}(t, R) - j_{\rm acc}(t, R)) + \Sigma_{\rm gas}(t, R)\frac{\partial j_{\rm disc}(t,R)}{\partial t}]}{\Sigma_{\rm gas}(t, R)\frac{\partial j_{\rm disc}(t,R)}{\partial R}}, \tag{35}$$

where $\dot{\Sigma}_{\rm acc}$ is the accretion rate from the CGM, $\Sigma_{\rm gas}$ is the gas density, $j_{\rm disc}$ is the specific angular momentum of the disc, and $j_{\rm acc}$ the specific angular momentum of the accreted gas. The term on the l.h.s. is determined by the specific angular momentum mismatch between that of the disc $j_{\rm disc}(t, R)$ and that of the accreting gas $j_{\rm acc}(t, R)$. The term on the r.h.s. is governed by the change in angular momentum of the disc ($\partial j_{\rm disc}/\partial t$). The $\partial j_{\rm disc}/\partial t$ term is often omitted in models (e.g Mayor & Vigroux, 1981; Pezzulli & Fraternali, 2016), however, it can dominate during the early stages of evolution when the DM halo is still actively growing and a significant amount of gas is accreted onto the disc. It can also become important once a galaxy has reached a low gas fraction, and there is a minimal mismatch between $j_{\rm disc}$ and $j_{\rm acc}$. The $\partial j_{\rm disc}/\partial t$ term is also important for the stellar component of the disc, which is not directly impacted by the gas accretion. However, the change in $M_{\rm vir}$, and subsequently v_c, do induce radial flows in the stellar disc. The resulting radial drift velocity of the stars is given by

$$u_{R_\star}(t, R) = -\frac{\partial j_{\rm disc}(t, R)/\partial t}{\partial j_{\rm disc}(t, R)/\partial R}. \tag{36}$$

When computing the radial flows at a given time step in the model for a given annulus at radius R of the disc, we approximate and simplify the expression of $j_{\rm disc}(t, R)$ as follows:

$$\begin{aligned} j_{\rm disc}(t,R) &\equiv \frac{2\pi \int_R^{R+dR} \Sigma(t,R') v_{\rm rot}(t,R') R'^2 dR'}{2\pi \int_R^{R+dR} \Sigma(t,R') R' dR'} \\ &\approx \frac{\Sigma(t,R) v_{\rm rot}(t,R) R^2 dR}{\Sigma(t,R) R dR} \\ &\approx v_{\rm rot}(t,R) R \end{aligned} \tag{37}$$

Hence, the specific angular momentum of a single annulus is solely dependent on its rotation velocity and radius. To implement the radial flows in the model, their effect on the stellar and gas surface density profiles needs to be derived. The radial mass flux μ of each component is given by (Pezzulli & Fraternali, 2016)

$$\mu(t,R) = 2\pi R \Sigma(t,R) u_R(t,R), \tag{38}$$

where $\Sigma(t, R)$ is the surface density, and $u_R(t, R)$ is the radial velocity of the respective component of the mass flux. The effective accretion rate $\dot{\Sigma}_{\rm eff}$ gives the total amount of gas mass that flows in and out of an annulus of the disc as follows

$$\dot{\Sigma}_{\rm eff} = \dot{\Sigma}_{\rm acc} - \frac{1}{2\pi R} \frac{\partial \mu}{\partial R} \tag{39}$$

$$= \dot{\Sigma}_{\rm acc} - \frac{1}{R} \frac{\partial}{\partial R} (R\, u_R \Sigma_{\rm gas}) \tag{40}$$

where the first term is the gas that is accreted onto the disc from the CGM (eq. (31)), the second term gives the change in net surface density as a consequence of inflows and outflows from and to adjacent annuli.

2.4 Star formation law

The amount of star formation in a galaxy is inherently linked to the amount of cold gas that is available to form stars. The Kennicutt-Schmidt (KS) law, links the star formation rate $\Sigma_{\rm SFR}$ with the gas surface density $\Sigma_{\rm gas}$, with a power law $\Sigma_{\rm SFR} \propto \Sigma_{\rm gas}^n$, where $n \approx 1.4$ (Kennicutt, 1998). This empirical relation is important in the modelling of the SFR. However, at low surface densities, the KS law breaks down, overestimating the SFR (Bacchini et al., 2019). The cold, dense ISM, becomes inefficient in forming and sustaining star formation at these lower densities, which occurs in low surface brightness systems and outer regions of galaxies. This breakdown may be related to the increasing vertical thickness of the gas disc, which reduces the local volume density even if the surface density remains relatively high. Bacchini et al. (2019) showed that this effect disappears when using a volumetric star formation law instead. Nevertheless, for simplicity, we adopt surface densities here. To account for suppressed star formation at low gas densities, we apply a modified KS law with a low-density threshold, adapted from Schönrich & Binney (2009):

$$\Sigma_{\rm SFR} = \begin{cases} \kappa \Sigma_{\rm gas}^{n_1} & \Sigma_{\rm gas} > \Sigma_{\rm cut-off} \\ \kappa (\Sigma_{\rm cut-off})^{n_1 - n_2} \Sigma_{\rm gas}^{n_2} & \text{otherwise,} \end{cases} \tag{41}$$

where n_1 is the standard KS slope, $n_1 = 1.4$ and n_2 is the cut-off slope $n_2 = 4.0$. The cut-off surface density is set to be $\Sigma_{\rm cut-off} = 0.004 \times 10^9\, {\rm M}_\odot\, {\rm kpc}^{-2}$ and the prefactor $\kappa = 2.2 \times (10^9\, {\rm M}_\odot)^{1-n_1}\, {\rm Gyr}^{-1}$, called "absolute star formation efficiency" by Kennicutt (1998).

To model how the SFR impacts the stellar and gas surface densities, stellar feedback also needs to be considered, or specifically the rate at which gas is returned to the ISM by stars. In general this

depends on the time delay from the star formation, the IMF and the SFR a the time the population was born. The mass return rate is given by

$$\dot{M}_{\rm ret}(t) = \int_{m_{\rm min(t)}}^{m_{\rm max}} SFR[t - \tau_{\rm MS}(m)]\phi(m)[m - m_{\rm rem}(m)]dm, \tag{42}$$

where $\tau_{\rm MS}$ is the main sequence time of a star i.e. the lifetime of a star, $m_{\rm rem}$ is stellar remnant mass, and $\phi(m)$ is the IMF (e.g. Chabrier, Kroupa or Salpeter) (Tinsley, 1980). Therefore $SFR[t - \tau_{\rm MS}(m)]$ describes the SFR at time the stars formed, and $m - m_{\rm rem}(m)$ the mass returned to the ISM.

In this model, we will assume the instantaneous recycling approximation (IRA), which assumes a fraction of the gas is instantaneously returned to the ISM when stars form. The reduced star formation rate $\Sigma_{\rm rSFR}$ accounts for this and is given by

$$\Sigma_{\rm rSFR} = (1 - \mathcal{R})\Sigma_{\rm SFR}, \tag{43}$$

where $\mathcal{R}$ is the return factor, defined as

$$\mathcal{R} = \int_{m_{\rm min}}^{m_{\rm max}} \phi(m)[m - m_{\rm rem}(m)]dm. \tag{44}$$

Within the IRA it is assumed that the life cycle of massive stars is negligible compared to timescales considered in the model ($\tau_{\rm MS} = 0$), while low-mass stars are assumed to live forever. The value of $\mathcal{R}$ is therefore dependent on the initial mass function (IMF) of the initial stellar population. In this thesis, we assume a Salpeter IMF, for which $\mathcal{R} = 0.3$ (Fraternali & Tomassetti, 2012), this assumption is further discussed in section 5.1.5.

2.5 Self-consistent rotation velocity

To model the kinematic evolution of our modelled galaxies, the rotation velocity as a function of the galactocentric radius needs to be computed. For kinematically cold matter components, the rotation velocity closely approximates the circular speed. The circular speed can be determined directly from the gravitational potential $\Phi(R, z)$ under the assumption of equilibrium and system being axisymmetric. Therefore, the total rotation curve can be constructed by summing the contributions from different mass components:

$$v_c^2(R) = R\left(\left.\frac{\partial\Phi_\star}{\partial R}\right|_{z=0} + \left.\frac{\partial\Phi_{\rm gas}}{\partial R}\right|_{z=0} + \left.\frac{\partial\Phi_{\rm DM}}{\partial R}\right|_{z=0}\right) \tag{45}$$

$$= v_\star^2(R) + v_{\rm gas}^2(R) + v_{\rm DM}^2(R) \tag{46}$$

where, $v_c(R)$ is the total circular speed, and $v_\star(R)$, $v_{\rm gas}(R)$, and $v_{\rm DM}(R)$ are the effective contributions to the rotation curve from the stellar, gas, and dark matter potentials, respectively.

The circular velocity of the DM component is given by eq. (25). Since the baryonic surface densities are computed numerically, they lack an analytic form. Therefore, to obtain the circular velocity contributions of these components, they need to be computed numerically directly from the surface density profiles. To achieve this, we use a Python code adapted from `vcdisk`[1] (Posti, 2022). The method used to compute the circular velocity is based on Casertano (1983) using the radial force in the disc $F_{\rm disc}(R)$:

$$v_{\rm disc} = \sqrt{-RF_{\rm disc}(R)}, \tag{47}$$

where $F_{\rm disc}(R)$ is defined as follows

$$F_{\rm disc}(R) = 4\pi G\int_0^\infty {\rm d}u\int_0^\infty {\rm d}z\; 2\sqrt{\frac{u}{Rp}}\frac{\mathcal{K}(p) - \mathcal{E}(p)}{\pi}\frac{\partial\rho(u,z)}{\partial u}, \tag{48}$$

[1]Documentation `vcdisk`: https://vcdisk.readthedocs.io/en/latest/#

where $\mathcal{K}$ and $\mathcal{E}$ are elliptic integrals, $p = x - \sqrt{x^2 - 1}$ and $x = (R^2 + u^2 + z^2)/(2Ru)$. u and z are elliptical coordinates used to describe the distribution of matter in the disc, given by the density $\rho(u, z)$. For an axisymmetric disc, the 3D density can be separated into a product of the radial surface density profile and a normalized vertical profile:

$$\rho(R, z) = \frac{\Sigma(R)\rho_z(z)}{N}, \tag{49}$$

where N is a normalisation factor related to $\rho(z)$ by $N = \int \mathrm{d}z\rho(z)$. For the vertical density, the profile of van der Kruit & Searle (1981) will be assumed, which is given by $\rho_z(z) = \cosh^{-2}(z/z_0)$, with a corresponding normalisation of $N = 2z_0$. A scale height of $z_0 = 0.3$ kpc is assumed for the gas and stellar disc. This is an arbitrary choice, based on the scale height of the Milky Way's thin disc, that has little impact on the resulting rotation curve. An example of a rotation curve, decomposed in its different contributions, is shown in fig. 7.

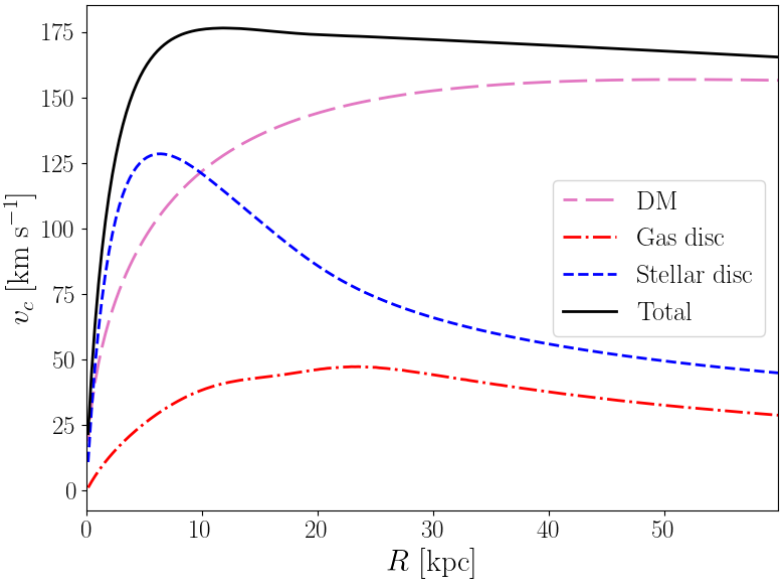

Figure 7: Decomposed rotation curve, showing the contributions from the stellar disc, gas disc and DM halo.

2.6 Initializing the model & numerical details

The previous sections outlined the various components of our galaxy evolution model. Here, we describe the numerical implementation and how the model is initialized. Within the model, the surface density profile, mass and specific angular momentum of the gas, stellar, and baryonic component are calculated for each time step. However, to quantify their radial and temporal dependence, the disc must be divided into annuli, and a time-stepping scheme must be defined.

2.6.1 Initialize the model

To trace different parameters in the resolved model, the galactic disc is defined in terms of annuli, spanning from $R = 0$ to $R = R_{\mathrm{max}}$, each characterised by a radius R and width ΔR. The number of annuli is set to $N_{\mathrm{radii}} = 200$. However, the maximum radius of the disc is varied based on galaxy mass to best resolve evolutionary processes. From the size-mass relation (section 1.2.5) we know that the size of the disc increases over time and with increasing mass. Using the scaling of this relation (eq. 7), a rough estimate of the required maximum radius can be made. The total

baryonic mass of the disc at $z = 0$, is approximated by the total amount of accreted gas $M_{\rm acc}(t_0)$ (eq. 32). However, the baryonic mass of the actual disc will always be slightly smaller than the total accreted gas, as the gas is assumed to accrete up to an infinite radius due to the exponential distribution of the accreted gas, while the baryonic mass is defined as the mass contained within $R_{\rm max}$. The maximum radius $R_{\rm max}$ is subsequently given by scaling the effective radius expected from the size-mass relation by 20:

$$R_{\rm max} \approx 10^{0.4+0.25(\log M_{\rm acc}(t_0)-10.3)} \times 20 \quad \text{kpc}. \tag{50}$$

For relatively high values of $j_{\rm max}$ and/or negative values of $\omega_{\rm acc}$ it can occur that the accreting radial scale length $R_{\rm acc}$ exceeds the maximum radius. Consequently, the specific angular momentum of the accreted gas that is considered within the limits of the model, will be much lower than the specified value for $j_{\rm acc}$ at those time steps, leading to extreme values of $R_{\rm acc}$ as the model attempts to compensate for the missing mass. To solve this issue, when for a set of parameters $R_{\rm acc}(t) > R_{\rm max}$, the model is halted and the maximum radius will be doubled, and the model is re-run. If $R_{\rm acc}(z = 0)$ remains too large after doubling $R_{\rm max}$ twice, the output of the model for that set of parameters will be considered invalid. In these cases, the size of the disc and $R_{\rm acc}$, far exceed realistic values.

The evolution model starts at a redshift of $z_{\rm start} = 10$, corresponding to a cosmic time of $t_{\rm c,start} \approx 0.47$ Gyr. Within the model, time is defined to run from $t = 0$ to $t = t_0$. For $z_{\rm start} = 10$, the model stops at $t_0 \approx 13.32$ Gyr (lifetime universe - $t_{\rm start}$). The galactic disc starts off with zero initial mass at $t = 0$. The DM halo is established at this time, at a given halo seed mass. As the DM halo evolves independently of the disc, following eq. (17), the initial halo mass is solely defined by $z_{\rm start}$ and $M_{\rm DM}(z = 0)$ (see section 2.1.1).

As explained in section 2.3, the radial flows in the initial stages of the model can become infinitely great in the used formalism, which assumes that instantaneous centrifugal equilibrium can be reached at each time step. To avoid problems with this, the radial flows are omitted in the first stage of the model. The radial flows are set to start at a redshift of $z_{\rm flows} = 7$, giving the model time to accrete mass and form a disc from the zero initial mass it started with. After this time, the time step becomes dynamic to account for the time needed to transport mass between different annuli (see section 2.6.2). The initial time step size is set to be $\Delta t = t_0/2000$.

Parameter	Units	Value	Ref.
$M_{\rm DM}(t_0)$	$\rm M_\odot$	Independent	eq. (17)
$M_{\rm acc}(t_0)$	$\rm M_\odot$	Free	eq. (32)
$\omega_{\rm acc}$	$\rm Gyr^{-1}$	Free	eq. (32)
$j_{\rm max}$	$\rm kpc\,km\,s^{-1}$	Free	eq. (33)
$j_{\rm min}$	$\rm kpc\,km\,s^{-1}$	$j_{\rm min} = j_{\rm max}/10$	eq. (33)
n		0.3	eq. (33)
α		0.0	$\alpha = j_{\rm acc}/j_{\rm disc}$, eq. (35)
$\mathcal{R}$		0.3	eq. (44)

Table 2: Input parameters of the model

2.6.2 Implementation radial flows & dynamical time step

The radial flows are implemented according to eqs. (35) and (36). The time derivative $\partial j_{\rm disc}/\partial t$ is computed using a third-order backward finite difference approximation (Landau et al., 2015). This is appropriate because the model is causal, i.e. we only have access to the current and previous time steps, not future ones. Backward differences estimate the derivative at the current time step t_n using function values at earlier times $t_n, t_{n-1}, \ldots, t_{n-k}$, where k is the order of the

approximation. The third-order backward difference takes the general form:

$$\left.\frac{\partial f}{\partial t}\right|_{t_n} \approx \sum_{i=0}^{3} a_i \, f(t_{n-i}), \tag{51}$$

where $f(t)$ is a generic function, the coefficients a_i depend on the spacing of the time steps and are computed from polynomial interpolation—specifically, using Lagrange basis functions constructed over the last $k+1$ time points, in our case $k = 3$. The implementation dynamically calculates these coefficients to support non-uniform spacing between time steps. The radial derivative $\partial j_{\rm disc}/\partial R$ (see eqs. (35) and (36)) is computed using the second-order central difference (Landau et al., 2015).

In the outer regions of the modelled galaxies, the radial velocity can reach unphysical values. To avoid these, a limit is placed based on the surface densities of the stellar and gas components. Where $\Sigma_{\rm gas} > 10^{-2}$ $\mathrm{M_\odot\,pc^{-2}}$ and $\Sigma_\star > 10^{-9}$ $\mathrm{M_\odot\,pc^{-2}}$, the radial velocity for each component is fixed to the last valid value encountered before the surface density dropped below the specified threshold (fig. 8). The placement of these limits makes a negligible difference, as very little mass is present in these regions. A stricter threshold is used for the gas component as its radial velocities are greater in the presence of an angular momentum mismatch.

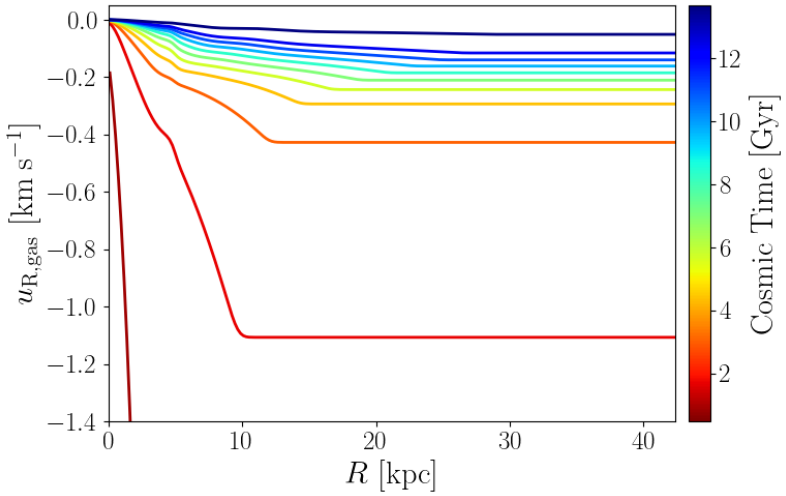

Figure 8: Example of the evolution of the radial velocity of the gas component, where the radial velocity curve is set to remain constant for $\Sigma_{\rm gas} > 10^{-2}$ $\mathrm{M_\odot\,pc^{-2}}$.

The numerical differentiation and integration methods used in the model can create systematic errors that blow up over time. To solve this, $u_{\rm R,gas}$ and $u_{\rm R,\star}$ are smoothed using a 1D Gaussian filter. This removes artificial dips in the radial flows of single annuli compared to adjacent annuli. For the smoothing, a higher weight is assigned to the inner annuli, to make sure that the radial flows in the region, where most mass is concentrated, are changed the least. The impact on the resulting mass fluxes is minimal and it ensures that there is no build up of systematic numerical errors.

Similarly, the log surface densities $\Sigma_{\rm gas}$ and $\Sigma_\star$ are smoothed too, however using a different method, namely using a cubic smoothing B-spline. This method is more adept at handling data that spans a large range of values. In early time steps, the surface densities can span more than 300 orders of magnitude, due to the steep exponential accretion profile and the relatively small size of the disc compared to $R_{\rm max}$. If the surface densities reach a floating-point underflow, it can produce a `NaN` in Python. To avoid this, surface densities below 10^{-300} $\mathrm{M_\odot\,pc^{-2}}$ are assigned the minimum value of 10^{-300} $\mathrm{M_\odot\,pc^{-2}}$. At these densities, the disc is essentially non-existent, hence

this condition will have no effect on the outcome of the model and helps prevent computational issues with `NaN`'s in Python.

Finally, after having applied the radial mass flows (section 2.3), the surface densities are corrected for the minor change in mass as a consequence of the numerical systematic error in the implementation of the smoothing. These processes should not impact the total mass of the disc. The correction factor $f_{\rm corr}$ is given by

$$f_{\rm corr} = \frac{M}{M + \Delta M}, \quad \text{where} \quad \Delta M = 2\pi \int_0^{R_{\rm max}} \left(\frac{1}{R} \frac{\partial}{\partial R} (R\, u_R \Sigma) \Delta t \right) R dR, \tag{52}$$

where the mass M, surface density Σ and radial velocity u_R correspond to either the stellar or gas component.

The mass transported by the radial flows needs to be able to reach the adjacent annulus within the time step Δt. The minimum time required for this is $\Delta R / \max(u_R)$, or following the Nyquist theorem, the sampling time step must satisfy $\Delta t \leq \frac{1}{2} \cdot \Delta R / \max(u_R)$. To this aim, we update the time step following

$$\Delta t = \min \left(\Delta t_{\rm max}, 0.9 \times \frac{\frac{1}{2} \cdot \Delta R}{\max(u_R)} \right) \tag{53}$$

where the maximum time step is set to $\Delta t_{\rm max} = t_0/500 \approx 27$ Myr. This maximum time step is greater than the initial time step of $\Delta t = t_0/2000$, under the assumption that a higher temporal resolution is needed at early times to accurately capture the fast growth of the disc and halo at these times. The time t at each iteration is saved and included as output of the model, such that the time evolution of the different parameters can be accurately represented.

2.6.3 Stopping conditions and output parameters

The evolution model is designed to run from $t = 0$ to $t = t_0$, where t_0 corresponds to $z = 0$. This way, the outcomes of the model can be compared to galaxies in the present day universe. In general, the model is designed to keep running until t reaches t_0. However, due to the dynamic time step, Δt can become extremely small when the radial velocity blows up. Despite the conditions put in place to prevent unphysical radial velocities in the early stages of evolution and in the outer regions of the galaxies, for some combinations of parameters they can still occur. To avoid excessive runtimes in these cases, a maximum number of iterations is imposed. The model terminates when the number of iterations exceeds $N_{\rm iter,max} = 4000$. This threshold is chosen based on the typical number of steps required to reach t_0, which lies between $\sim 500 - 800$ for the selected initial time step and the way the dynamic time step evolves. The chosen threshold is therefore safely above the expected range in normal cases, while still avoiding excessive runtimes when the model fails to progress. If t fails to reach t_0 within this limit, the model output for that parameter set is considered invalid

Our model automatically computes the following parameters: $M_{\rm DM}(t)$, $\Sigma_\star(t, R)$, $\Sigma_{\rm gas}(t, R)$, $M_\star(t)$, $M_{\rm gas}(t)$, $M_{\rm bar}$, $j_\star(t)$, $j_{\rm gas}(t)$, $j_{\rm bar}(t)$ and more. However, to compare the results of the model with the TFR and mass-size relations, we also require knowing the rotation velocity at the "flat" part of the rotation curve $v_{\rm flat}$, and the size of the disk R_e.

We define $v_{\rm flat}$ to be average circular speed within the region where $0.5 < \Sigma_{\rm gas} < 1.0\ {\rm M_\odot\,pc^{-2}}$, which approximately corresponds to typical values for the outer HI discs in observations. The size of the stellar and gas disc is characterized by their respective effective radius R_e. The effective radius is defined as the radius within which half the light of the galaxy is emitted. If a constant mass-to-light ratio is assumed for the entire disc, the half-light radius is equivalent to the half-mass radius. Hence, we take the effective radius to be the radius within which half of the total gas/stellar mass is contained.

2.7 Constraining model parameters

In this section, we describe how the free parameters of the model are constrained. Using local scaling relations, we are able to evaluate the accuracy of a galaxy produced by the model for a given set of free parameters based on its properties, in particular its baryonic mass, rotation velocity, gas fraction, angular momentum and disc size. Once local scaling relations are satisfactory reproduced, we investigate predictions for their evolution with time.

We constrain the free parameters of the model $\log M_{\rm acc}(t_0)$, $\omega_{\rm acc}$, $\log j_{\rm max}$ for a range of DM halo masses. We assume no angular momentum mismatch between the disc and the accreting gas (eq. (35)). Introducing a mismatch, increases the radial velocity of the gas, subsequently increasing the number of time steps required to model the evolution of a galaxy from $z = 10$ to $z = 0$, making it more computationally expensive. The 3 free parameters are constrained for the halo masses $\log(M_{\rm DM}/M_\odot)(t_0) = [10.25, 13.00]$, with steps of 0.25 dex. Three local relations are used to constrain the parameters: 1) the BTFR (Lelli et al., 2019), which links baryonic mass to $V_{\rm flat}$ and thereby to the DM halo; 2) the $j_{\rm bar} - M_{\rm bar} - f_{\rm gas}$ relation (Mancera Piña et al., 2021b), which constrains the gas accretion history through $f_{\rm gas}$ and the angular momentum growth; and 3) the stellar size–mass relation (van der Wel et al., 2014), which connects stellar mass to the radial distribution of stars. Together, these relations provide complementary constraints on $M_{\rm acc}(t_0)$, $\omega_{\rm acc}$ and $j_{\rm max}$.

The time evolution of the angular momentum growth of the accreting gas is set to follow the powerlaw (eq. (33)) with $n = 0.3$. For powers $n \geq 1.0$ it was found that too much gas is being accreted in the inner regions at early times, leading to relatively smaller sizes of the discs. We tested to the model for $n = 1$ and found that to still obtain results that are in agreement with the stellar size-mass relation at $z = 0$, the model compensates by accreting the gas at later times, i.e. the model favours negative values of $\omega_{\rm acc}$. However, a declining accretion history and corresponding declining SFH is expected for most LTGs (Leitner, 2012). To account for this, we set $n < 1.0$, specifically $n = 0.3$, allowing for a fast increase in $j_{\rm acc}$, and consequently $r_{\rm acc}$, at early times.

To explore the parameter space, we assume the following prior range for the free parameters:

- $\log(M_{\rm acc}/M_\odot)(t_0)$ is set to vary from $[\log(M_{\rm DM}/M_\odot)(t_0) - 3, \log(M_{\rm DM}/M_\odot)(t_0) - 0.5]$. This broadly covers the range of values expected from the SHMR (section 1.2.7).
- $\log j_{\rm max}$ is varied ± 1 dex around the local $j_{\rm bar} - M_{\rm bar}$ relation, where $\log(M_{\rm acc}/M_\odot)(t_0)$ is assumed to correspond to $\log(M_{\rm bar}/M_\odot)(t_0)$.
- $\omega_{\rm acc}$ is varied between $[-0.5, 1.0]$ Gyr^{-1}. For lower halo masses ($\log(M_{\rm DM}/M_\odot) \leq 11.25$), the lower limit on the $\omega_{\rm acc}$ range is extended to -1.0 Gyr^{-1}, and for higher masses ($\log(M_{\rm DM}/M_\odot) \geq 12.25$) the upper limit is extended to 1.5 Gyr^{-1}, to better capture the distribution around the peak of the posterior.

Within each range, 20 linearly spaced values were used per parameter to explore the 3D space (or 26 for the extended ranges of $\omega_{\rm acc}$).

To finally constrain the free parameters, we run a Markov Chain Monte Carlo (MCMC) algorithm. Within the MCMC, the log-likelihood for a single modelled galaxy, for a given set free parameters, is approximated by

$$\log \mathcal{L} = -\frac{1}{2} \sum_i \left[\left(\frac{y_i^{\rm model} - y_i^{\rm s.r.}}{\sigma_{i,y}^{s.r.}} \right)^2 \right] \tag{54}$$

Where the sum is performed over the three different scaling relations used to constrain the parameters. $y_i^{\rm s.r.}$ and $\sigma_{i,y}^{s.r.}$ are the values and scatter of the respective scaling relations. To let the walkers in the MCMC algorithm freely explore the parameter space in a computationally efficient manner,

interpolation on the previously described 3D grid is applied. The prior is set using the best-fitting values on the grid. For each discrete value of a given free parameter, the prior is assigned as the maximum value of $-\sum_i[(y_i^{\rm model} - y_i^{\rm s.r.})/\sigma_{i,y}^{s.r.}]^2$, obtained when varying all possible combinations of the other two free parameters. Values outside the selected ranges of the free parameters, are given a prior of 0. The resulting prior distribution is then normalised so that its probability density function (PDF) integrates to unity. The resulting posterior distributions of each parameter from MCMC, are used to obtain the best-fit value and uncertainty of each free parameter, for a given DM halo mass.

3 Data

Scaling relations, in particular kinematic ones, are well constrained at $z = 0$ and will therefore be used to constrain the model. Based on the best-fit parameters we obtain the evolution of the scaling relations according to the model. Using the limited kinematic data that is available at $z > 1$, we can examine if it matches trend of the model.

The rotation of a galactic disc can be traced due to the Doppler effect, where one side will be blue shifted and the other side red shifted, with respect to the systemic velocity. This effect can be observed using emission or absorption lines. For nearby galaxies, the gaseous discs can be observed with the 21-cm line coming from HI emission. This line is ideal for tracing the rotation of the disc and probing the galactic potential, as the atomic gas is much more extended than the stellar component of the disc. However, this can only be done for nearby galaxies, due to observational limitations. At higher redshifts, other emission lines are needed. The CO, [CI] and [CII] transitions are a good alternative to trace the cold gas components of discs (Carilli & Walter, 2013). However, in contrast to the HI emission lines, CO emission traces the molecular gas instead of the atomic gas, which is less radially extended and therefore might not probe the full rotation curve. The sensitivity and resolution required to study the CO, [CI] and [CII] kinematics at higher redshifts makes the Atacama Large Millimeter Array (ALMA) the best instrument for these observations (Rizzo et al., 2023). A downside is the long integration time required for these emission lines, making the studied sample limited (Rizzo et al., 2024).

For this reason, many studies have also used line emissions that trace the warm ionized gas (Hα, [OII], [OIII]) as alternatives (e.g. Epinat et al., 2009; Stott et al., 2016; Di Teodoro et al., 2016; Simons et al., 2016; Turner et al., 2017; Übler et al., 2019). These emission lines need short observation times, so the current samples comprise hundreds of galaxies (e.g. Harrison et al., 2017; Wisnioski et al., 2019). The downside of these observations is that the warm ionised gas component is a poor tracer of the main gas component and is likely to be contaminated by non-circular motions like outflows (Kohandel et al., 2024; Parlanti et al., 2024), making it difficult to extract the main underlying rotation of the galactic disc. Therefore, in this thesis, only observations of cold gas tracers will be considered.

3.1 Observational data for higher redshifts

For resolved kinematic observations at $z > 0.5$, we compile a set of limited but diverse samples (table 3). The majority of our high-z galaxies come from the Archival Large Program to Advance Kinematic Analysis (ALPAKA) sample ((Rizzo et al., 2023)), for these galaxies we compute the total molecular mass and specific angular momentum (section 3.2). All galaxies in our high-z dataset are disc galaxies, biased towards high masses with $\log(M_{\rm bar}/M_{\odot}) \gtrsim 10.0$ and all have active star formation.

Sample overview:

- **ALMA-ALPAKA survey:** The ALMA-ALPAKA is a project that has gathered observations from the ALMA archive to study the kinematics of SFGs in the redshift range $0.5 - 3.5$, using spatially resolved observations of CO or [CI]. 19 of the 28 ALPAKA galaxies have been kinematically identified as rotating discs. Of these discs, 13 are in (proto)clusters, and 6 have an AGN or show hints of an AGN presence. Additionally, 8 have been identified as starburst galaxies, and 10 as main-sequence galaxies (Rizzo et al., 2023). The selection criteria, based on data quality, naturally bias the sample toward massive, actively star-forming systems. The surface brightness profiles of the stellar and gas components of these galaxies have been analysed by Frickmann (2022), using HST and ALMA observations, respectively. For the majority of the galaxies, the reddest HST band, F160w, was used to build the stellar surface brightness profile. The Sérsic profile parameters (effective radius and Sérsic index) listed in Frickmann (2022) are used to determine the surface density profiles of the ALPAKA galaxies in this thesis.

- **High-z [CII] galaxies:** Roman-Oliveira et al. (2023, 2024) study 4 massive star forming galaxies at redshift ~ 4.5, using ALMA observations of [CII] 158 μm. 3 are identified as starburst galaxies and 1 as a main-sequence galaxy.
- **Lensed [CII] galaxies:** 6 lensed galaxies at $z \sim 4.5$ from Rizzo et al. (2020, 2021), with [CII] ALMA observations. Of these, 5 are classified as starburst galaxies.
- **Individual galaxies:**
  - A massive starburst galaxy at $z = 4.75$, with [CII] ALMA observations by Lelli et al. (2021)
  - The "Big Wheel" galaxy at $z = 3.25$ and extremely extended disc with CO ALMA observations from Wang et al. (2025).

Reference	Data samples / Instrument	# galaxies	Kinematic tracer	$\log(M_{\rm bar}/M_\odot)$	Redshift
Rizzo et al. (2023); Rizzo et al. (2024)	ALMA-ALPAKA	17	CO, [CI]	$10.6 - 11.8$	$0.5 - 3.5$
Roman-Oliveira et al. (2023, 2024)	ALMA	4	[CII]	$10.5 - 11.5$	$4 - 5$
Rizzo et al. (2020, 2021)	ALMA	6	[CII]	$10.3 - 11.0$	$4 - 5$
Lelli et al. (2021)	ALMA	1	[CII]	~ 10.7	4.75
Wang et al. (2025)	ALMA	1	CO(4-3)	~ 11.7	3.25

Table 3: Datasets of high-redshift galaxy kinematics used in this thesis

3.2 Physical parameters for the high-z samples

In this section we will describe how the gas mass and angular momenta are computed for the ALPAKA sample (section 3.2.1). For the other data samples, instead of using the rotation curves, we use an approximation of the angular momentum described in section 3.2.2.

3.2.1 $M_{\rm H_2}$ and j computation - ALPAKA sample

To compute the molecular gas masses for the ALPAKA galaxies we use the following equation:

$$M_{\rm H_2} = L_{\rm CO} r_l \alpha_{\rm CO}, \tag{55}$$

where r_l is the luminosity line ratio, and $\alpha_{\rm CO}$ is the CO-to-H_2 conversion factor (Bolatto et al., 2013). $\alpha_{\rm CO}$ is a poorly constrained parameter that varies with gas density, temperature, and metallicity of the environment (Schinnerer & Leroy, 2024). Here we adopt different ranges for main sequence and starburst galaxies based on estimates from literature: $\alpha_{\rm CO}$ is allowed to vary uniformly, in a Monte Carlo (MC) computation, between $3.0 - 4.0\ {\rm M}_\odot\ 10^{-10}\ {\rm K\,km\,s^{-1}\,pc^2}$ (Daddi et al., 2010) for main sequence galaxies, and between $0.8 - 3.2\ {\rm M}_\odot\ 10^{-10}\ {\rm K\,km\,s^{-1}\,pc^2}$ for starburst galaxies (Kirkpatrick et al., 2019). The luminosity line ratios r_l are taken from Boogaard et al. (2020), where the line ratios for different CO transition in different redshift ranges are presented. Molecular gas masses and uncertainties are then obtained via a MC approach: luminosities and line ratios are drawn from Gaussian distributions reflecting their measurement errors, while $\alpha_{\rm CO}$ is drawn from the uniform ranges above.

The specific angular momentum of the ALPAKA galaxies is computed using eq. (3). For the surface density profile of the (molecular) gas and stellar component we take their respective surface brightness profiles, assuming a constant mass-to-light ratio. The surface density profiles are

extrapolated from the Sérsic index and effective radius of the profiles, determined by Frickmann (2022). Not for all galaxies do we have information on the optical surface brightness, hence j is only computed for the component for which the Sérsic profile is known. For the rotation velocity, the rotation curves of Rizzo et al. (2023) are used. The number of resolution elements in the rotation velocity curves range from 2-5. The curves are extended assuming they remain flat after the last data point. The gas and stellar component are assumed to have the same rotation velocity.

The specific angular momentum is computed within a maximum radius that extends far beyond the radii for which rotation curves are observed, as a significant fractions of the disc's angular momentum resides in the outer regions where surface densities are below the CO detection limit. Beyond a certain radius, j is expected to reach an asymptote, due to extremely low surface densities at these radii (Marasco et al., 2019). However to get a lower limit on j, we assume the disc truncates at the last value of the rotation curve, i.e. the surface density drops to zero beyond this radius. This radius should roughly coincide with the outer most observable radius of a galaxy. This choice ensures that only regions where the kinematics are observationally constrained are included, and it avoids introducing uncertain extrapolations into the faint outer disc. The uncertainties in j are computed using a standard MC algorithm, taking into account the uncertainties in the effective radius, Sérsic index and the rotation velocity in the individual resolution elements. The rotation curves, surface brightness profiles and the resulting angular momentum in the different mass components is shown in fig. 9. The values of j in the different mass components are presented in table 4.

3.2.2 Angular Momentum approximation

For other high-z data, we use an approximation for a quick estimate of their angular momentum, which is not reliant on the full rotation curve or surface density profiles. For this we use the approximation of the specific angular momentum by Romanowsky & Fall (2012)

$$j = k_n V_{\rm flat} R_{\rm eff}, \tag{56}$$

where $V_{\rm flat}$ the asymptotic rotation velocity, assumed to be the rotation velocity in the outer regions ($V_{\rm ext} \approx V_{\rm flat}$), and $R_{\rm eff}$ is the effective radius. The coefficient k_n is a function of the Sérsic index n, given by the following approximation:

$$k_n \approx 1.15 + 0.029n + 0.062n^2. \tag{57}$$

For the galaxies in our high-z sample, aside from the ALPAKA sample, only the galaxies of Roman-Oliveira et al. (2023) have reliable effective radii and Sérsic indices. When applied to the ALPAKA galaxies, the resulting estimate of j was found to deviate $< 10\%$ on average from the other method that uses the full rotation profiles, for density profiles with $n < 3$. For profiles with a higher Sérsic index, the approximation tends to overestimate j compared to the other method due to the extended outer wings in these profiles.

The angular momentum of the baryonic component (molecular gas + stars) is defined as

$$j_{\rm bar} = f_{\rm gas} j_{\rm gas} + (1 - f_{\rm gas}) j_\star, \tag{58}$$

where $j_{\rm gas}$ and $j_\star$ are the specific angular momentum of the gas and stellar component respectively, and $f_{\rm gas}$ is the gas fraction ($f_{\rm gas} = M_{\rm gas}/M_{\rm bar}$).

Galaxy ID	$j_\star$ $[10^3\,\mathrm{kpc\,km/s}]$	$j_{\mathrm{H_2}}$ $[10^3\,\mathrm{kpc\,km/s}]$	j_{bar} $[10^3\,\mathrm{kpc\,km/s}]$
1	$1.093^{+0.004}_{-0.003}$	$1.398^{+0.028}_{-0.027}$	$1.168^{+0.008}_{-0.007}$
2	$1.326^{+0.017}_{-0.018}$	$0.455^{+0.008}_{-0.009}$	$1.247^{+0.016}_{-0.016}$
3	$1.631^{+0.077}_{-0.069}$	$1.031^{+0.020}_{-0.020}$	$1.577^{+0.070}_{-0.063}$
6	$0.934^{+0.024}_{-0.022}$	$0.507^{+0.452}_{-0.257}$	$0.778^{+0.167}_{-0.098}$
7	—	$0.735^{+0.015}_{-0.015}$	—
8	$2.41^{+0.12}_{-0.12}$	$1.965^{+0.038}_{-0.034}$	$2.242^{+0.078}_{-0.079}$
9	$1.84^{+0.10}_{-0.10}$	$1.965^{+0.083}_{-0.087}$	$1.897^{+0.068}_{-0.065}$
11	$2.801^{+0.035}_{-0.035}$	$3.91^{+0.11}_{-0.11}$	$3.340^{+0.054}_{-0.052}$
13	$3.8^{+1.1}_{-1.2}$	—	—
19	$2.29^{+0.23}_{-0.23}$	$0.86^{+0.11}_{-0.11}$	$1.66^{+0.15}_{-0.13}$
20	$3.5^{+1.0}_{-1.1}$	$0.788^{+0.010}_{-0.011}$	$3.17^{+0.87}_{-0.92}$
22	$1.728^{+0.060}_{-0.061}$	$1.095^{+0.033}_{-0.036}$	$1.618^{+0.049}_{-0.052}$
23	—	$2.922^{+0.057}_{-0.052}$	—
25	$1.57^{+0.12}_{-0.12}$	$0.794^{+0.027}_{-0.025}$	$1.360^{+0.089}_{-0.083}$
BRI1335-0417	$1.24^{+0.65}_{-0.63}$	$0.63^{+0.14}_{-0.13}$	$1.11^{+0.57}_{-0.51}$
J081740	$2.5^{+1.4}_{-1.4}$	$0.99^{+0.21}_{-0.21}$	$1.8^{+1.1}_{-0.9}$
SGP38326-1	$4.6^{+2.9}_{-2.7}$	$2.18^{+0.25}_{-0.29}$	$3.0^{+1.2}_{-1.0}$
SGP38326-2	$2.1^{+1.6}_{-1.5}$	$1.22^{+0.13}_{-0.15}$	$1.34^{+0.41}_{-0.26}$

Table 4: Angular momentum values for the ALPAKA galaxies (labelled by their ID number), and the galaxies from Roman-Oliveira et al. (2023)

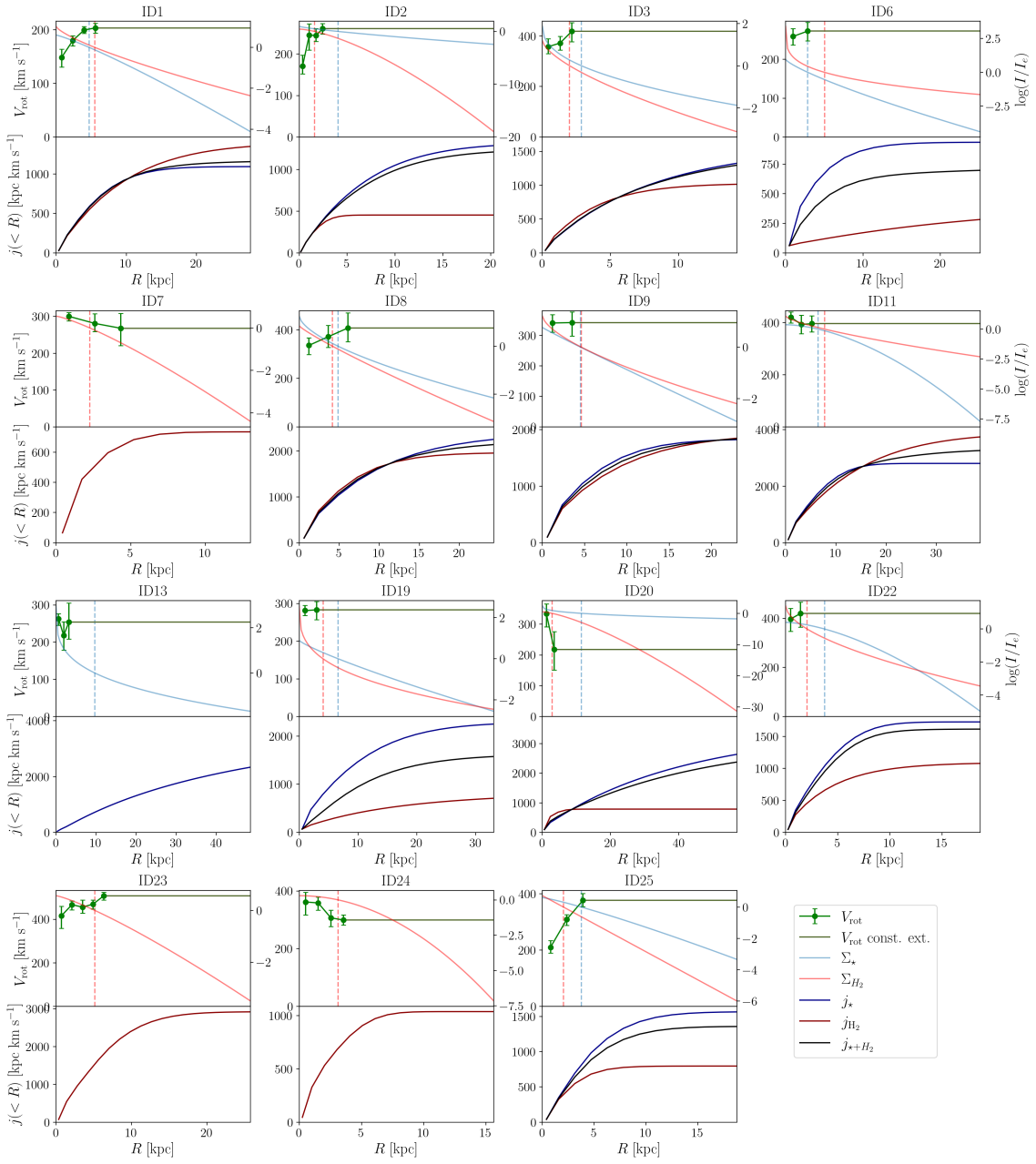

Figure 9: *top panels:* the rotation velocity profile of the ALPAKA galaxies (Rizzo et al., 2023) in green, with the extrapolated constant extension from the last data point. The surface brightness profiles of the stellar (blue), and molecular gas (H_2) component (red), scaled by the effective surface brightness. The dashed vertical lines indicate the effective radius of their respective mass component (assumed to be the same as the surface brightness). *bottom panels:* The specific angular momentum of the stellar (blue), H_2 (red), and combined (black) component.

3.3 High-z galaxies compared to local scaling relations

In section 1.2 the local (baryonic) Tully Fisher relation and the specific angular momentum - mass relation are presented. They are well-defined for the local universe, however it is unclear how they evolve and even whether they hold up at higher redshifts. In this section, we present the local of our selected high-redshift galaxies, with resolved observations of the cold gas kinematics (see section 3.1), compared to the local scaling relations.

In fig. 10 we show the local TFR (left panel) and BTFR (right panel) from Lelli et al. (2016b) as solid black lines, together with the high redshift galaxies to compare their positions with respect to the local scaling relations. Due to low resolution of the rotation curve for the majority of the galaxies, the velocity at the outer observed regions of the galaxies, the external circular speed $V_{\rm ext}$, is used as a substitute of $V_{\rm flat}$, and is used in the local relations. The majority of the galaxies are located below the local TFR, outside the 1σ bounds. This indicates a relatively lower stellar mass and higher circular speed with respect to the local relation. No clear trend between redshift and the distance from the local relation can be observed.

In the $M_{\rm bar} - V_{\rm flat}$ plane, the high redshift galaxies are closer to the local BTFR compared to what happens in the $M_\star - V_{\rm rot}$ plane with the TFR. Similarly to the TFR, the scatter in redshift is high, potentially suggesting a diverse evolution path of these galaxies. Isolating the galaxies based on environment, AGN presence, and star formation main sequence or starburst, also indicate no clear behaviour with redshift within these small subsamples.

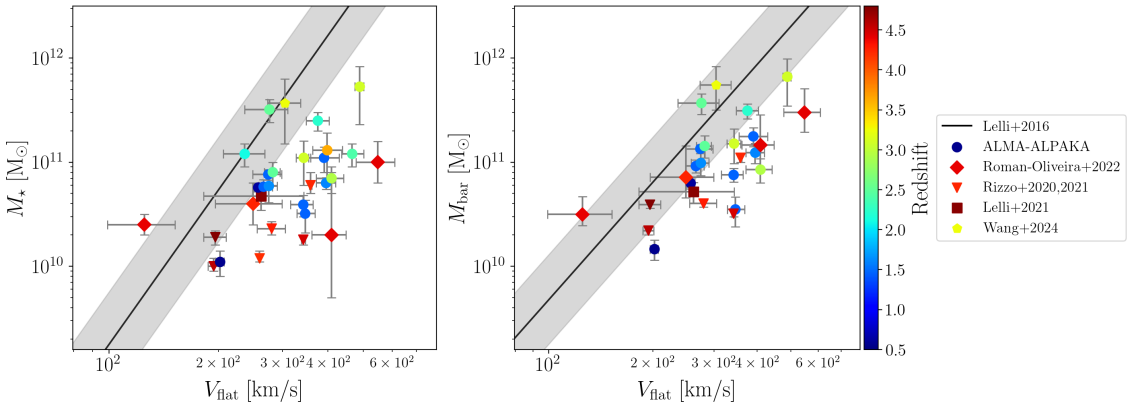

Figure 10: The Tully-Fisher relation *(left)* and the baryonic Tully-Fisher relation *(right)*, where the respective masses are plotted against the external circular speed. The high redshift galaxies are coloured according to their redshift. The local relations ($z \approx 0$) are fits to the data of Lelli et al. (2016a), with the intrinsic scatter indicated by the grey band.

In fig. 11 we show the local specific angular momentum - mass relations for the stellar, gas and baryonic component of disc galaxies as dashed black lines (Mancera Piña et al., 2021a). The local $j_{\rm H_2} - M_{\rm H_2}$ relation (Geesink et al., 2025) is shown as a solid black line the middle panel. With the available high-z data, only the mass and kinematics of the molecular gas can be obtained, while the relations at $z = 0$ are based on HI. Due to lack of observations of the atomic gas at these redshifts (Bera et al., 2023; Chowdhury et al., 2023; Zhang et al., 2021), we do not make assumptions and consider only the molecular gas component. The baryonic component is taken to be the sum of the stellar and molecular gas component.

Within our high-z sample, the angular momentum could only be computed for a limited amount of galaxies, due to the lack of data available on their density profiles. For the stellar and baryonic component, the high-z galaxies lie close to the local relation. Comparing the high redshift galaxies to the local $j_{\rm gas} - M_{\rm gas}$, we observe that they lie below the relation, having a significantly lower specific angular momentum for a given mass. This can be partially clarified by the ignored HI component of the discs. The HI disc is likely to be more extended than the

concentrated H_2 distribution within the discs, hence incorporating the atomic gas would likely bring these galaxies closer to the local relation. To make a more fair comparison to local galaxies, we make the comparison with the local $j_{\mathrm{H_2}} - M_{\mathrm{H_2}}$ relation. The majority of the high redshift galaxies, also lie below, but much closer to this relation, having, on average, a smaller j_{gas} at a certain M_{gas}. Additionally, the molecular masses for high-z galaxies have a high uncertainty, because we only have observations of high-J CO transition or [CII] for the majority of them. Similar to the Tully-Fisher relations, no trend between redshift and distance from the local relations can be discerned.

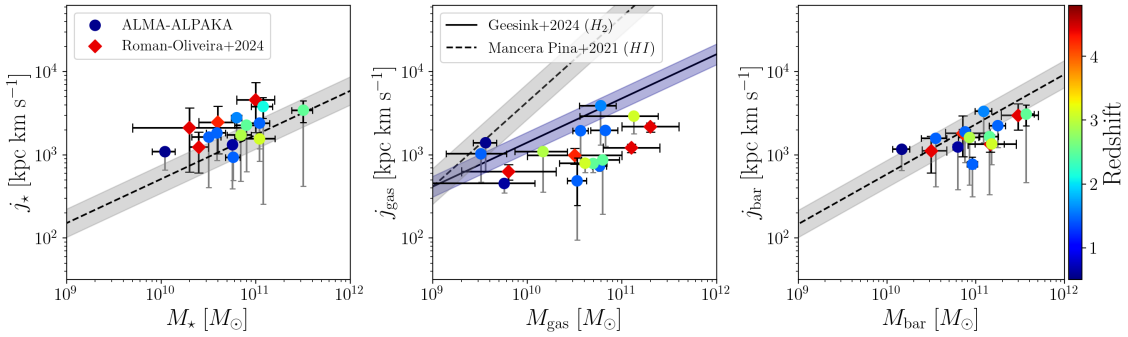

Figure 11: The specific angular momentum - mass relation (from left to right) for the stellar, gas, and baryonic component of the galaxies, with the local relations from Mancera Piña et al. (2021a) shown as dashed lines and their 1σ intrinsic scatter in grey. The local $j_{H_2} - M_{H_2}$ relation is similarly shown in blue (Geesink et al., 2025). For the high redshift galaxies, only the molecular gas is considered for the gas. The baryonic component is assumed to be the sum of the stars and molecular gas. The high redshift galaxies are coloured according to their redshift. For the ALPAKA galaxies, the lower limit in j is given by the grey error bar.

4 Results

In this section we will present the results of our disc evolution models, starting with the parameter fitting in section 4.1. For the best fit parameters we will examine how different properties of the galactic disc behave and evolve in models for three different DM mass bins (section 4.2). Lastly, in section 4.3, we will present the predicted evolution of different scaling relations and compare them to our high redshift data sample and other empirical relations from the literature.

4.1 Constraints on the free parameters of the evolution model

In this section, we present the constraints on the free parameters (i.e. $\log M_{\rm acc}(t_0)$, $\omega_{\rm acc}$ and $\log j_{\rm max}$) of the model described in section 2, for a range of DM halo masses, using the method described in section 2.7. The resulting posterior distributions from the MCMC are shown in appendix C in the form of corner plot, for each DM halo mass (example in fig. 12). Due to the non-gaussianity of some of the distributions, the peak of each distribution is taken. The upper and lower error are determined by taking the shortest interval within which 1σ of the sample around the peak is contained. To better track the general evolution of the galaxies within this range, we also take the median of the sample within the computed upper and lower bounds around the maximum. From the 2D posterior distributions displayed in the corner plots, the degeneracy be-

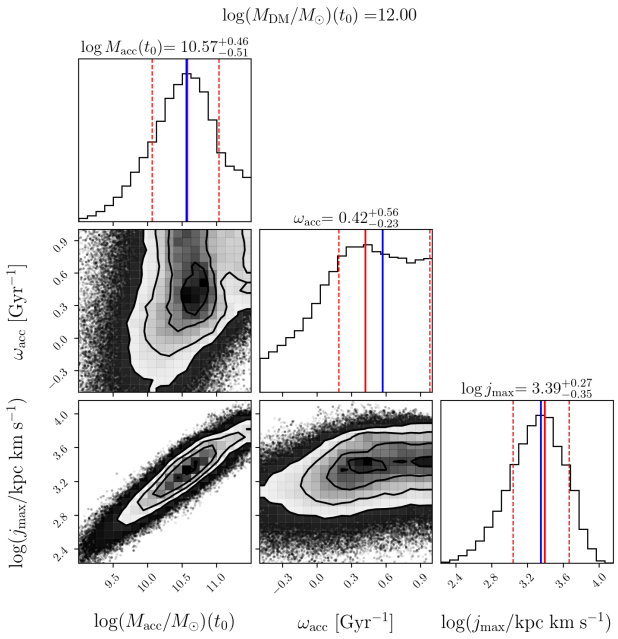

Figure 12: The posterior distributions of the free parameters of the model for $\log(M_{\rm DM}/M_\odot)(t_0) = 12.0$. The red line indicates the maximum of the distribution, with its 1σ uncertainties as the red dashed lines. The blue line is the median of the sample within the uncertainty bounds.

tween the parameters can be analysed too. For all DM halo masses an increase in $\log M_{\rm acc}$ favours larger values of $j_{\rm max}$. The best fit of $\omega_{\rm acc}$ is less affected by a change in the other free parameters. However, $\omega_{\rm acc}$ is in general less constrained, showing a flatter posterior distribution within the bounds of the prior. The posteriors of $\log M_{\rm acc}$ and $j_{\rm max}$, in general, are better defined peaked distributions.

To check if the fitting process was successful we compare how the model reproduces the local scaling relations that were used to constrain the parameters. Figure 13 shows the three scaling relations, with results from the model and its scatter shown as data points, where each data point corresponds to a single DM mass bin. The scatter is the 1σ scatter of the grid sample within the bounds on the best-fit parameters values. For all three relations, we see that the medians and the

scatter within the model reproduce the scaling relations well, indicating that the fitting procedure was successful. Only for the stellar size-mass relation, for the higher masses, the model shows a higher scatter than the local relation of van der Wel et al. (2014).

Figure 14 shows the values of the best-fit parameters as a function of DM halo mass. For every halo mass, we show the values of the three parameters at the peak of their posterior distribution and the corresponding uncertainties with blue circles and the median values with the stars. For the total accreted gas $\log M_{\rm acc}$, the peak and median of the best-fit appear to follow a clear linear increase with an increasing $\log M_{\rm DM}$. The scatter around the peak is consistently between $0.4-0.5$ dex. For accretion frequency $\omega_{\rm acc}$, in general, one can observe that $\omega_{\rm acc}$ increases with increasing $\log M_{\rm DM}$, from $\omega_{\rm acc} \sim -0.5$ Gyr^{-1} to $\omega_{\rm acc} \sim 0.5$ Gyr^{-1}. For $\log(M_{\rm DM}/M_\odot) > 12$, the best-fit estimate appears to plateau around $\omega_{\rm acc} \sim 0.5$ Gyr^{-1}. For $\log(M_{\rm DM}/M_\odot) \leq 11$, the model favours negative $\omega_{\rm acc}$ values, i.e. accretion rates that increase with cosmic time. For $\omega_{\rm acc} \approx -0.5$ Gyr^{-1}, this would indicate the majority of the gas was accreted in the last 2 Gyr, or after $z \sim 0.2$. On the other hand, for $\omega_{\rm acc} \approx 0.5$ Gyr^{-1}, most gas is accreted in the first 2 Gyr of the model, or before $z \sim 2.5$. Compared to the other parameters, $\omega_{\rm acc}$ is less constrained, and has a typical scatter of ~ 0.5 Gyr^{-1}. For the lowest 3 halo masses, the lower bound on the best-fits, reaches the edge of the posterior, and should therefore not be considered the true lower bound on the peak or median value. Lastly, for $\log j_{\rm max}$, similar to $\log M_{\rm acc}$, a linear increase with increasing $\log M_{\rm DM}$ can be observed. The typical scatter around the median is ~ 0.3 dex.

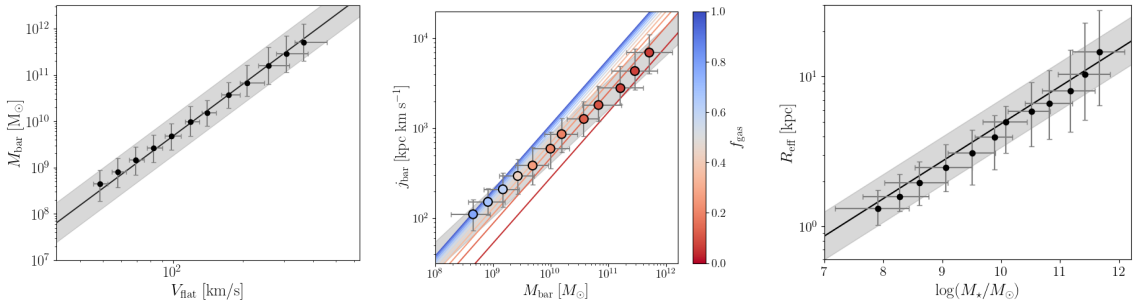

(a) Local baryonic Tully-Fisher relation (Lelli et al., 2019)

(b) Local $j_{\rm bar} - M_{\rm bar} - f_{\rm gas}$ relation (Mancera Piña et al., 2021b)

(c) Local stellar size-mass relation (van der Wel et al., 2014)

Figure 13: The medians and the scatter of the model results at $z = 0$ as the data points, compared to the respective local relation with their intrinsic scatter as the grey band. *middle:* the gas fraction is indicated by the colour, and the $j_{\rm bar} - M_{\rm bar}$ relation (Mancera Piña et al., 2021a) is in grey.

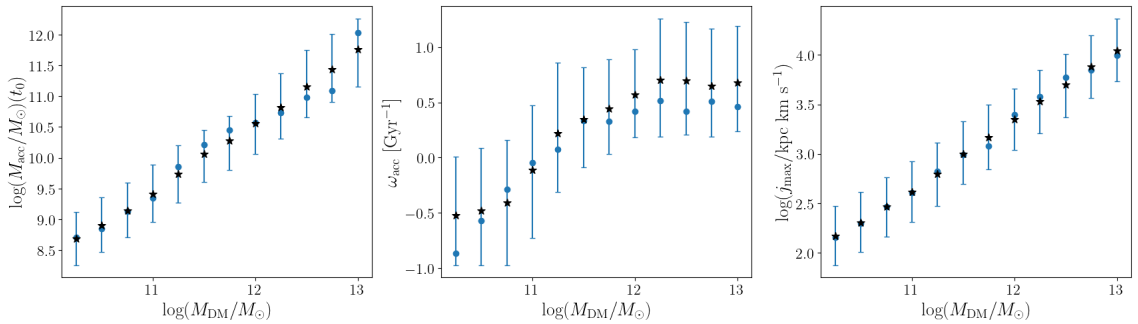

Figure 14: The best fit values of the 3 free parameters of the evolution model against the DM halo mass; *left:* total accreted matter, *middle:* accretion frequency, *right:* maximum specific angular momentum of the accreted gas. In blue, the values corresponding to maximum of the posterior distribution, with error bars representing the 1σ scatter around the peak. The black star indicates the median of the sample within the 1σ bounds.

4.2 Behaviour of the disc properties of modelled galaxies

In this section, we examine how different properties of the galactic disc evolve, including the accretion radius, surface densities, and star formation rate. To illustrate the difference in behaviour for different masses, the corresponding evolution of the properties of the disc, for three representative halo masses $\log(M_{\rm DM}/M_\odot)(t_0) = 11.00, 11.75, 12.50$ are shown. For each halo mass, the best-fit peak values of the free parameters are used.

The specific angular momentum of the accreted gas is set to grow over time, following eq. (33). This induces an inside-out formation of the disc. Here, the power in the relation is set to $n = 0.3$. The red dashed line in fig. 15 shows the evolution of $j_{\rm acc}$. The accretion radius $R_{\rm acc}$, defined as the radial scale length of the exponential distribution of the accreted gas at each time step, is defined by $j_{\rm acc}$ and the rotation velocity $V_{\rm rot}(R)$ at that time, using eq. (34). The black line in fig. 15 shows the resulting evolution of $R_{\rm acc}$. If $V_{\rm rot}(R)$ evolves little, $R_{\rm acc}$ is expected to follow a similar trend as $j_{\rm acc}$. However, the figure shows $R_{\rm acc}$ peaks at early times (< 2 Gyr) for relatively massive galaxies ($\log(M_{\rm DM}/M_\odot) \gtrsim 11.75$), while $j_{\rm acc}$ always increases monotonically, indicating the model needs to accrete gas at higher radii to compensate for a relatively low rotation velocity at these times.

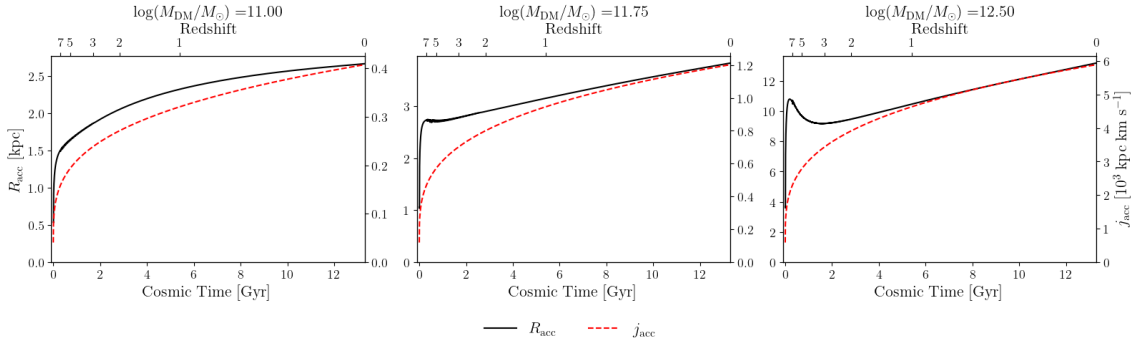

Figure 15: The evolution of the accretion radius $R_{\rm acc}$ and the specific angular momentum of the accreted gas $j_{\rm acc}$, for $\log(M_{\rm DM}/M_\odot)(t_0) = 11.00, 11.75, 12.50$ (from left to right).

In fig. 16, $\Sigma_\star$, $\Sigma_{\rm gas}$, and $\Sigma_{\rm SFR}$ are shown at different redshifts for the discs evolving within our representative DM haloes, corresponding to $\log(M_{\rm DM}/M_\odot)(t_0) = 11.00, 11.75, 12.50$. For all masses, the gas disc is more extended than the stellar disc, in agreement with observations. This is a consequence of the star formation being less efficient at lower gas densities.

For the lowest halo mass, all surface densities increase over time, producing a progressively flatter profile. The latter is a direct consequence of the inside-out formation of the disc. At $z > 1$, the surface densities closely resemble an exponential profile. At lower redshifts, the profiles show a flattening in the inner regions of the disc. For this lowest halo mass, the accretion frequency is negative ($\omega_{\rm acc} = -0.04$ Gyr^{-1}). Hence more gas is accreted at later times and at larger radii, contributing to a relatively smaller increase of the density in the inner regions.

For the intermediate halo mass, the surface densities gradually increase over time, with little change in the steepness of the profiles. However, in the inner regions a decline can be observed. For this halo mass, the best-fit accretion frequency was found to be $\omega_{\rm acc} = 0.33$ Gyr^{-1}. This implies most gas is accreted at early times in the inner regions, feeding the star formation there. However, the consumed gas is not replenished, due to the low accretion rate at later time. Less accretion also induces weaker radial flows, which in turn are also not capable of replenishing the gas in the core. Another contributing factor to the "flattening" in the inner regions, is the chosen star formation law (eq. 41), which allows a higher star formation efficiency at higher gas surface densities. The effect of the break in the star formation law can be seen in the bottom panel of fig. 16, which show a sharp drop-off in $\Sigma_{\rm SFR}$ at larger radii.

Lastly, for the highest halo mass, relatively little change in the surface densities over time

is seen compared to the lower halo masses. The accretion frequency of this galaxy is $\omega_{\rm acc} = 0.42$ Gyr^{-1}. As a consequence, the contributing factors to the evolution of the profiles are similar to that of $M_{\rm DM}/M_\odot)(t_0) = 11.75$, but more extreme due to the gas being accreted at even earlier times. The result is a stronger flattening of the profiles.

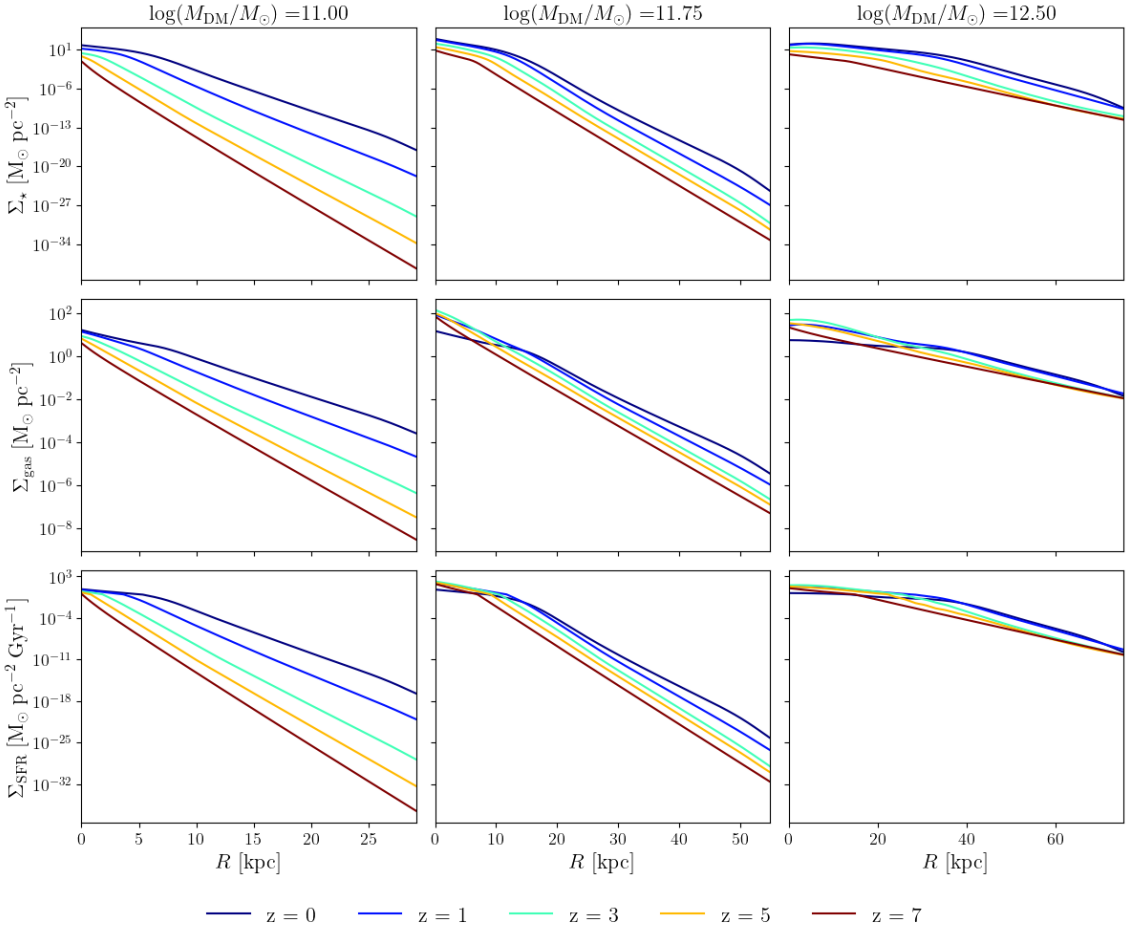

Figure 16: The stellar surface density *(top row)*, gas surface density *(middle row)*, and the star formation rate density *(bottom row)*, at different redshifts as indicated by the colours. The different columns correspond to the evolution of galaxies with $\log(M_{\rm DM}/M_\odot)(t_0) = 11.00, 11.75, 12.50$ (from left to right).

Figure 17 shows the evolution of the total stellar mass, gas mass, and global star formation rate for the same models as above. For the lowest halo mass ($\log(M_{\rm DM}/M_\odot)(t_0) = 11.00$), as mentioned, we found a negative accretion frequency. As a consequence, both the gas and stellar masses increase over time, with an accelerated increase in stellar mass. The evolution for the other halo masses ($\log(M_{\rm DM}/M_\odot)(t_0) = 11.75, 12.50$) show a similar trend to each other. The peak in the gas mass and SFR occurs between $z \sim 2-3$. In the first few Gyr they grow quickly, due the high accretion rate at these times. At later times, when gas is consumed in star formation, and less gas is accreted from the CGM, both gas and SFR drop.

Lastly, we look at the decomposed rotation curves of the previously discussed model galaxies at $z = 0$ (fig. 18). For $\log(M_{\rm DM}/M_\odot)(t_0) = 11.00$, the rotation is dominated by the DM halo contribution at every radius. For the higher halo masses, the stellar disc is more dominant in the inner regions, due to its relatively steep density profile compared to the gas disc. The gas contribution is less significant and peaks at higher radii, due to the gas disc being more extended. In all three cases, the rotation curve becomes flat at higher radii. Additionally, we can look at the rotation curves at $z = 4$ (fig. 19). At this time, the DM is the dominant component, and the

gas component dominates over the stellar component in all cases. All these behaviours are in agreement with observed kinematic properties, although some differences exist, as we discuss in section 5.2.

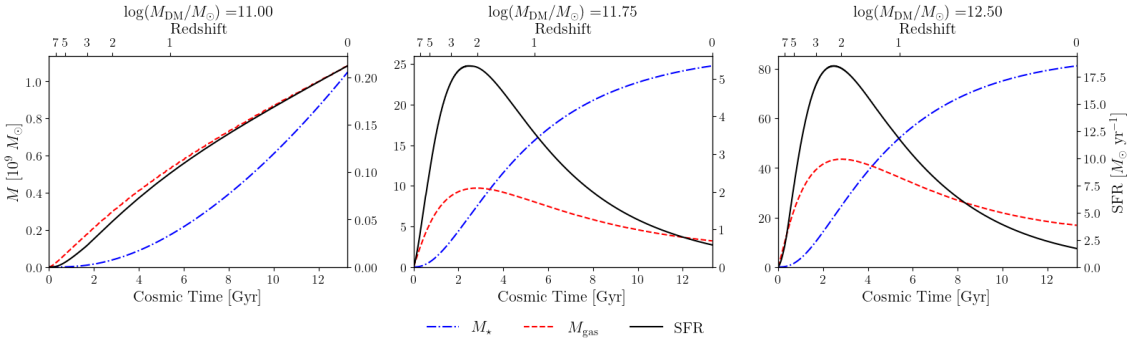

Figure 17: Evolution of the total stellar mass, gas mass and star formation rate in the three models with $\log(M_{\rm DM}/M_\odot)(t_0) = 11.00, 11.75, 12.50$ (from left to right)

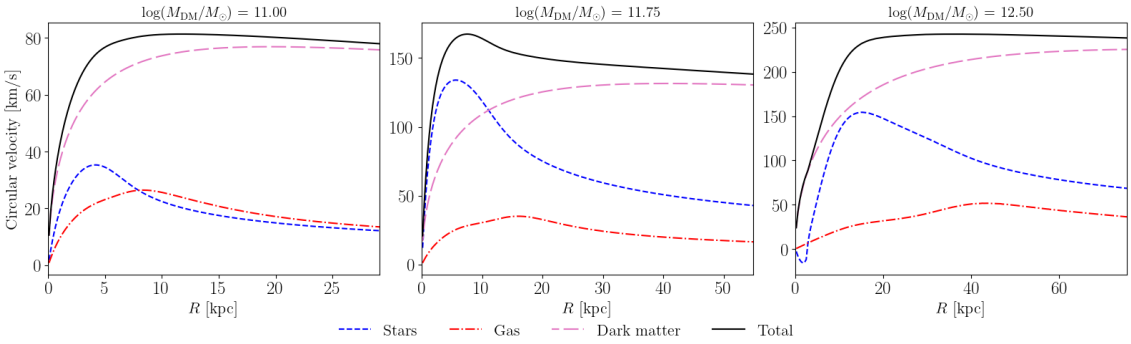

Figure 18: The $z = 0$ decomposed rotation curves, showing the contribution of the stellar disc, gas disc and DM halo, for models with $\log(M_{\rm DM}/M_\odot)(t_0) = 11.00, 11.75, 12.50$ (from left to right)

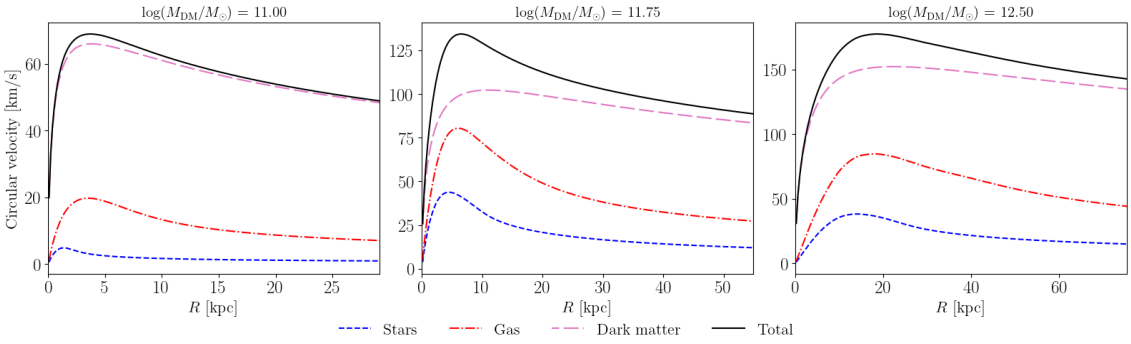

Figure 19: The $z = 4$ decomposed rotation curves, showing the contribution of the stellar disc, gas disc and DM halo, for models with $\log(M_{\rm DM}/M_\odot)(t_0) = 11.00, 11.75, 12.50$ (from left to right)

4.3 Evolution of scaling relations

In this section, we look at the evolution of different scaling relations. Our model evolves galaxies from $z = 10$ to $z = 0$, with radial flows starting at $z = 7$, therefore, we examine the evolution for $z = 7 - 0$. To get an estimate of the general evolution at different masses, the median values of the best-fit parameters are used. We remind that the free parameters were constrained using three local scaling relations, the BTFR, $j_{\rm bar} - M_{\rm bar} - f_{\rm gas}$ relation, and the stellar size-Mass relation. Additionally, the model will be compared to other well known local scaling relations.

Note that due to the negative $\omega_{\rm acc}$ estimates at low $\log M_{\rm DM}$, the disc is formed at later cosmic times. Consequently, not all properties of the galaxies can be defined at high redshifts for these lower halo masses.

4.3.1 Evolution of the Tully-Fisher relations

The first two kinematic scaling relations to be examined are the TFR and the BTFR, for which the results are shown in fig. 20. To get an estimate of the output parameters of the model and their scatter, we take the model results corresponding to the 3D grid parameters within the upper and lower bounds of the best fit estimates of the free parameters. The black data points in the figure represent the medians and the scatter of the properties within these bounds (same as fig. 13). Besides the local BTFR, which was used in the fitting, the local TFR is also well reproduced by the model, showing a similar linear relation and scatter. At the highest halo masses, the model slightly underestimates the stellar masses, for given $V_{\rm flat}$.

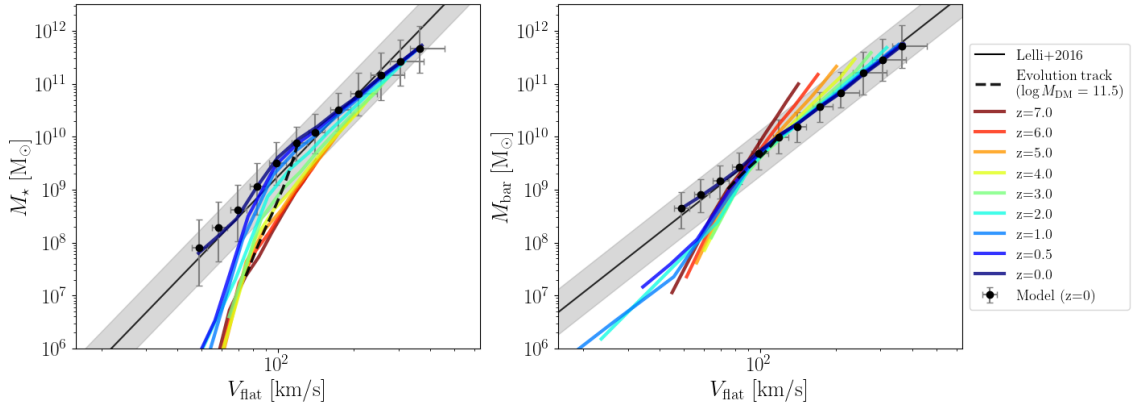

Figure 20: The evolution of the Tully-Fisher relation *(left)* and the baryonic Tully-Fisher relation *(right)* for $z = 7 - 0$, where the different redshifts are indicated by the colours. The local relation and its intrinsic scatter are represented by the black curve and grey band, respectively (Lelli et al., 2016a). The medians and the scatter of the model results at $z = 0$ are presented by the black data points. The black dashed line shows the evolutionary track for a single galaxy, corresponding to $\log(M_{\rm DM}/M_\odot)(z = 0) = 11.5$.

Furthermore, the predicted evolution of these scaling relations can be inspected in fig. 20. For the TFR, at $M_\star > 10^9\ M_\odot$, the relation evolves little. For a given $M_\star$, the relation shifts to slightly higher velocities, but stays within the bounds of the local relation for $z = 7 - 0$. At $M_\star < 10^9\ M_\odot$, there is a sharp turn-off for $z \geq 0.5$, predicting significantly higher velocities compared to the relation at $z = 0$. This indicates that, according to the model, galaxies at these masses obtain most of their stellar mass at late cosmic times. This is directly connected to the negative $\omega_{\rm acc}$ values that were found for the lower DM halo masses.

For the BTFR, a similar but less significant turn-off is seen at $M_{\rm bar} < 10^9\ M_\odot$. Simultaneously, at higher masses, the model predicts higher baryonic masses compared to local relation, at a given $V_{\rm flat}$. In general, this indicates that more massive galaxies obtain most of their mass at early times, letting $M_{\rm bar}$ evolve relatively little with respect to their rotation velocity $V_{\rm flat}$, within the

examined redshift range. In comparison, lower mass galaxies are predicted to obtain most of their mass at later times, showing a more significant growth in $M_{\rm bar}$. These results combined lead to an increase in the steepness of the BTFR with increasing redshift.

Additionally, we can look at the evolution of a single galaxy. Figure 20 shows to evolution track of a galaxy with $\log(M_{\rm DM}/M_\odot) = 11.5$ as a black dashed line. Its stellar mass grows nearly three orders of magnitude between $z = 7$ and $z = 0$, while the baryonic mass grows by 1 order of magnitude. At $z \gtrsim 4$ the galaxy lies below the local TFR, while for the BTFR it remains well within the bounds of the local relation throughout its evolution.

Figure 21 shows the predicted evolution of the model compared to our high-z data sample for the TFR (right) and the BTFR (left). For the TFR, we see that the high-z galaxies are scattered below their respective evolution paths based on redshift, i.e. for a given stellar mass they have higher rotation velocities than predicted by the model. In contrast, the high-z TFR predicted by the model converges to the local relation at these high masses.

For the BTFR we also find that the high-z galaxies lie below the local relation opposed to the model that predicts that at higher redshifts, galaxies lie further above the relation. In other words, at a given stellar mass the model underestimates the rotation velocity compared to the high-z data. We discuss this further in section 5.3.1.

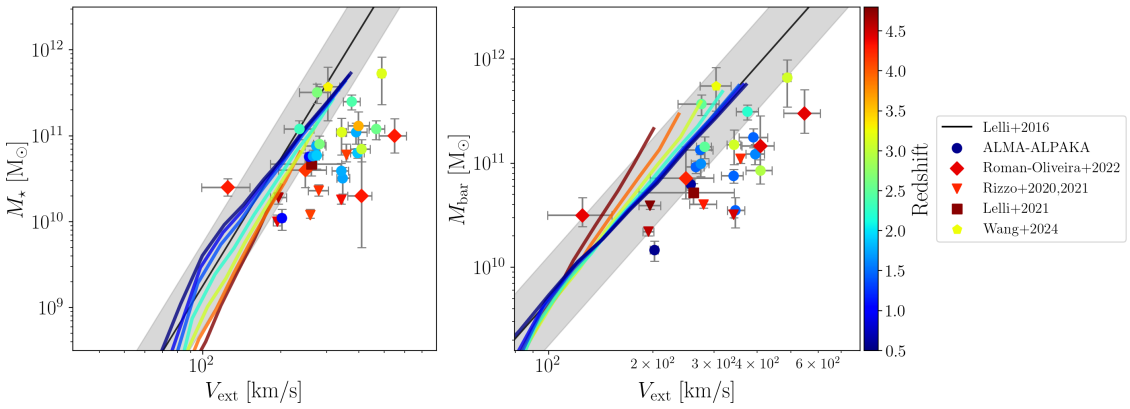

Figure 21: Same as fig. 20, including high-z galaxy data from Chapter 3, with the redshift indicated by the colours

4.3.2 Evolution of the j-M relations

Figure 22 shows the predicted evolution of the $j - M$ relation for the different mass components. Firstly, we can check how well the model reproduces the local $j - M$ relations by Mancera Piña et al. (2021a). The $j_{\rm bar} - M_{\rm bar} - f_{\rm gas}$ relation was used to constrain the parameters, and we see that the model reproduces the local $j_{\rm bar} - M_{\rm bar}$ relation and its scatter well as discussed before. For the stellar and gas component, the model also accurately follows the corresponding local relations. For the stellar component, the medians of the model lie slightly above the relation, but are within the 1σ scatter.

The black dashed lines in fig. 22 indicate the evolution path of a single galaxy. For the stellar and baryonic component, a steady growth in j and M is observed overtime. For the gas component, $j_{\rm gas}$ increases steadily, but $M_{\rm gas}$ declines after a certain time as the gas is consumed by star formation and little gas is accreted.

Overall, the evolution of $j_\star - M_\star$ relation shows little evolution in the slope of the relation and a decrease in the normalisation with cosmic time. This indicates the stellar specific angular momentum evolves relatively little over time compared to the growing stellar mass. For $j_{\rm gas} - M_{\rm gas}$, the relation appears to evolve little from $z = 7$ to $z = 2$, after which for galaxies with $M_{\rm gas} > 10^9\ M_\odot$,

the $M_{\rm gas}$ declines while $j_{\rm gas}$ grows. The result is a steepening of the relation over time. The baryonic relation evolves little compared to those of the other mass components. The evolution of the stellar and gas component show an opposite trend, hence it follows that for their combined evolution in the baryonic component, it cancels out. The little evolution present indicates a slight decline in the normalisation of the relation over time.

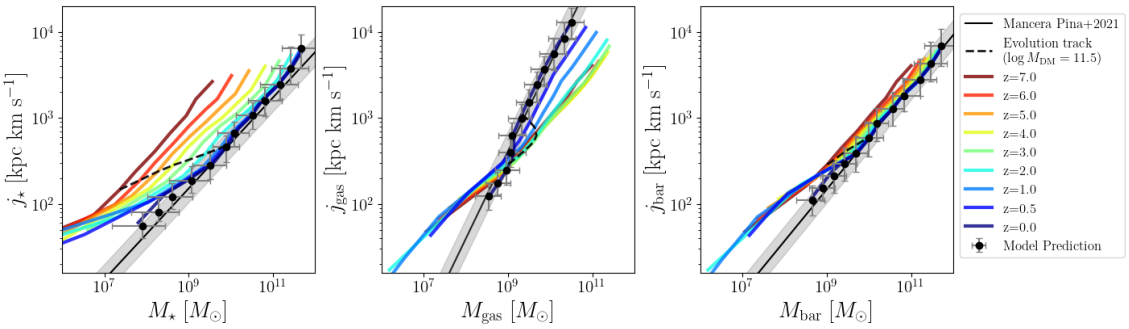

Figure 22: The evolution of the specific angular momentum - mass relation (from left to right) for the stellar, gas, and baryonic component of the galaxies. Similar to fig. 20, with the local relation of Mancera Piña et al. (2021a).

Figure 23 shows the evolution of the $j - M$ relations compared to the high-z data sample for the different mass components. For the $j_\star - M_\star$ relation there is a reasonable agreement between our model and the data, with both being systematically above the local relation. In the $j_{\rm gas} - M_{\rm gas}$ plane the mismatch between the data sample and model prediction is more significant. While both predict that high-z galaxies have a lower $j_{\rm gas}$ at a given $M_{\rm gas}$, the $j_{\rm gas}$ of the observed galaxies is systematically lower than that predicted by the model. For the $j_{\rm bar} - M_{\rm bar}$ relation, both the high-z data and the model show little deviation from the local relation a high redshifts. However, the data have a slightly lower $j_{\rm bar}$ at a given $M_{\rm bar}$ compared to the predictions of the model. The possible causes behind the disagreements between the data and the model are further discussed in section 5.3.1.

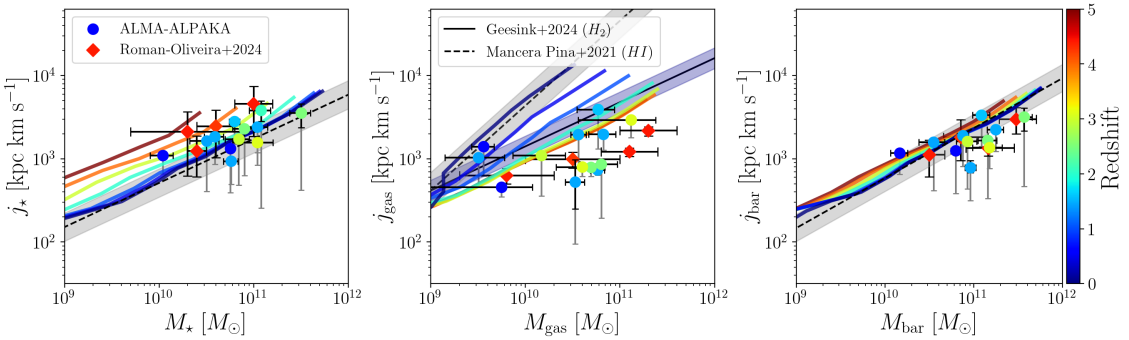

Figure 23: Same as fig. 22, including high-z galaxies, with the redshift indicated by colour. In the middle panel we also shows the local $j_{H_2} - M_{H_2}$ relation with its intrinsic scatter in blue (Geesink et al., 2025)

4.3.3 Evolution of the stellar size-mass relation

Next we look at the evolution of the stellar size-mass relation, presented in fig. 24. This relation was also used to constrain the free parameters, and the model reproduces the general trend and scatter of the local relation well. At high-z, the relation changes most for higher masses, showing that stellar mass increases over time, with relatively little change in the effective radius. When comparing to the observed relations at high-z to the model (right panel fig. 24), it also shows that at fixed stellar mass, we expect a smaller $R_{\rm eff}$. This discrepancy is partially related to the choice of $n = 0.3$, which leads to little evolution in $j_{\rm acc}$ and consequently $r_{\rm acc}$ within the examined redshift range. We will further discuss this discrepancy in section 5.1.

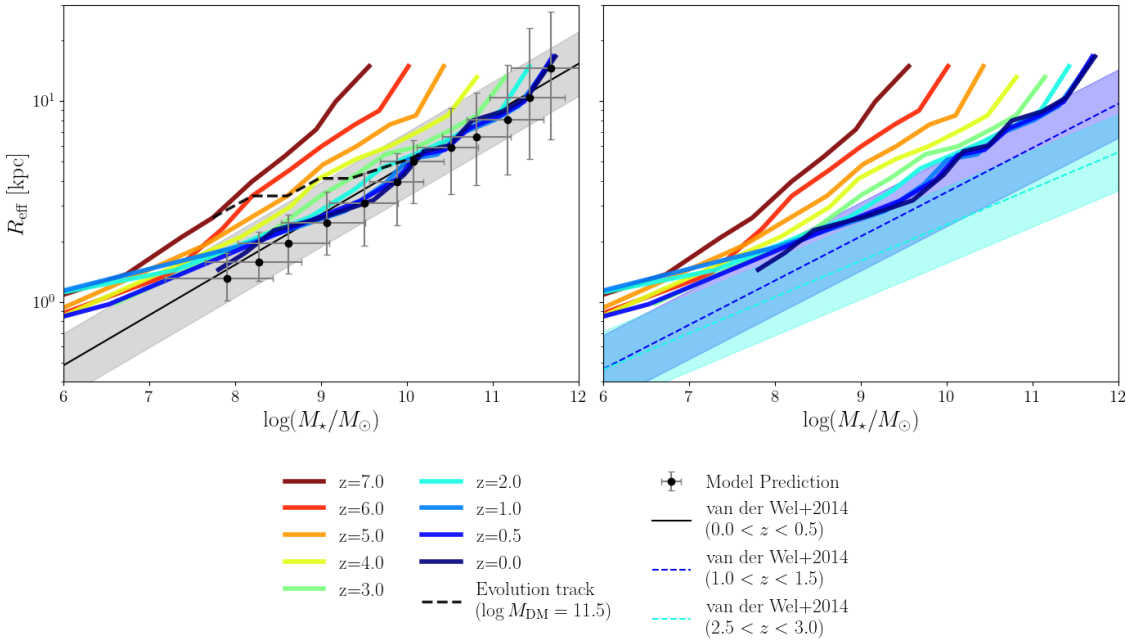

Figure 24: *left:* The evolution of stellar size-mass relation. Similar to fig. 20, with the local relation of van der Wel et al. (2014). *right:* the size-mass relation of the model (full lines) compared to the empirical relations (dashed lines) from van der Wel et al. (2014).

4.3.4 Evolution of the SHMR and SFMS

In addition to the scaling relations that contain parameters that were used in constraining the free parameters of the model, we compare the predictions of the SHMR and SFMS relations of our model to the observed ones at $z = 0$ and higher z.

Figure 25 shows the local relation and the predicted evolution of the SHMR by the model, compared to the relation derived with abundance matching (section 1.2.7). At $z \sim 0$ (middle panel fig. 25) our model overestimates the stellar masses for a given DM halo mass, on the lower and higher halo mass ends, when compared to the lowest z bin of Shuntov et al. (2025) and the local disc galaxies sample from Mancera Piña et al. (2025). Around $\log(M_{\rm DM}/M_\odot) \approx 12$, the model returns the most accurate stellar-to-halo mass ratios. In general the SHMR relation of the model at $z = 0$, more closely resemble a linear relation between $\log M_\star$ and $\log M_{\rm DM}$. This is in line with other determinations, in particular Posti et al. (2019).

The evolution of the SHMR shows a decline in steepness of the relation with decreasing z for $\log(M_\star/M_\odot) > 9$. This indicates that with increasing DM mass, $\log M_{\rm DM}$ shows a bigger growth relative to the growth in $\log M_\star$. For $\log(M_\star/M_\odot) < 9$, a steep drop-off can be observed as a consequence of of the fact that models with lower $M_{\rm DM}$ obtain the majority of their baryonic mass at progressively later times.

The evolution predicted by the model can be compared to the empirical SHMRs of Shuntov et al. (2025) (fig. 25 right panel), where we specifically show the SHMR at $z \approx 2, 4, 6$ for both. The relations from Shuntov et al. (2025) were established using a SMF based on JWST observations from the COSMOS-Web survey, and the HMF from Watson et al. (2013). The qualitative trend in both is similar, showing that at a certain $\log M_{\rm DM}$, $\log M_\star$ is greater at higher redshifts. However, the SHMR's of our model at these redshifts are systematically shifted towards lower $\log M_{\rm DM}$ by ~ 0.5 dex compared to the SHMR's of Shuntov et al. (2025).

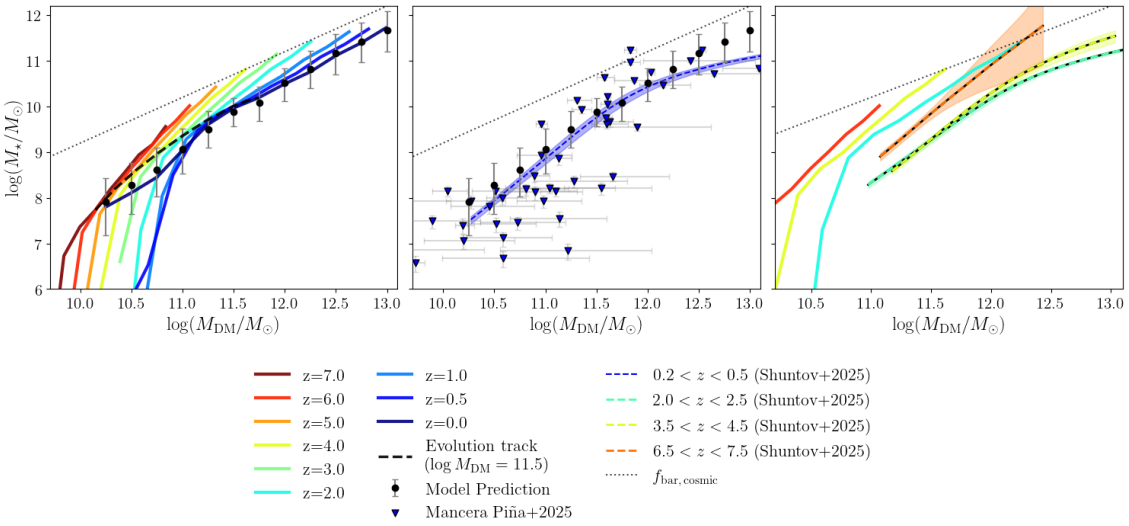

Figure 25: *left:* Evolution of the SHMR in our model, similar fig. 20. *middle:* The data points indicate the median and scatter of the model's results at $z = 0$. The dashed blue line is the empirical SHMR from Shuntov et al. (2025) at their lowest z bin, with its intrinsic scatter indicated by the blue band. The blue triangles are local disc galaxies from (Mancera Piña et al., 2025). *right:* The full lines are the result of the model at $z = 2, 4, 6$. The dashed lines are the results from Shuntov et al. (2025) at similar redshifts. The dotted line in every panel indicates the cosmic baryon fraction.

Figure 26 shows the predicted evolution of the star formation main sequence. To check how well the model reproduces the local relation, we compare to the relation by Whitaker et al. (2012) based on a sample with redshifts $0 < z < 0.5$. Our model closely resembles this relation at $z = 0.5$. At $z = 0$, the model underestimates the SFR for $\log(M_\star/M_\odot) \gtrsim 9.5$, slightly overestimates it at lower masses. In general the main sequence follows a linear relation for $z \geq 0.5$, for which the SFR at a given mass declines over time. When examining the change in the SFR over the evolution of a single galaxy (dashed black line in fig. 26 left panel), we see that for the evolution track plotted for $\log(M_{\rm DM}/M_\odot)(z = 0) = 11.5$, the SFR increases at high z, peaks around $z = 2$, and then declines. In general, the SFR in the model evolves more rapidly at $z < 4$.

In fig. 26 (right panel), the SFMS of the model is compared to the observed determination of Popesso et al. (2023) at $z = 0, 2, 4, 6$. Both show the same qualitative trend with higher SFRs at higher redshifts for a given stellar mass. However, where all model shows a nearly linear relation between $\log \mathrm{SFR}$ and $\log M_\star$ at all redshifts, the relations from Popesso et al. (2023) show turn-off in the SFMS slope for $\log(M_\star/M_\odot) \geq 10.5$. Consequently, the model slightly overestimates the SFR at these high masses. However note that at high-z, the relations from Popesso et al. (2023) contain galaxies that cannot be in our model because they may have quenched before $z = 0$. At lower masses, the model tends to underestimate the SFR, particularly around $z \sim 2$.

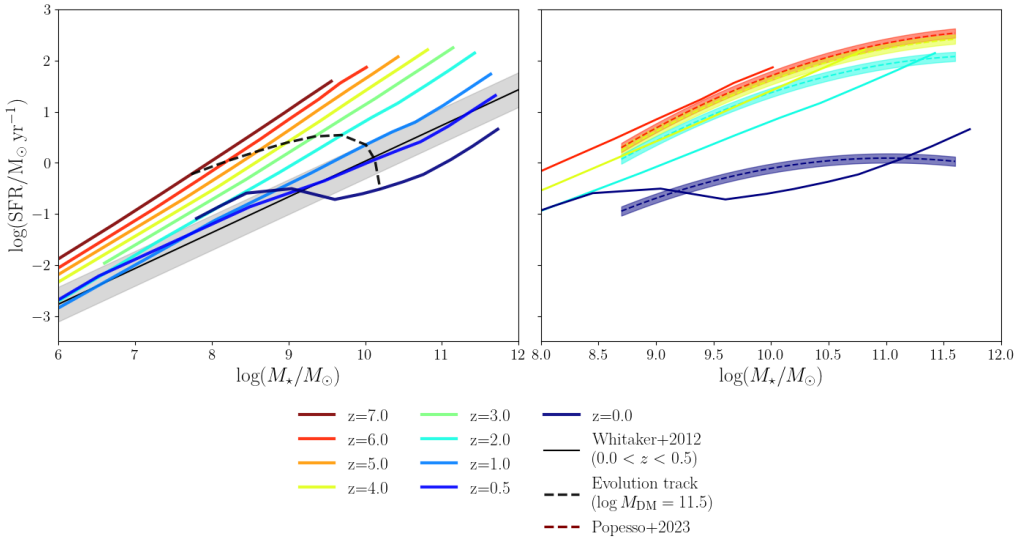

Figure 26: *left:* The evolution of the star formation main sequence. Similar to fig. 20, with the observed local relation of Whitaker et al. (2012). *right:* The SFMS of the model (full lines), compared to the empirical relations (dashed lines) of Popesso et al. (2023).

4.4 Impact of different n and j mismatch on best-fit parameters

All the results shown so far were for $n = 0.3$ and no angular momentum mismatch between the accreted gas and the disc ($\alpha = 0$). Here we test the model for $n = 0.5, 1.0$ (section 2.2.2), and for $\alpha = 0.1, 0.2$, i.e. $j_{\rm acc}(t, R)$ will be $(1 - \alpha)j_{\rm disc}$ (section 2.3). A greater mismatch causes stronger inward radial flows for the gas in disc. The best-fit parameters for these variations are computed for $\log(M_{\rm DM}/M_\odot) = 11.0, 11.75, 12.5$. The resulting corner plots are presented in appendix C.2.

Figure 27 shows the best-fit parameter values for the 3 free parameters of the model for the different combination of n and α. In general we see that the new best-fit values are within the 1σ uncertainty of the original results ($n = 0.3,\ \alpha = 0$), indicated by the black data points in the figure. For the total accreted matter ($\log M_{\rm acc}(t_0)$, left panel fig. 27), different values for n and α have little impact on the best-fit values. For the accretion frequency ($\omega_{\rm acc}$, middle panel fig. 27), we see a decline in the lowest DM mass bin for greater values n. The negative values of $\omega_{\rm acc}$ indicate that the accretion rate increase exponentially over time, with more gas being accreted at later times for greater negative values. For the maximum accreted angular momentum ($j_{\rm max}$, right panel fig. 27), the best-fit values for the $n = 1$ results are greater by ~ 0.5 dex relative to the original results. For the other values of n and α the difference in $j_{\rm max}$ are negligible. From the on average small change in the best-fit parameters, we conclude that subsequent difference in the evolution of the galaxy's properties in the model is also small. However, this is not a full explanation, and based on different constraints or other changes in the model, a change in these parameters could have a larger impact on the results. It is therefore important to include n and α as free parameters in the future.

4.5 Evolution of scaling relations for no DM evolution

In this section, we look at the results of the model with no growth of the DM halo. This implies that the total DM mass and its contribution to the rotation velocity remain constant. This version should also more closely resemble that of Costa (2024), where the DM halo was not considered and the rotation curve was assumed to be constant in time. Similar to the test for different values of n and α, we computed the best-fit parameters for $\log(M_{\rm DM}/M_\odot) = 11.0, 11.75, 12.5$. Similar to the original results we took $n = 0.3$, and assumed no mismatch ($\alpha = 0.0$). The best-fit values for

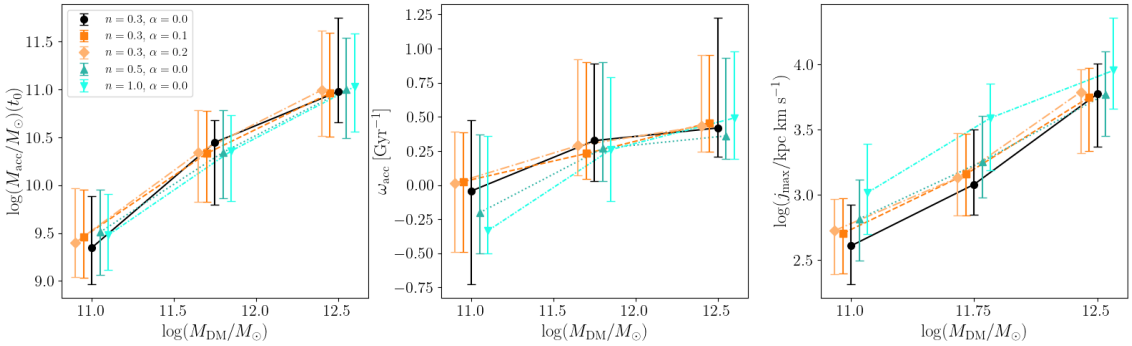

Figure 27: The best fit values of the 3 free parameters of the evolution model against 3 DM halo masses, for different combinations of n and α (see legend). *left:* total accreted matter, *middle:* accretion frequency, *bottom:* maximum specific angular momentum of the accreted gas. The values of the best fit parameters are indicated by the maximum of the posterior distribution and the 16th and 84th percentile of the sample around the maximum indicated by the errorbars. The positions of the points along the x-axis have been slightly shifted around the reference masses ($\log(M_{\rm DM}/M_\odot) = 11.0, 11.75, 12.5$) for clarity.

$M_{\rm acc}(t_0)$, $\omega_{\rm acc}$ and $j_{\rm max}$ do not differ significantly from the previously presented results and are well within their 1σ uncertainty bounds.

In fig. 28, the predicted evolution of the TFR and BTFR are shown, based on the evolution of galaxies with $\log(M_{\rm DM}/M_\odot) = 11.0, 11.75, 12.5$. The evolutionary track for a galaxy with $\log(M_{\rm DM}/M_\odot) = 11.75$ is also included in the figure as the dashed black line. In general, we see little evolution of $V_{\rm flat}$, while the stellar and baryonic masses grow over time. This is expected as $M_{\rm DM}$ is the dominant component in the rotation curve at large radii, hence when $M_{\rm DM}$ does not evolve, $V_{\rm flat}$ will also grow little over time. The result is that the relations at higher redshifts, lie further below the local relations. This is in stark contrast with the original results (fig. 20), where we observed an evolution of $V_{\rm flat}$, leading to the prediction that more massive high-z galaxies lie on the local TFR and slightly above the local BTFR. The $M_\star$ and $M_{\rm bar}$ mass range covered in these new results have little overlap with the mass range of the high-z data, however, the qualitative evolution trend of the model is in better agreement with the high-z data.

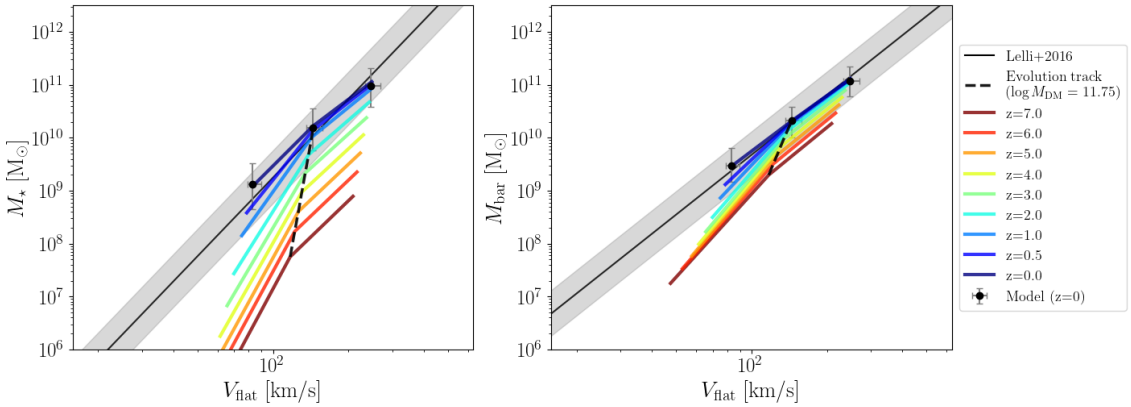

Figure 28: The evolution of the Tully-Fisher relation *(left)* and the baryonic Tully-Fisher relation *(right)*, same as fig. 20, but for a model with no evolution of the DM halo.

Figure 29 shows the predicted evolution of the $j - M$ relations of the stellar, gas, and baryonic component for this model with no DM halo growth. The qualitative evolution trend is similar to the original results (fig. 22). The evolution of the specific angular momentum is tightly linked to

the prescribed evolution of $j_{\rm acc}$, which was not changed. Similarly, the evolution of the individual mass components is tightly linked to the free parameters $M_{\rm acc}(t_0)$ and $\omega_{\rm acc}$, which have not changed significantly.

The evolution of the size-Mass relation for a model with no DM evolution (see fig. 30), also shows a similar qualitative trend compared to the original results. The effective radius does show a larger growth within the examined redshift range, compared to the nearly constant evolution at high masses in the original results. This appears an improvement when compared to the empirical relations. Similar to the $j - M$ relations, this relation is more influenced by the free parameters of the model than by the value of $M_{\rm DM}$, given that the parameter values difference is small.

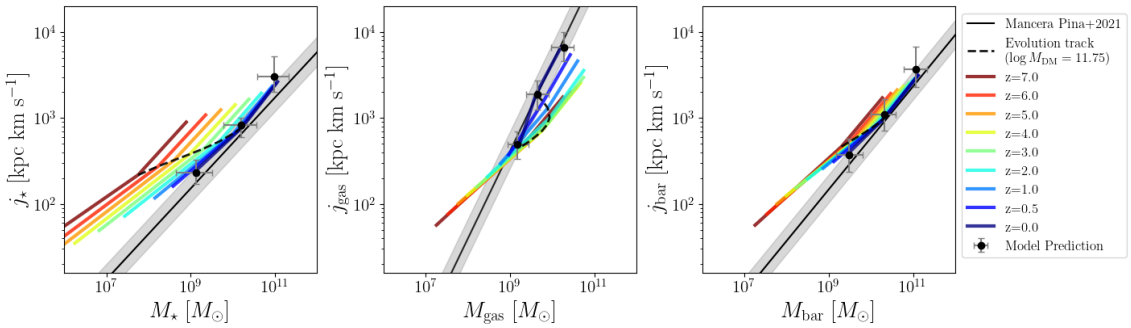

Figure 29: The evolution of the specific angular momentum - mass relation (from left to right) for the stellar, gas, and baryonic component of the galaxies, same as fig. 22, but for a model with no evolution of the DM halo.

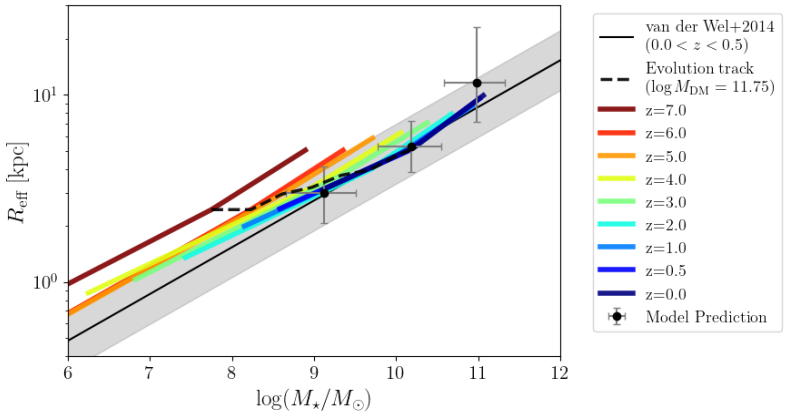

Figure 30: The evolution of stellar size-mass relation. Same as fig. 24, but for a model with no evolution of the DM halo.

5 Discussion

In this section we will first discuss how the main assumptions in our model impact the derived parameters and we discuss potential improvements (section 5.1). After that we will examine how our high redshift data sample compares to the predicted evolution of the scaling relations. We then compare the scaling relations from our model with the ones reported in the literature and analyse discrepancies (section 5.3). Lastly, in section 5.5, other possible additions and improvements to the model will be discussed.

5.1 Impact of assumptions in the evolution model

5.1.1 Absence of feedback

In our model, outflows are completely neglected for all galaxy masses ($\dot{\Sigma}_{\rm out} = 0$, eqs. (15) and (16)), under the reasoning that massive galaxies retain most of their gas due to their high escape velocities. However, this simplification may have several implications for the results of the model. In particular, it can lead to an overestimation of the stellar and baryonic mass, especially for low-mass galaxies, in which stellar and supernova-driven feedback can expel a significant amount of gas from the galactic disc (Muratov et al., 2015; Christensen et al., 2016). Hence, ignoring outflows, leads to an overprediction of gas retention and consequently of the star formation efficiency. In the model, star formation is increased in regimes where feedback would self-regulate or quench the star formation. To compensate for this, in low-mass galaxies, the results of the parameter fitting are that the model accretes gas mostly at later times, which is discussed in more detail later. It is however interesting that we can mostly reproduce the shape of the SHMR at $z = 0$ without ejective feedback.

Additionally, feedback can impact the distribution of the angular momentum in the disc (El-Badry et al., 2018). For instance, the ejected gas from stellar feedback often comes from central, low angular momentum regions of the galaxy. If a fraction of the ejected gas is later re-accreted (e.g. through galactic fountains), this gas is expected to have a higher angular momentum than at the time of ejection due to factors like mixing with the CGM and torque by the DM halo. As a consequence, it will also be accreted at larger radii, where the angular momentum of the disc is greater. In general, feedback with or without re-accretion leads to a higher average angular momentum of the baryonic component and more extended discs, compared to results from smooth gas accretion alone.

Currently, any mismatch between the observed properties and the model predictions must be compensated entirely by adjusting the accretion history, i.e. tuning $\omega_{\rm acc}$. To obtain galaxies with realistic gas fractions and sizes, the model predicts negative values for $\omega_{\rm acc}$ for low-mass galaxies, meaning most gas is accreted at later times. Including feedback would improve regulation of the SFR by reducing the amount of gas that is available for star formation and reduce the SFR. A lower overall SFR could allow gas to be accreted earlier, resulting in more realistic predictions for $\omega_{\rm acc}$ for low-mass galaxies. Additionally, inclusion of feedback could help break the degeneracy between the total accreted mass $M_{\rm acc}(t_0)$ and the accretion history ($\omega_{\rm acc}$). In the future we could implement feedback using a simple parametrized outflow model, e.g. by introducing a mass-loading factor which could be related to the SFR or halo mass (e.g. Muratov et al., 2015).

5.1.2 Accretion: history and radial distribution

The current assumption for the accretion history is an exponentially declining or increasing accretion rate (eq. 29). While this is a common simplification, it is not a generic outcome of cosmological growth with the gas accretion being connected to several other important processes. In the current model a high value of $\omega_{\rm acc}$ concentrates accretion and star formation at early times. A smaller positive $\omega_{\rm acc}$ would create more extended discs and a slower stellar mass growth. Additionally, it may lead to better SFHs, compared to the current SFHs (fig. 17), in which strong quenching occurs for higher masses at $z > 2$.

There are several key processes that impact the accretion history. Firstly the gas accretion is linked to the growth of the halo. The potential of the halo is connected to the virial temperature and the ability of the gas to cool, the shock stability of inflows (hot vs. cold mode), and the gravitational force needed to retain gas. Secondly, the baryon accretion itself is therefore regulated by cooling, feedback, and virial shocks. Cold-mode accretion is expected to dominate in low-mass haloes (Kereš et al., 2005), with a relatively steady inflow. Hot-mode accretion is more more dominant in more massive haloes, creating a more delayed and non-monotonic accretion history (Dekel & Birnboim, 2006; Nelson et al., 2015). Implementing prescriptions that would mimic hot-mode accretion could allow for smaller a $\omega_{\rm acc}$ (i.e. longer accretion timescales) for massive galaxies, instead of the current best-fit $\omega_{\rm acc}$ that forces all gas to be accreted in the first 2 Gyr of the evolution in the model.

As the exponential form only has one parameter controlling its shape ($\omega_{\rm acc}$), it controls both the steepness at early times and the suppression of the accretion at later times. As galaxies in reality can have delayed accretion peaks or sustained late-time accretion (Behroozi et al., 2013), the model is likely to overestimate $\omega_{\rm acc}$ in high-mass systems to suppress late-time growth, and underestimate $\omega_{\rm acc}$ in low-mass systems to sustain growth on longer timescales.

The gas itself is always accreted in an exponential surface density profile, with a scale radius increasing over time according to $R_{\rm acc}(t) \sim j_{\rm acc}(t)/V_{\rm rot}$. Because the accreted gas is distributed with most of its mass near the centre, the resulting disc grows, concentrating baryonic mass at small radii. This keeps the average $j_{\rm bar}$ relatively low. The model compensates for this with very large $R_{\rm acc}$ at early times (fig. 15) Introducing a more extended or outer-peaked profile (e.g. a gamma function) would help contribute to more extended discs, without needing $\omega_{\rm acc}$ or n to compensate for this. E.g. the power in the growth of $j_{\rm acc}$ was now set $n = 0.3$ to force a steep increase in j at early times by accreting at larger radii. For a profile that is not centrally peaked, the gas can be accreted at larger radii for the same angular momentum. Furthermore, it would lead to lower central surface densities and slower star formation, allowing for a higher gas fraction at late times, contributing to more realistic estimates of $\omega_{\rm acc}$, particularly for low-mass galaxies.

5.1.3 Angular momentum of accreted gas

As discussed in the previous section, $j_{\rm acc}(t)$ is closely related to the accretion history and the growth of the disc size. Here we will specifically discuss the assumed evolution of $j_{\rm acc}(t)$ (eq. 33) and its corresponding parameters. The main assumptions in the current parametrization of $j_{\rm acc}(t)$ is the choice of $j_{\rm min} = j_{\rm max}/10$ and $n = 0.3$. The choice for these parameters impact the evolution of several galactic properties. Firstly the size evolution, if early accreted gas has a lower angular momentum, the mass will be more centrally concentrated. Hence a lower $j_{\rm min}$ compresses early discs. Additionally, this leads to higher central densities and SFR, and increased rotation velocities. For example, in section 4.4, we saw that for $n = 1$, the model compensates for this by predicting a greater negative $\omega_{\rm acc}$ at the low halo mass, and in general predicts greater values for $j_{\rm max}$, compared to the results of $n = 0.3$. This is because, for $t < t_0$, $j_{\rm acc}$ is lower for $n = 1$ than when $n = 0.3$, assuming the same $j_{\rm min}$ and $j_{\rm max}$. To offset this reduction and still match the required angular momentum budget of the disc, the model compensates by adopting higher values of $j_{\rm max}$. The evolution of $j_{\rm acc}$ also has an impact on the evolution of the specific angular momentum of the different mass components of the discs. These assumptions also have a direct impact on the best-fit estimates of $j_{\rm max}$ and $\omega_{\rm acc}$. If $j_{\rm max}/j_{\rm min}$ is set too high, this could lead to unrealistically high values of $j_{\rm max}$ and negative values for $\omega_{\rm acc}$ to recover the local size-mass relation. Additionally, we note that introducing an angular momentum mismatch α of 10% or 20% between the accreted gas and the disc has a negligible impact on the results within the current model. However, if the model is adapted based on the assumptions discussed here, α and n could have more significant impact on the results and should be considered as free parameters in the future.

As an improvement to the model, $j_{\rm min}$ could be made a free parameter or be allowed to vary with the halo spin parameter or environment. Alternatively, the growth of the accreted angular

momentum could be directly related to the DM halo, e.g. by letting $j_{\rm acc}(t)$ scale with the evolution of the halo's specific angular momentum (Bullock et al., 2001b).

5.1.4 Absence of mergers

Another simplification of our model is the absence of both minor and major mergers. The model assumes a smooth continuous gas accretion, with no perturbations to the disc. A general consequence of this is an overly smooth evolution of the galaxy's properties and a reduction in the evolutionary scatter. Major mergers could temporarily destroy the disc or permanently change the morphology of a galaxy. Within the framework of our model, a galaxy will always remain a stable disc. In general the majority of SFGs are believed to have obtained most of their mass through the smooth accretion of cold gas (Speagle et al., 2014). However, for the massive galaxies ($\log(M_\star/M_\odot) \gtrsim 11.0$), minor mergers can contribute significantly to the build-up of mass (Rodriguez-Gomez et al., 2016). Especially at lower redshift ($z \lesssim 2.0$) mergers become more important relative to the declining cold gas accretion rate. For these massive galaxies, star formation is expected to quench at relatively early times, with dry mergers dominating the growth in stellar mass and potentially contributing to the formation of a bulge (Oser et al., 2010; Tacchella et al., 2016). This is consistent with the results of our model, in which we found that for these masses the majority of the gas is accreted at $z \gtrsim 2.5$. Additionally, the lack of bulge formation due to the absence of mergers could help explain the shallow surface density profiles in the inner regions of massive galaxies in the model.

5.1.5 Instantaneous recycling approximation

The IRA treats all stellar mass loss from SNe and stellar winds as instantaneous, as we assume a fixed fraction $\mathcal{R} = 0.3$ of the SFR is returned to the ISM at each time step. However in reality, roughly half of the gas recycling that is due to stellar winds occurs on Gyr timescales. The IRA leads to an overestimation of the gas return at early times, artificially sustaining star formation, while simultaneously causing an underestimation of the gas fraction at later times. By removing the time-delay between star formation and feedback, the SFH flattens, leading to lower $\omega_{\rm acc}$ to compensate for the higher internal gas recycling. If the IRA was removed, likely more gas is returned at later times, requiring less accretion. The model could be improved by applying delayed recycling where the gas return is computed using IMF-weighted stellar lifetimes (eq. 42), allowing the gas return from different stellar populations to be spread over Gyr timescales.

5.2 Evolution of surface densities

In this section, we will discuss if the observed behaviour of the disc properties matches expectations, based on the results presented in section 4.2. Firstly in fig. 15 we observed that the evolutionary trend of $R_{\rm acc}$ does not follow the same trend as $j_{\rm acc}$ as $R_{\rm acc}$ peaks at early times. As the angular momentum is determined by the distribution of mass and the rotation velocity, this is likely an indication of a too low rotation velocity at early times, that the increase in $R_{\rm acc}$ is compensating for. At these times, the rotation velocity is dominated by the dark matter component (fig. 19), and therefore suggests that the DM halo is not growing fast enough at early times. For the DM accretion rate we currently use the formalism by Krumholz et al. (2018), for future work a different prescription should be used, e.g. the semi-analytical merger tree of van den Bosch et al. (2014). Our results for a model with constant DM gave a more accurate evolution of the TFR and size-mass relation in particular (section 4.5), a faster growth of the DM halo at early times is likely to have a similar effect.

Related to the rotation curve decomposition, we also observed an issue with the rotation of the stellar component for the higher DM mass in fig. 18. In the inner 3 kpc, the rotation velocity is negative (not real), as a result of a small decline in the stellar surface density towards the centre at $z = 0$ (fig. 16). This is related to the larger issue of the flattening of the surface densities in

the inner regions for the higher mass galaxies in the model. While based on observations, more massive SFGs are commonly found to have a bulge (e.g. Förster Schreiber & Wuyts, 2020). As discussed in section 5.1.4, the absence of mergers in our model could be a contributor to this discrepancy. Additionally, an absence of strong inward radial flows contribute to the relatively shallow density profiles in the central regions.

5.3 Comparison evolution model & literature

In section 4.3, the predicted evolution of several scaling relations was compared to our high-redshift data sample and to evolutionary trends reported in the literature. In this section, we examine any discrepancies and discuss how they may relate to the assumptions and limitations of our evolution model.

5.3.1 Comparison to high redshift data

When comparing the predicted evolution of scaling relations to our high redshift data sample, a mixed level of agreement was found (figs. 21 and 23). All galaxies in our sample are massive star forming discs ($\log(M_{\rm bar}/M_{\odot}) \gtrsim 10.5$), and their positions relative the local and evolved scaling relations reflect both the model limitations and observational biases which are further discussed in this section.

At fixed stellar mass, the high redshift galaxies show much scatter with redshift but tend to lie below the local TFR, i.e. they have higher rotation velocities than local galaxies of the same stellar mass. In contrast our model predicts little to no evolution of the TFR at these high stellar masses. This is directly related to the high $\omega_{\rm acc}$ that was found at these masses, meaning that gas is accreted at very early times with little evolution later. As discussed in section 5.1, this overestimation of $\omega_{\rm acc}$ is likely related to the assumption made for $j_{\rm acc}(t)$ and the absence of feedback. Cosmological simulations also predict a relatively little evolution at high stellar masses (Lovell et al., 2018; Pillepich et al., 2019), and find that massive discs reach equilibrium earlier and evolve more slowly. The fact that the high-z galaxies lie below the predicted relation at high-z, could also be partially attributed to an underestimation of the halo mass at these times. A faster growth of the halo mass at early times would result in a larger $V_{\rm flat}$ at high redshifts, bringing the model closer to the data.

For the BTFR, we also found that the high-z galaxies lie slightly below the local relation, while the model predicts that they should lie above it. One contribution to this discrepancy could be the incomplete measurement of the total gas mass in the data. Cold molecular gas accounts for a fraction of the total gas, while the atomic gas is omitted. HI is difficult to detect at $z \gtrsim 1$, with much debate on its evolution even at these redshifts (Bera et al., 2023; Chowdhury et al., 2023; Zhang et al., 2021). However the atomic gas can be dynamically dominant in the outer disc and therefore have a non-negligible contribution to the mass and angular momentum of the gas and baryonic component (Lagos et al., 2014; Popping et al., 2014).

The predicted evolution in $j_{\star} - M_{\star}$ relation (fig. 23) aligns reasonably well with the observations, considering both the relatively large scatter in the evolution model (not shown in the figure) and the scatter in the data. The predicted evolution indicates that while the galaxies gradually build up their stellar mass, $j_{\star}$ evolves relatively little. For these massive galaxies most stars are formed early, and since the stellar radial flows are relatively small, and with IRA, the absence of mergers and no feedback, $j_{\star}$ is not further disrupted. The high angular momentum of the gas that is accreted later has little impact on the stellar component due to the low amount of gas being accreted at these times, and the low gas densities in the outer regions allow for little star formation (due to use of a star formation law with a low density cut-off, eq. (41)).

For the $j_{\rm gas} - M_{\rm gas}$ (fig. 23) relation we observe a bigger mismatch between the predicted evolution and the high-z observations. This is likely connected to a systematic underestimation of the gas angular momentum in the data, due to the missing HI component discussed previously.

Observations only trace the centrally concentrated molecular gas. The HI gas is expected to be more extended (Krogager et al., 2024), meaning even if it contributes little to the total gas mass at these redshift, it could have a large impact in the angular momentum of the gas. Furthermore, the model predicts little evolution in the relation until $z \sim 2$, after which it turns to the local relation as the gas mass declines due to consumption by star formation and little replenishment by gas accretion, while in general $j_{\rm gas}$ still grows. If the evolution of the molecular gas component shows a similar trend as the total gas component, i.e. a continuing growth in j with a nearly constant or decreasing gas mass at low-z, this could help explain why the high-z galaxies in our sample lie below the local $j_{\rm H_2} - M_{\rm H_2}$ relation.

The $j_{\rm bar} - M_{\rm bar}$ relation (fig. 23) shows very little evolution, which is in good agreement with the high-z sample. The data is scattered slightly below the local relation and the predicted evolution, however this is possibly related to the systematic underestimation of $j_{\rm gas}$ as discussed previously.

Aside from the already mentioned discrepancies in the data, the bias and diversity of the sample also needs to be considered. All observed galaxies are luminous, massive, well-ordered discs with high SFRs, and, for some, AGN activity. Additionally, they come from a range of environments, with the majority being in overdense regions. Most importantly they are not guaranteed to be direct progenitors of local disc galaxies. This selection bias makes it difficult to make a generalized comparison to the evolution predicted by the model. Moreover, the diversity in the data introduces significant scatter, making it difficult to isolate any evolutionary trends in this small sample.

For future comparisons a more homogeneous data sample is required, with new observation from ALMA. Additionally, the accuracy in the current sample can be improved with JWST observations, to replace the stellar surface brightness profiles from HST observations that were used to compute $j_\star$ and $j_{\rm bar}$ of the galaxies in the ALPAKA sample. An improved data sample would allow for the high-z data to be included in constraining the free parameters of the model. This would help remove degeneracies between the parameters and provide a more accurate description for the evolution of the scaling relations.

5.3.2 Tully-Fisher and j-M relations

Aside from comparing the scaling relations to our high-z data sample, here we compare the evolution of the scaling relations predicted by our model with previous observational studies, and to the results of other (semi-)analytic models. Any observational studies are mostly limited to redshifts below $z \sim 1.5$. At these low redshifts, with very limited observations below $\log(M_\star/M_\odot) = 10$, Marasco et al. (2019) and Genzel et al. (2020) also find little evolution of the stellar scaling relations ($j_\star - M_\star$, TFR).

The evolution of our model for the BTFR shows the opposite trend compared to predictions from the literature, where generally low-mass discs build up their rotation velocity more gradually and high-mass discs take longer to build up their baryonic mass (Dutton & van den Bosch, 2009; Lagos et al., 2017). Our evolution model is likely overestimating the baryonic mass at early times for high-mass galaxies, due to the absence of feedback and outflows in the model, which would otherwise suppress early baryon retention and the SFR.

For the $j_\star - M_\star$ relation, the predicted evolution shows a gradual growth of $j_\star$ at all masses, with the slope of the relation staying nearly constant with a drop in the normalisation over time (fig. 22). This implies that a fixed stellar mass, the model predicts that high redshift galaxies have a higher $j_\star$. Marasco et al. (2019) found no evolution of the $j_\star - M_\star$ relation for $0 < z < 1$, which is in agreement with our findings as our models start to depart from the $z = 0$ relation for $z > 2$. Simulation show an opposite trend, with $j_\star$ increasing over time at fixed stellar mass for $0 \lesssim z \lesssim 3$ (Lagos et al., 2017). This discrepancy likely stems from the shallow growth in size at higher masses in the model as a consequence of the shallow growth in $j_{\rm acc}$ during the majority of their evolution. This is related to the choice of n, which was discussed in sections 5.1.2 and 5.1.3.

For the $j_{\rm gas} - M_{\rm gas}$ relation we see a qualitatively similar trend in the evolution as Lagos et al. (2017), with $j_{\rm gas}$ being greater at low redshifts at fixed gas mass. We also both find that this increase at fixed mass becomes greater at higher gas masses. Additionally, they find little to no evolution in the $j_{\rm bar} - M_{\rm bar}$ relation in their investigated redshift range ($0 \lesssim z \lesssim 3$) which is consistent with our findings.

5.3.3 Stellar size-Mass relation

In the evolution of the stellar size-mass relation we found that the model predicts that at fixed stellar mass, galaxies have a larger stellar disc at higher redshift. This is opposite of what is observed by van der Wel et al. (2014), which showed the SFGs of the same stellar mass are smaller at higher redshifts. This disagreement is partially a consequence of the prescribed evolution of $j_{\rm acc}$ in the model which is discussed in more detail in sections 5.1.2 and 5.1.3. Additionally, we found $R_{\rm acc}$ peaks at early times, after which it remains nearly constant for high masses. This is different compared the more monotonic growth that is prescribed to $j_{\rm acc}$. As mentioned previously, a different formalism for the DM accretion rate could indirectly contribute to a more gradual growth of $R_{\rm acc}$ and therefore also the effective radius of the disc. A more significant growth of $R_{\rm eff}$ over time, would bring the models closer to the empirical evolution of the size-mass relation.

5.3.4 SHMR

The stellar-to-halo mass ratio peaks at halo mass of $M_h \sim 10^{12} M_\odot$ and declines at both lower and higher masses due to feedback (SNe at low mass, AGN at high mass) (Shuntov et al., 2025; Somerville & Davé, 2015). At low redshifts, this efficiency peaks around $\epsilon_\star \approx 0.2$ (i.e. 20% of the cosmic baryons turned into stars). In our model we find slightly too much stellar mass in haloes compared to empirical SHMRs (Behroozi et al., 2019; Shuntov et al., 2025), particularly at $\log(M_{\rm DM}/M_\odot) \gtrsim 12$ this discrepancy is noticable. This is likely connected to a lack of quenching or reduced SF efficiency in the model as consequence of having no feedback and no possibility of morphological evolution. The slight overestimation of the stellar mass for low-mass galaxies is also likely related to the absence of feedback in the model. As discussed in section 5.1.1, this leads to overestimated stellar and baryonic mass, for a given halo mass. However, the empirical SHMR is also weighted down by ETGs, which are not included in our model. Considering the SHMR for disc galaxies reduces the disagreement (Mancera Piña et al., 2025).

In our model the SHMR at high redshift lies above the local relation, implying that haloes grew relatively more in mass than their corresponding galaxies. Behroozi et al. (2019) found a similar qualitative trend at high redshifts, showing an increase in the stellar-to-halo mass ratio at $z > 5$. Additionally, Shuntov et al. (2025) found a sharp increase in the star formation efficiency after $z > 3.5$, indicating that before that the halo growth rate is dominant over the SFR. In our model, the dominant DM growth implies that at fixed halo mass, the stellar-to-halo mass ratio is higher for galaxies at higher redshifts. If this effect is overestimated, the model may predict stellar masses that are too high at early times for a given halo mass in comparison to the empirical SHMR at high redshifts. Furthermore, the overestimation of the stellar mass at high redshift is also still tied to the same problems discussed for the overestimation at $z = 0$ and the extremely high values of $\omega_{\rm acc}$ we find for the more massive DM haloes.

5.3.5 Star formation main sequence

The model reproduces the qualitative trend in the evolution of the SFRs with redshifts, showing higher SFRs at earlier times, when compared to the empirical SFMS by Popesso et al. (2023). However the exact behaviour differs in several ways. Firstly in our model the relation remains nearly linear at all redshifts, and it slightly over predicts the SFRs at $z \leq 2$ at intermediate masses. Empirical studies often show that the SFMS slope becomes shallower above $\log(M_\star/M_\odot) \sim 10.5$,

at $z \leq 2$, interpreted as an indication of the suppressed SFR for massive galaxies as a consequence of quenching mechanisms (Schreiber et al., 2015; Popesso et al., 2023). The processes like AGN feedback and halo-quenching are not accounted for in our model. However, other studies like Speagle et al. (2014) and Pearson et al. (2018) find that a single power law describes the SFMS across this mass range well.

When looking at the SFH of single galaxies in the model, we find that the SFR peaks around $z \sim 2$, with the exception of halo masses for which a negative $\omega_{\rm acc}$ was found (fig. 17). This peak is line with the global star formation rate density of the Universe that peaks around $z \sim 2$, known as cosmic noon (Madau & Dickinson, 2014).

5.4 Comparison to model with no halo evolution

In section 4.5 we presented the results of a model with no DM evolution, i.e. the DM halo mass and its contribution to the rotation curve remain constant over time. Compared to our original results, the biggest difference is the evolution of $V_{\rm flat}$. With no DM halo growth, the evolution of $V_{\rm flat}$ is also minimal, as the DM is the dominant component in the rotation curve in the outer regions of the disc. The other properties, like the specific angular momentum and masses of the stellar, gas and baryonic component are similar to our original model, indicating that they are not strongly related to the DM halo. This confirms our interpretation about the strong dependence of the $j - M$ relations on the assumed time evolution for $j_{\rm acc}$. Under the current assumption of $n = 0.3$, $j_{\rm acc}$ already evolves little over the examined redshift range ($z = 0-7$), hence implementing no halo growth, causes little change in angular momentum. For higher values of n, a more significant change in the evolution of the angular momenta and sizes of the discs is expected between models with and without halo growth.

In general, we can conclude from these results that a faster halo growth is needed at early times to obtain a more accurate evolution of the TFR and BTFR, as this would result in a more dominant evolution of the stellar and baryonic mass compared to $V_{\rm flat}$. For an improvement in the other scaling relations, changes regarding the angular momentum of the accreted gas and an implementation of feedback are more relevant, as discussed in section 5.1.

5.5 Future Work

Aside from the direct assumptions in the model and the corresponding improvements that were discussed in section 5.1, there are several other potential extensions to our semi-analytic model.

Firstly, the model currently puts all cold gas in a single reservoir. An improvement would be to split this up into atomic (HI) and molecular (H_2) components. Observationally, star formation correlates more tightly with molecular gas than with the total cold gas (Bigiel et al., 2008). Hence by incorporating an H_2 based star formation law, the model will be able to have a more accurate SFR. To model the partitioning of cold gas into an atomic and molecular component, a metallicity or pressure based method is commonly used (Popping et al., 2014; Xie et al., 2017). Furthermore a two-phase treatment of the ISM would allow for a direct comparison to observed H_2 and HI surface density profiles.

Another related extension to the model would be to follow the chemical enrichment of gas and stars, as the current model neglects metallicity entirely. Observed metallicity gradients and mass-metallicity relations could help provide strong constraints on the enrichment history and processes in the model like accretion and radial flows (Pezzulli & Fraternali, 2016; Bilitewski & Schönrich, 2012). The non-instantaneous recycling of gas and metals also strongly impact the chemical enrichment, and would need be accounted for to accurately model observed abundances. Xie et al. (2017) also note that to have an accurate self-consistent H_2 formation efficiency, the model must be able to reproduce the mass metallicity relations in the stellar and gas components.

In the current model the surface densities evolve freely in each annulus following gas accretion, star formation and radial flows, i.e. no specific surface density shape is imposed. However, we

are treating the disc as razor-thin, thereby losing a degree of freedom to the vertical (z) structure. Adding a 3D component (e.g. thin/thick disc and bulge) could help model certain processes more accurately. Firstly, a 3D structure would allow for a volumetric star formation law to be applied, which models the SFR more accurately, especially at low surface densities (Bacchini et al., 2019). Additionally it could help model the formation of H_2, which is correlated to the midplane pressure/volume density (Krumholz & Matzner, 2009). Components like a bulge or a thick stellar disc also change the gravitational potential in the inner regions of the galaxy, thereby changing the rotation velocity and angular momentum contributions from the central regions. Furthermore a z-resolved gas reservoir could help model processes like fountain accretion, i.e. mass ejection and delayed reaccretion with modified angular momentum (Fraternali & Binney, 2008; El-Badry et al., 2018). This alters the growth of $j_{\rm gas}$ and $j_\star$ with selective low-j removal and later high-j accretion.

6 Conclusion

In this thesis, we presented a radially resolved semi-analytic model for the evolution of star-forming disc galaxies that self consistently includes gas accretion, radial flows, conservation of the angular omentum, star formation and an independent evolving dark matter halo. The free parameters of the model are total accreted baryonic mass $M_{\rm acc}(t_0)$ (with t_0 corresponding to $z = 0$), the accretion frequency $\omega_{\rm acc}$, and the maximum specific angular momentum of the accreted gas $j_{\rm max}$. These parameters are constrained using local empirical scaling relations: the baryonic Tully-Fisher relation (BTFR), the relation between the specific angular momentum, baryonic mass and gas fraction, i.e. $j_{\rm bar} - M_{\rm bar} - f_{\rm gas}$ plane, and the stellar size-mass relation. The fitting and uncertainty quantification were performed with MCMC explorations of the parameter space.

For the best-fit total accreted mass and $j_{\rm max}$ we find that they increase approximately linearly with halo mass, while the accretion frequency $\omega_{\rm acc}$ shows a systematic trend from negative (late accretion) at low halo masses ($\log(M_{\rm DM}/M_\odot) < 11$) to positive (early accretion) at high halo masses. The posterior distributions indicate that $\log M_{\rm acc}$ and $\log j_{\rm max}$ are relatively well constrained, whereas $\omega_{\rm acc}$ remains broader and more degenerate with model assumptions. The model reproduces the three local relations used for the fitting within the intrinsic scatter, giving confidence that the chosen parametrisation within the model captures the principal scaling behaviour at $z = 0$.

Examining the evolution of individual galaxy properties shows robust qualitative behaviour: discs grow inside-out, the gas disc is consistently more extended than the stellar disc, and the modelled star-formation histories peak around $z \sim 2$ for the typical parameter ranges explored. However, there are some tensions in the structural growth. The accretion radius $R_{\rm acc}$ peaks early while the prescribed $j_{\rm acc}$ grows monotonically, suggesting an underestimation of early rotation velocities, and hence halo growth, in the adopted dark matter accretion prescription. At high halo masses, the inner stellar surface densities flatten and in some cases lead to anomalous inner rotation signatures, pointing to missing channels of central mass concentration like mergers or stronger inward flows.

Comparison with high-z cold gas kinematic data reveal mixed agreement. For massive high-z discs the observed galaxies tend to lie below the local TFR and BTFR (i.e. higher asymptotic rotation velocity $V_{\rm flat}$ at fixed $M_\star$ and $M_{\rm bar}$) while the model predicts a minimal evolution of the TFR at high mass, and lower $V_{\rm flat}$ compared to the local BTFR. This discrepancy can be partly traced to the model's tendency to place accretion at very early times (high $\omega_{\rm acc}$) for high mass haloes and to a likely underestimation of halo mass growth at early times. A better agreement was found for the evolution of the $j_\star - M_\star$ and $j_{\rm bar} - M_{\rm bar}$ relations. For the gas component, the model predicts higher values of $j_{\rm gas}$ in comparison to the high-z data, which might be related to the fact that the high-z observations only trace the compact molecular gas in galactic discs.

The evolution of the stellar size-mass relation, shows a modest size evolution, consistent with inside-out growth, however the growth is weaker than expected in comparison to observations. This discrepancy is related to assumed parameter values in the $j_{\rm acc}$ growth and to the early peak in $R_{\rm acc}$ as consequence of an underestimated halo mass at early times. For the star formation main sequence (SFMS), the model naturally produces elevated star formation rates at higher redshifts, in line with empirical evolutions of the SFMS. In the inferred stellar-to-halo mass relation (SHMR) evolution, the model places the high-z relation above the local SHMR, indicating a growth in the DM haloes compared to their galaxies at early times. This trend is qualitatively similar to that reported in literature, however the model systematically overestimates the stellar-to-halo mass ratio.

Some improvements can be made to the model to provide a more accurate prediction for galaxy evolution. The most important are: 1) the inclusion of stellar/AGN-driven outflows (mass-loading) and delayed re-accretion to regulate baryon retention and increase the angular momentum of the disc $j_{\rm disc}$ via fountain recycling; 2) replace the instantaneous recycling approximation with delayed recycling using IMF-weighted lifetimes; 3) adapt the halo-growth prescription to

allow for faster early halo growth; 4) separation of the gas component into HI and H_2, potentially adding an H_2-based star formation law. Implementing even a subset of these changes is expected to reduce the need for extreme accretion histories in both low- and high-mass systems and provide a more accurate evolution of the disc properties.

In summary, this work demonstrates that a relatively simple, radially resolved semi-analytic framework, calibrated to local scaling relations, can capture the first-order evolution of masses, disc sizes, angular momenta and SFRs across cosmic time and provides insight into the effect of different physical assumptions. The remaining discrepancies highlight a small number of physically motivated extensions that should be prioritised in future versions of the model to achieve a closer agreement with high redshift observations and to help constrain otherwise poorly known parameters such as the accretion timescales and the angular momentum accretion history.

7 Acknowledgements

I would like to thank my supervisors, Filippo Fraternali and Francesca Rizzo, for their support, encouragement and feedback throughout this project. Our discussions have always been very useful and insightful and I look forward to continuing working together in the future. I am also grateful to Pavel Mancera Piña for his helpful comments and assistance in acquiring data, and to Gabriele Pezzulli for sharing his insights. Furtermore, I thank all members of Filippo's research group, Jenny, Sten, Barbara, Linn and others, our group meetings were always very insightful, and I am thankful you were always willing to help me with my struggles in the project. I would also like to thank all my friends in the research office, your daily support, shared frustrations, and encouragement made this project not only more manageable but also much more enjoyable

Finally, I acknowledge that parts of this thesis benefited from AI-assisted writing support for improving clarity, and assistance in making the Python code more streamlined and efficient.

References

Bacchini C., Fraternali F., Pezzulli G., Marasco A., Iorio G., Nipoti C., 2019, Astronomy and Astrophysics, 632, A127

Behroozi P. S., Wechsler R. H., Conroy C., 2013, The Astrophysical Journal, 770, 57

Behroozi P., Wechsler R. H., Hearin A. P., Conroy C., 2019, Monthly Notices of the Royal Astronomical Society, 488, 3143

Bera A., Kanekar N., Chengalur J. N., Bagla J. S., 2023, The Astrophysical Journal Letters, 950, L18

Bigiel F., Leroy A., Walter F., Brinks E., de Blok W. J. G., Madore B., Thornley M. D., 2008, The Astronomical Journal, 136, 2846

Bilitewski T., Schönrich R., 2012, Monthly Notices of the Royal Astronomical Society, 426, 2266

Bolatto A. D., Wolfire M., Leroy A. K., 2013, Annual Review of Astronomy and Astrophysics, 51, 207

Bond J. R., Cole S., Efstathiou G., Kaiser N., 1991, The Astrophysical Journal, 379, 440

Boogaard L. A., et al., 2020, The Astrophysical Journal, 902, 109

Bryan G. L., Norman M. L., 1998, The Astrophysical Journal, 495, 80

Bullock J. S., Kolatt T. S., Sigad Y., Somerville R. S., Kravtsov A. V., Klypin A. A., Primack J. R., Dekel A., 2001a, Monthly Notices of the Royal Astronomical Society, 321, 559

Bullock J. S., Dekel A., Kolatt T. S., Kravtsov A. V., Klypin A. A., Porciani C., Primack J. R., 2001b, The Astrophysical Journal, 555, 240

Carilli C. L., Walter F., 2013, Annual Review of Astronomy and Astrophysics, 51, 105

Casertano S., 1983, Monthly Notices of the Royal Astronomical Society, 203, 735

Catinella B., et al., 2018, Monthly Notices of the Royal Astronomical Society, 476, 875

Chabrier G., 2003, Publications of the Astronomical Society of the Pacific, 115, 763

Chiappini C., Matteucci F., Romano D., 2001, The Astrophysical Journal, 554, 1044

Chowdhury A., Kanekar N., Chengalur J. N., 2023, The Astrophysical Journal Letters, 958, L29

Christensen C. R., Davé R., Governato F., Pontzen A., Brooks A., Munshi F., Quinn T., Wadsley J., 2016, The Astrophysical Journal, 824, 57

Cimatti A., Fraternali F., Nipoti C., 2020, Introduction to galaxy formation and evolution. Cambridge University Press

Costa A., 2024, Bachelor's thesis, Rijksuniversteit Groningen

Daddi E., et al., 2010, The Astrophysical Journal, 713, 686

Danovich M., Dekel A., Hahn O., Ceverino D., Primack J., 2015, Monthly Notices of the Royal Astronomical Society, 449, 2087

Dekel A., Birnboim Y., 2006, Monthly Notices of the Royal Astronomical Society, 368, 2

Dekel A., et al., 2009, Nature, 457, 451

Di Teodoro E. M., Fraternali F., 2014, Astronomy and Astrophysics, 567, A68

Di Teodoro E. M., Fraternali F., Miller S. H., 2016, Astronomy and Astrophysics, 594, A77

Di Teodoro E. M., Posti L., Ogle P. M., Fall S. M., Jarrett T., 2021, Monthly Notices of the Royal Astronomical Society, 507, 5820

Dutton A. A., Macciò A. V., 2014, Monthly Notices of the Royal Astronomical Society, 441, 3359

Dutton A. A., van den Bosch F. C., 2009, Monthly Notices of the Royal Astronomical Society, 396, 141

El-Badry K., et al., 2018, Monthly Notices of the Royal Astronomical Society, 473, 1930

Epinat B., et al., 2009, Astronomy and Astrophysics, 504, 789

Fall S. M., 1983, in Athanassoula E., ed., IAU Symposium Vol. 100, Internal Kinematics and Dynamics of Galaxies. pp 391–398

Fall S. M., Efstathiou G., 1980, Monthly Notices of the Royal Astronomical Society, 193, 189

Fox A., Davé R., eds, 2017, Gas Accretion onto Galaxies. Astrophysics and Space Science Library Vol. 430, doi:10.1007/978-3-319-52512-9,

Fraternali F., Binney J. J., 2008, Monthly Notices of the Royal Astronomical Society, 386, 935

Fraternali F., Tomassetti M., 2012, Monthly Notices of the Royal Astronomical Society, 426, 2166

Fraternali F., Marasco A., Marinacci F., Binney J., 2013, The Astrophysical Journal Letters, 764, L21

Freeman K. C., 1970, The Astrophysical Journal, 160, 811

Frickmann D., 2022, Master's thesis, University of Copenhagen, Niels Bohr Institute

Förster Schreiber N. M., Wuyts S., 2020, Annual Review of Astronomy and Astrophysics, 58, 661

Geesink N. N., Mancera Piña P. E., Lagos C. d. P., Kriek M., 2025, Astronomy and Astrophysics, 697, A87

Genzel R., et al., 2020, The Astrophysical Journal, 902, 98

González Delgado R. M., et al., 2015, Astronomy and Astrophysics, 581, A103

Hafen Z., et al., 2022, Monthly Notices of the Royal Astronomical Society, 514, 5056

Harrison C. M., et al., 2017, Monthly Notices of the Royal Astronomical Society, 467, 1965

Kennicutt Jr. R. C., 1998, The Astrophysical Journal, 498, 541

Kereš D., Katz N., Weinberg D. H., Davé R., 2005, Monthly Notices of the Royal Astronomical Society, 363, 2

Kirkpatrick A., Sharon C., Keller E., Pope A., 2019, The Astrophysical Journal, 879, 41

Kohandel M., Pallottini A., Ferrara A., Zanella A., Rizzo F., Carniani S., 2024, Astronomy and Astrophysics, 685, A72

Krogager J. K., et al., 2024, Monthly Notices of the Royal Astronomical Society, 535, 561

Kroupa P., 2002, Science, 295, 82

Krumholz M. R., Matzner C. D., 2009, The Astrophysical Journal, 703, 1352

Krumholz M. R., Burkhart B., Forbes J. C., Crocker R. M., 2018, Monthly Notices of the Royal Astronomical Society, 477, 2716

Lagos C. D. P., Baugh C. M., Zwaan M. A., Lacey C. G., Gonzalez-Perez V., Power C., Swinbank A. M., van Kampen E., 2014, Monthly Notices of the Royal Astronomical Society, 440, 920

Lagos C. d. P., Theuns T., Stevens A. R. H., Cortese L., Padilla N. D., Davis T. A., Contreras S., Croton D., 2017, Monthly Notices of the Royal Astronomical Society, 464, 3850

Landau R. H., José M., Bordeianu C. C., 2015, Computational physics : problem solving with Python, 3 edn. Wiley-Vch. C

Leitner S. N., 2012, The Astrophysical Journal, 745, 149

Lelli F., McGaugh S. S., Schombert J. M., 2016a, The Astronomical Journal, 152, 157

Lelli F., McGaugh S. S., Schombert J. M., 2016b, The Astrophysical Journal Letters, 816, L14

Lelli F., McGaugh S. S., Schombert J. M., Desmond H., Katz H., 2019, Monthly Notices of the Royal Astronomical Society, 484, 3267

Lelli F., Di Teodoro E. M., Fraternali F., Man A. W. S., Zhang Z.-Y., De Breuck C., Davis T. A., Maiolino R., 2021, Science, 371, 713

Lin L., et al., 2008, The Astrophysical Journal, 681, 232–243

Lovell M. R., et al., 2018, Monthly Notices of the Royal Astronomical Society, 481, 1950

Madau P., Dickinson M., 2014, Annual Review of Astronomy and Astrophysics, 52, 415

Mancera Piña P. E., Read J. I., Kim S., Marasco A., Benavides J. A., Glowacki M., Pezzulli G., Lagos C. d. P., 2025, Astronomy and Astrophysics, 699, A311

Mancera Piña P. E., Posti L., Fraternali F., Adams E. A. K., Oosterloo T., 2021a, Astronomy and Astrophysics, 647, A76

Mancera Piña P. E., Posti L., Pezzulli G., Fraternali F., Fall S. M., Oosterloo T., Adams E. A. K., 2021b, Astronomy and Astrophysics, 651, L15

Marasco A., Fraternali F., Posti L., Ijtsma M., Di Teodoro E. M., Oosterloo T., 2019, Astronomy and Astrophysics, 621, L6

Martin G., Kaviraj S., Devriendt J. E. G., Dubois Y., Pichon C., 2018, Monthly Notices of the Royal Astronomical Society, 480, 2266

Mayor M., Vigroux L., 1981, Astronomy and Astrophysics, 98, 1

McGaugh S. S., Schombert J. M., 2015, The Astrophysical Journal, 802, 18

McGaugh S. S., Schombert J. M., de Blok W. J. G., Zagursky M. J., 2010, The Astrophysical Journal Letters, 708, L14

McKee C. F., Ostriker E. C., 2007, Annual Review of Astronomy and Astrophysics, 45, 565

Mo H. J., Mao S., White S. D. M., 1998, Monthly Notices of the Royal Astronomical Society, 295, 319

Mo H., van den Bosch F., White S., 2010, Galaxy Formation and Evolution. Cambridge University Press

Moster B. P., Naab T., White S. D. M., 2013, Monthly Notices of the Royal Astronomical Society, 428, 3121

Muratov A. L., Kereš D., Faucher-Giguère C.-A., Hopkins P. F., Quataert E., Murray N., 2015, Monthly Notices of the Royal Astronomical Society, 454, 2691

Navarro J. F., Frenk C. S., White S. D. M., 1996, The Astrophysical Journal, 462, 563

Nelson D., Genel S., Vogelsberger M., Springel V., Sijacki D., Torrey P., Hernquist L., 2015, Monthly Notices of the Royal Astronomical Society, 448, 59

Nelson E. J., et al., 2016, The Astrophysical Journal, 828, 27

Oppenheimer B. D., Davé R., Kereš D., Fardal M., Katz N., Kollmeier J. A., Weinberg D. H., 2010, Monthly Notices of the Royal Astronomical Society, 406, 2325

Oser L., Ostriker J. P., Naab T., Johansson P. H., Burkert A., 2010, The Astrophysical Journal, 725, 2312

Parlanti E., et al., 2024, Astronomy and Astrophysics, 684, A24

Patel S. G., et al., 2013, The Astrophysical Journal, 766, 15

Pearson W. J., et al., 2018, Astronomy and Astrophysics, 615, A146

Peebles P. J. E., 1969, The Astrophysical Journal, 155, 393

Pezzulli G., Fraternali F., 2016, Monthly Notices of the Royal Astronomical Society, 455, 2308

Pezzulli G., Fraternali F., Boissier S., Muñoz-Mateos J. C., 2015, Monthly Notices of the Royal Astronomical Society, 451, 2324

Pezzulli G., Fraternali F., Binney J., 2017, Monthly Notices of the Royal Astronomical Society, 467, 311

Pillepich A., et al., 2019, Monthly Notices of the Royal Astronomical Society, 490, 3196

Pitts E., Tayler R. J., 1989, Monthly Notices of the Royal Astronomical Society, 240, 373

Planck Collaboration et al., 2020, Astronomy and Astrophysics, 641, A6

Popesso P., et al., 2023, Monthly Notices of the Royal Astronomical Society, 519, 1526

Popping G., Somerville R. S., Trager S. C., 2014, Monthly Notices of the Royal Astronomical Society, 442, 2398

Posti L., 2022, vcdisk: Rotation curves of disk galaxies, Python package vcdisk, version 0.3.1

Posti L., Fraternali F., Di Teodoro E. M., Pezzulli G., 2018, Astronomy and Astrophysics, 612, L6

Posti L., Marasco A., Fraternali F., Famaey B., 2019, Astronomy and Astrophysics, 629, A59

Press W. H., Schechter P., 1974, The Astrophysical Journal, 187, 425

Qu Y., et al., 2017, Monthly Notices of the Royal Astronomical Society, 464, 1659

Rizzo F., Vegetti S., Powell D., Fraternali F., McKean J. P., Stacey H. R., White S. D. M., 2020, Nature, 584, 201

Rizzo F., Vegetti S., Fraternali F., Stacey H. R., Powell D., 2021, Monthly Notices of the Royal Astronomical Society, 507, 3952

Rizzo F., et al., 2023, Astronomy and Astrophysics, 679, A129

Rizzo F., et al., 2024, Astronomy and Astrophysics, 689, A273

Rodriguez-Gomez V., et al., 2016, Monthly Notices of the Royal Astronomical Society, 458, 2371

Roman-Oliveira F., Fraternali F., Rizzo F., 2023, Monthly Notices of the Royal Astronomical Society, 521, 1045

Roman-Oliveira F., Rizzo F., Fraternali F., 2024, Astronomy and Astrophysics, 687, A35

Romanowsky A. J., Fall S. M., 2012, ApJS, 203, 17

Salpeter E. E., 1955, The Astrophysical Journal, 121, 161

Schinnerer E., Leroy A. K., 2024, Annual Review of Astronomy and Astrophysics, 62, 369

Schönrich R., Binney J., 2009, Monthly Notices of the Royal Astronomical Society, 396, 203

Schreiber C., et al., 2015, Astronomy and Astrophysics, 575, A74

Shen S., Mo H. J., White S. D. M., Blanton M. R., Kauffmann G., Voges W., Brinkmann J., Csabai I., 2003, Monthly Notices of the Royal Astronomical Society, 343, 978

Shuntov M., et al., 2025, Astronomy and Astrophysics, 695, A20

Simons R. C., et al., 2016, The Astrophysical Journal, 830, 14

Somerville R. S., Davé R., 2015, Annual Review of Astronomy and Astrophysics, 53, 51

Speagle J. S., Steinhardt C. L., Capak P. L., Silverman J. D., 2014, ApJS, 214, 15

Stewart K. R., Brooks A. M., Bullock J. S., Maller A. H., Diemand J., Wadsley J., Moustakas L. A., 2013, The Astrophysical Journal, 769, 74

Stott J. P., et al., 2016, Monthly Notices of the Royal Astronomical Society, 457, 1888

Tacchella S., Dekel A., Carollo C. M., Ceverino D., DeGraf C., Lapiner S., Mandelker N., Primack Joel R., 2016, Monthly Notices of the Royal Astronomical Society, 457, 2790

Tinsley B. M., 1980, Fundamentals of Cosmic Physics, 5, 287

Tully R. B., Fisher J. R., 1977, Astronomy and Astrophysics, 54, 661

Tumlinson J., Peeples M. S., Werk J. K., 2017, Annual Review of Astronomy and Astrophysics, 55, 389

Turner O. J., et al., 2017, Monthly Notices of the Royal Astronomical Society, 471, 1280

Übler H., et al., 2019, The Astrophysical Journal, 880, 48

Verheijen M. A. W., 2001, The Astrophysical Journal, 563, 694

Voit G. M., Meece G., Li Y., O'Shea B. W., Bryan G. L., Donahue M., 2017, The Astrophysical Journal, 845, 80

Wang W., et al., 2025, Nature Astronomy, 9, 710

Watson W. A., Iliev I. T., D'Aloisio A., Knebe A., Shapiro P. R., Yepes G., 2013, Monthly Notices of the Royal Astronomical Society, 433, 1230

Whitaker K. E., van Dokkum P. G., Brammer G., Franx M., 2012, The Astrophysical Journal Letters, 754, L29

Wisnioski E., et al., 2019, The Astrophysical Journal, 886, 124

Xie L., De Lucia G., Hirschmann M., Fontanot F., Zoldan A., 2017, Monthly Notices of the Royal Astronomical Society, 469, 968

Yang L., et al., 2025, arXiv preprint

Zhang W., Kauffmann G., Wang J., Chen Y., Fu J., Wu H., 2021, Astronomy and Astrophysics, 648, A25

van de Voort F., Schaye J., Booth C. M., Haas M. R., Dalla Vecchia C., 2011, Monthly Notices of the Royal Astronomical Society, 414, 2458

van den Bosch F. C., Jiang F., Hearin A., Campbell D., Watson D., Padmanabhan N., 2014, Monthly Notices of the Royal Astronomical Society, 445, 1713

van der Kruit P. C., Searle L., 1981, Astronomy and Astrophysics, 95, 105

van der Wel A., et al., 2014, The Astrophysical Journal, 788, 28

A Constants

Name	Symbol	Value	Note
Gravitational constant	G	$4.300 \times 10^{-6}\,\mathrm{kpc}\,(\mathrm{km/s})^2\,\mathrm{M}_\odot^{-1}$	
Hubble constant	H_0	$67.66\,\mathrm{km\,Mpc^{-1}\,s^{-1}}$	
Reduced Hubble constant	h	0.6766	$h = H_0/100$
Matter density parameter	$\Omega_{\mathrm{m},0}$	0.315	
Vacuum density parameter	$\Omega_{\Lambda,0}$	0.6847	
Radiation density parameter	$\Omega_{\mathrm{r},0}$	9.26×10^{-5}	

Table 5: Constants in the model with their used value. The cosmological parameters are from Planck Collaboration et al. (2020).

B Code

The Python code of our evolution model is provided in the linked Github repository. In addition, the code used to compute the angular momenta of the galaxies in our high redshift sample is also provided.

url: https://github.com/AnnaEsselink/MScThesis_Astronomy_public

C MCMC - Corner Plot Results

C.1 Corner plots results ($n = 0.3$)

The following figures show the MCMC results for models with halo masses at $z = 0$ spanning the range $\log(M_{\rm DM}/M_\odot) = 10.25 - 13.00$ in steps of 0.25 dex. No angular momentum mismatch between the disc and accreting gas is assumed, and the power in the $j_{\rm acc}(t)$ relations was set to $n = 0.3$. The red line indicates the maximum of the resulting posterior distribution presented by the histograms in the corner plots. The dashed red lines are the 1σ bounds around the maximum. The blue line represents the median of the sample within those bounds.

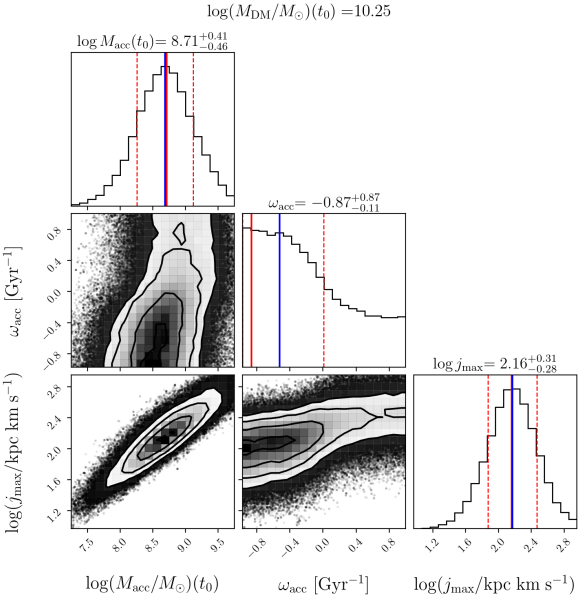

Figure 31: Corner plot for $\log(M_{\rm DM}/M_\odot) = 10.25$,

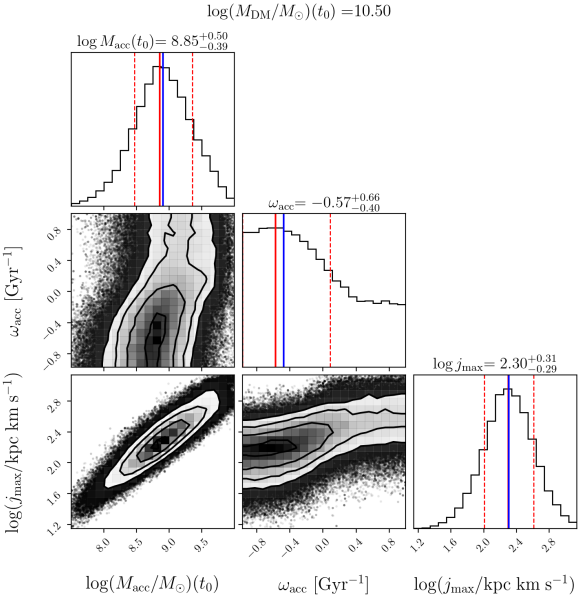

Figure 32: Corner plot for $\log(M_{\rm DM}/M_\odot) = 10.50$,

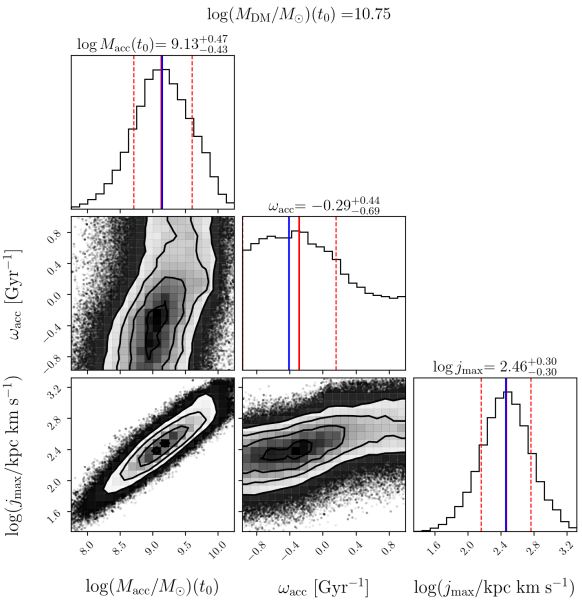

Figure 33: Corner plot for $\log(M_{\rm DM}/M_\odot) = 10.75$,

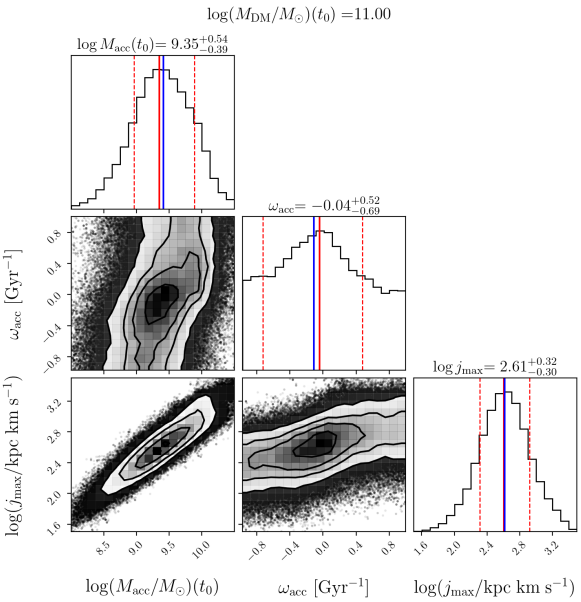

Figure 34: Corner plot for $\log(M_{\rm DM}/M_\odot) = 11.00$,

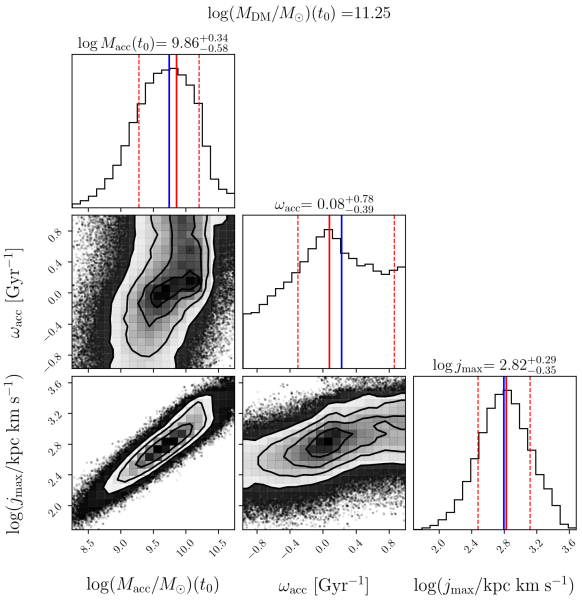

Figure 35: Corner plot for $\log(M_{\rm DM}/M_\odot) = 11.25$,

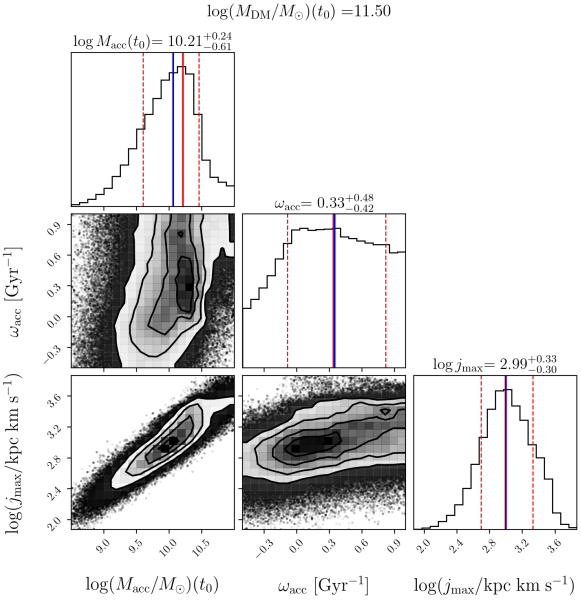

Figure 36: Corner plot for $\log(M_{\rm DM}/M_\odot) = 11.50$,

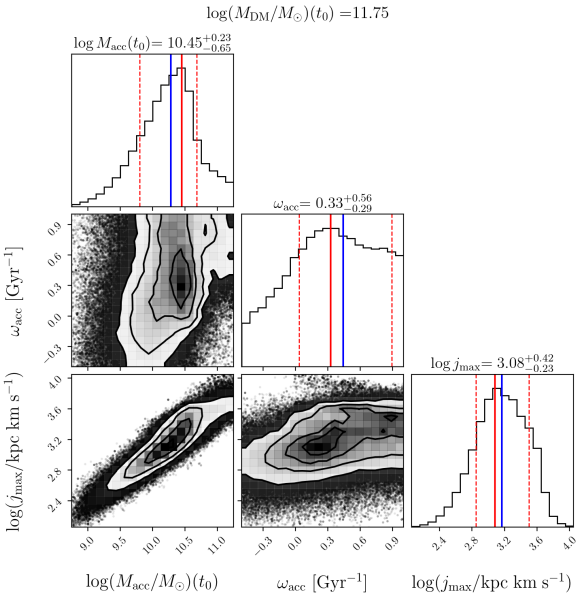

Figure 37: Corner plot for $\log(M_{\rm DM}/M_\odot) = 11.75$,

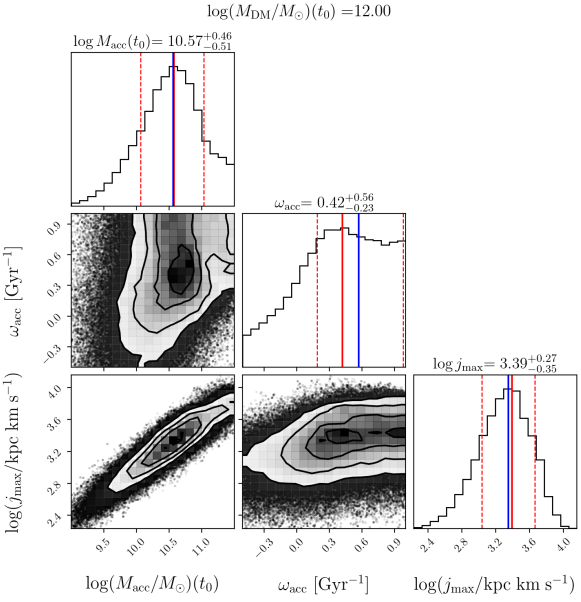

Figure 38: Corner plot for $\log(M_{\rm DM}/M_\odot) = 12.00$,

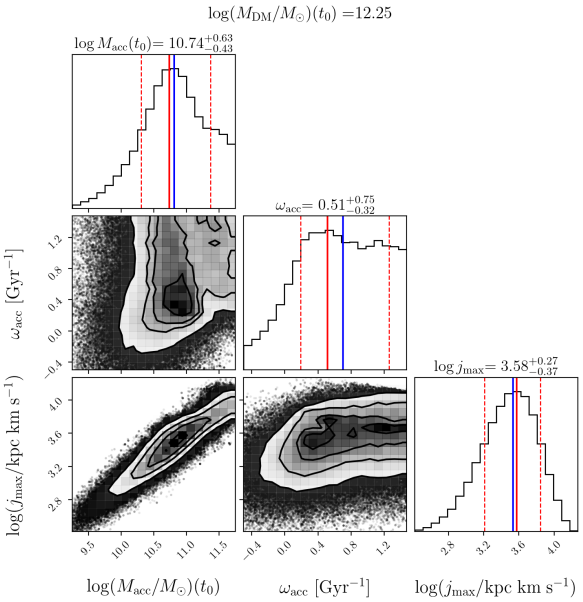

Figure 39: Corner plot for $\log(M_{\rm DM}/M_\odot) = 12.25$,

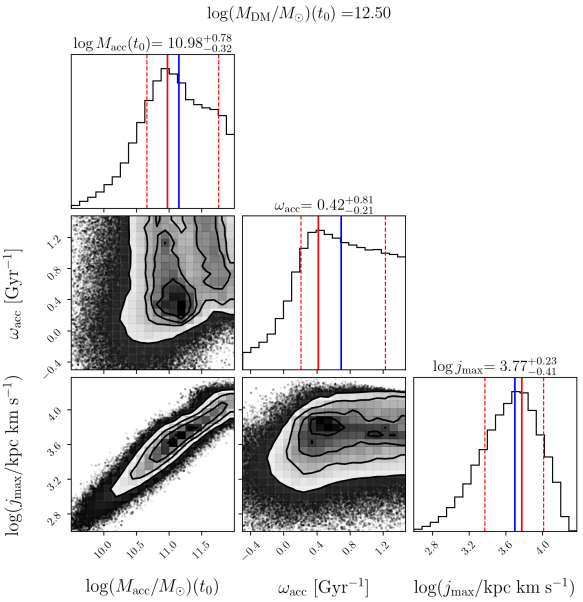

Figure 40: Corner plot for $\log(M_{\rm DM}/M_\odot) = 12.50$,

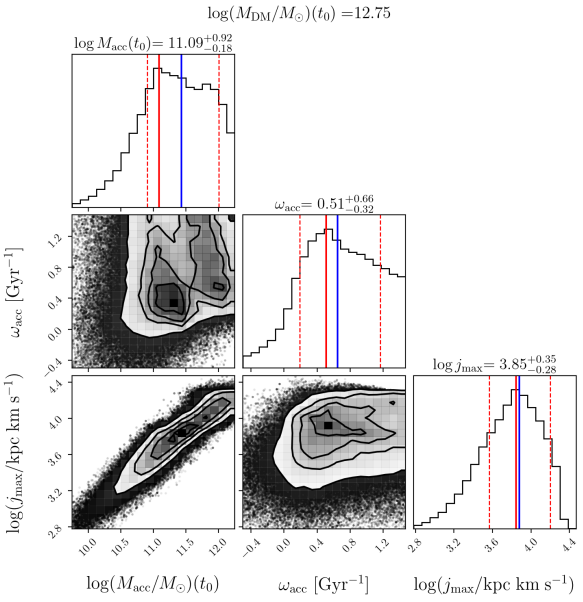

Figure 41: Corner plot for $\log(M_{\rm DM}/M_\odot) = 12.75$,

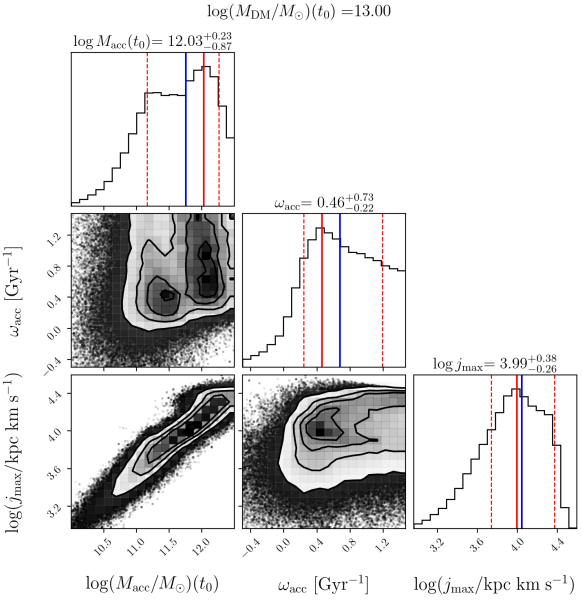

Figure 42: Corner plot for $\log(M_{\rm DM}/M_\odot) = 13.00$,

C.2 Corner plots for different n and angular momentum mismatch

For the halo masses $\log(M_{\rm DM}/M_\odot)(t_0) = 11.0, 11.75, 12.50$ we test the model for different values of the angular momentum mismatch α (section 2.3) and of the power in the $j_{\rm acc}(t)$ evolution n (section 2.2.2). The title in the figures indicate which values of $\log M_{\rm DM}$, α and n the corner plot corresponds to. When α is not indicated $\alpha = 0$.

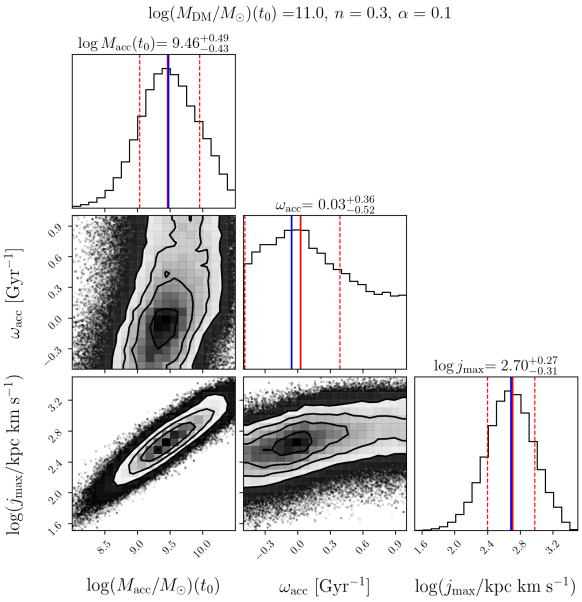

Figure 43: Corner plot for $\log(M_{\rm DM}/M_\odot) = 11.00$, $\alpha = 0.1$

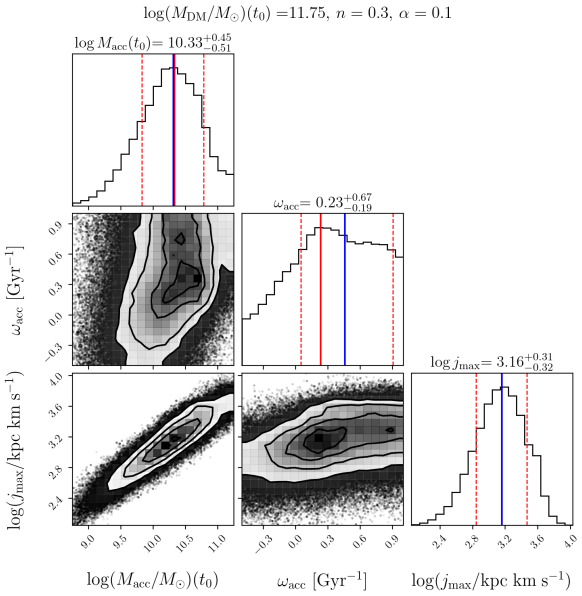

Figure 44: Corner plot for $\log(M_{\rm DM}/M_\odot) = 11.75$, $\alpha = 0.1$

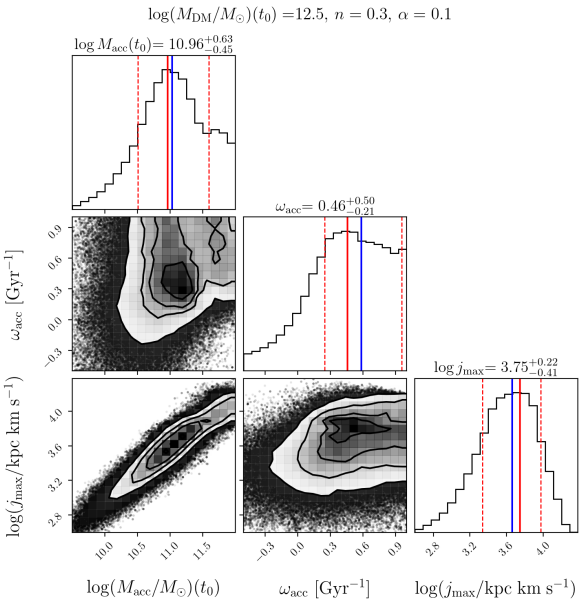

Figure 45: Corner plot for $\log(M_{\rm DM}/M_\odot) = 12.50$, $\alpha = 0.1$

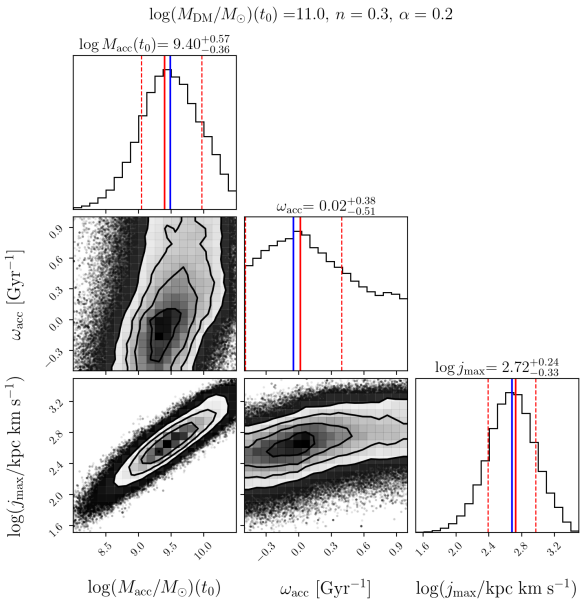

Figure 46: Corner plot for $\log(M_{\rm DM}/M_\odot) = 11.00$, $\alpha = 0.2$

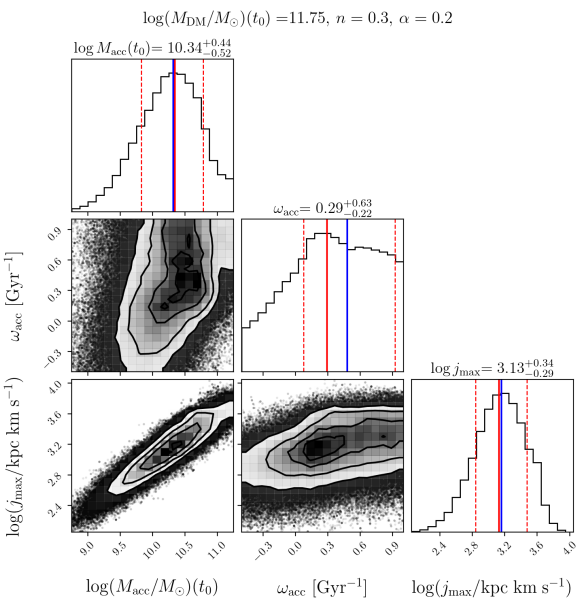

Figure 47: Corner plot for $\log(M_{\rm DM}/M_\odot) = 11.75$, $\alpha = 0.2$

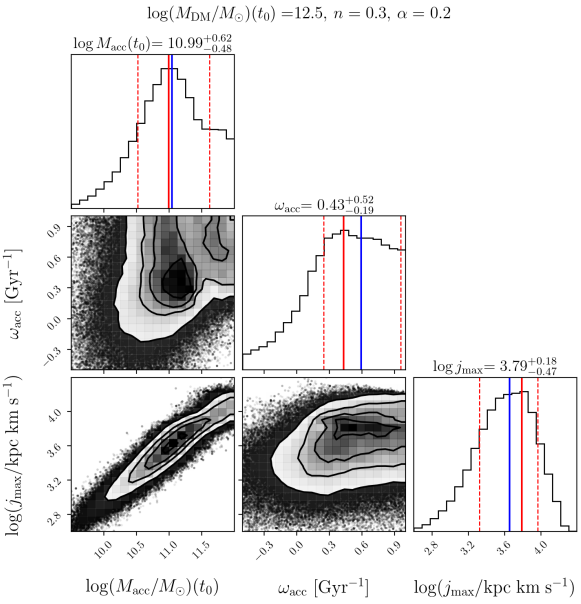

Figure 48: Corner plot for $\log(M_{\rm DM}/M_\odot) = 12.50$, $\alpha = 0.2$

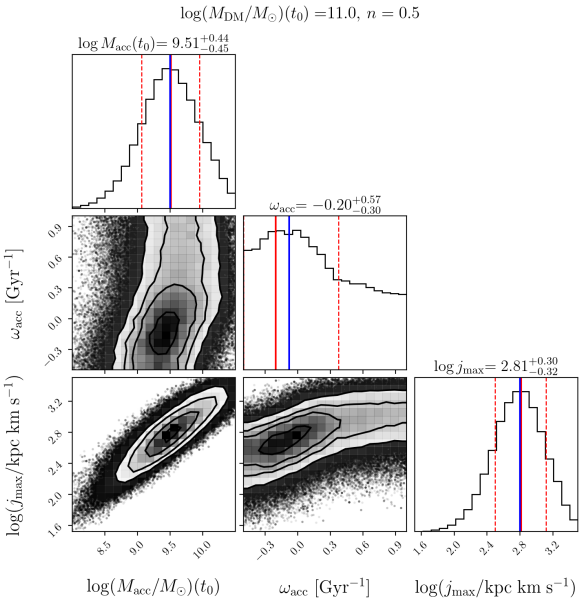

Figure 49: Corner plot for $\log(M_{\rm DM}/M_\odot) = 11.00$, $n = 0.5$

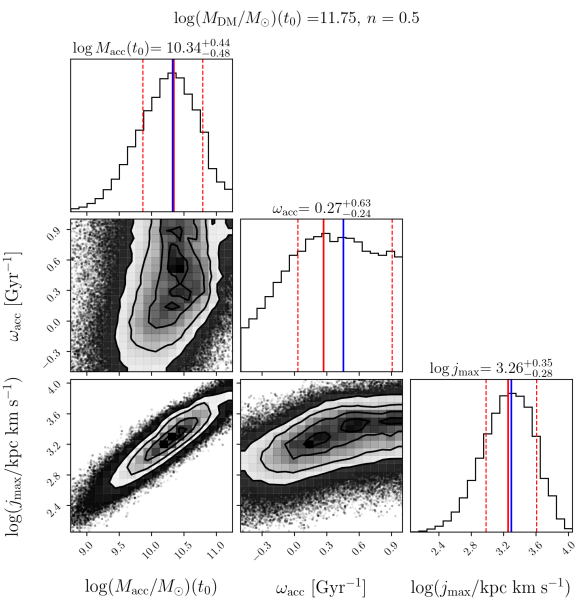

Figure 50: Corner plot for $\log(M_{\rm DM}/M_\odot) = 11.75$, $n = 0.5$

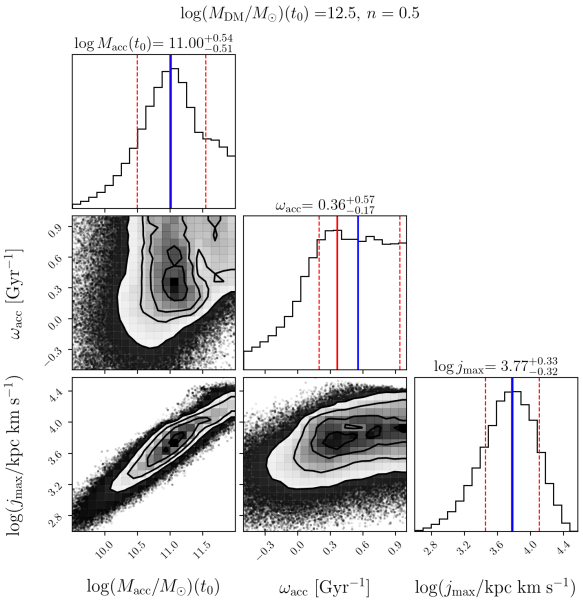

Figure 51: Corner plot for $\log(M_{\rm DM}/M_\odot) = 12.50$, $n = 0.5$

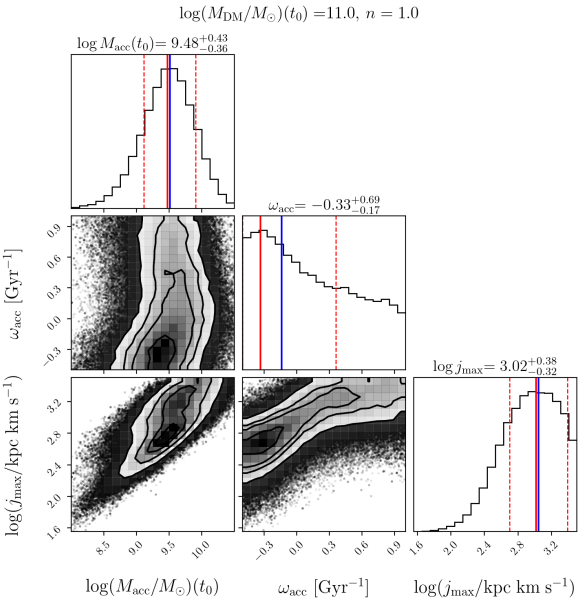

Figure 52: Corner plot for $\log(M_{\rm DM}/M_\odot) = 11.00$, $n = 1.0$

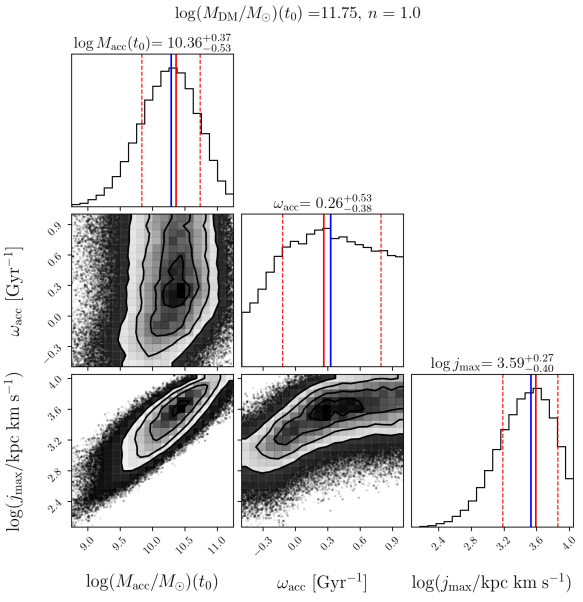

Figure 53: Corner plot for $\log(M_{\rm DM}/M_\odot) = 11.75$, $n = 1.0$

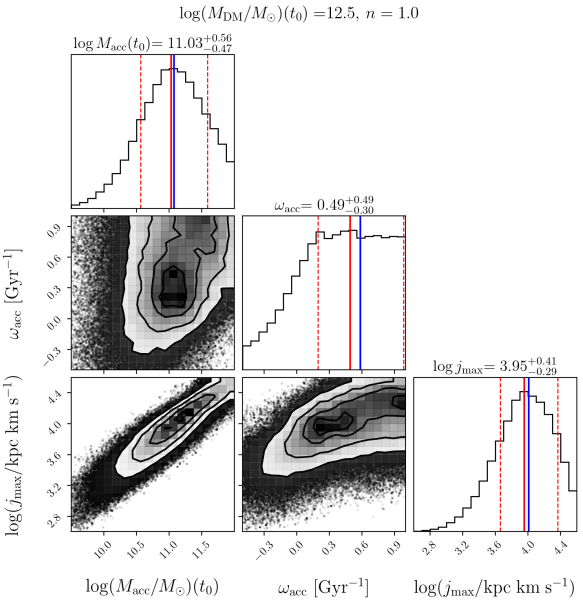

Figure 54: Corner plot for $\log(M_{\rm DM}/M_\odot) = 12.50$, $n = 1.0$